Doctoral Dissertation
Doctoral Program in Metrology (32nd cycle)

Metrological Approach to Tip-enhanced Raman Spectroscopy

Alessio Sacco
* * * * * *

Supervisors
Prof. Renato S. Gonnelli
Dott. Andrea M. Rossi

Doctoral Examination Committee:

Prof. Volker Deckert, Referee, Friedrich-Schiller University of Jena, Germany

Prof. Tullio Scopigno, Referee, Sapienza University of Rome, Italy

Prof. Enzo Di Fabrizio, Politecnico di Torino, Italy

Prof. Fabrizio Giorgis, Politecnico di Torino, Italy

Prof. Giuseppe Spoto, University of Turin, Italy

Politecnico di Torino
October 31st, 2019

I hereby declare that, the contents and organisation of this dissertation constitute my own original work and does not compromise in any way the rights of third parties, including those relating to the security of personal data.

. . . . . .

Alessio Sacco

Turin, October 31st, 2019

Summary

Tip-enhanced Raman spectroscopy (TERS) is a surface measurement technique which, combining surface-enhanced Raman spectroscopy (SERS) and scanning probe microscopy (SPM), is capable of topographic and chemical imaging simultaneously, each with nanometric lateral resolution, and can achieve single-molecule Raman detection. The Raman community is currently lacking reference samples, standardised procedures for enhancement factor evaluation, and even common definitions which are essential for the harmonisation and comparability of results. This work tackled some of the most pressing metrological needs of TERS while also exploring innovative approaches for the improvement of the efficiency of the technique, its accuracy, and the evaluation of its uncertainty.

TERS requires specific probes with strict parameters in terms of shape, dimensions and material for plasmon resonance with a specific excitation wavelength. The first part of the thesis was dedicated to manufacture highly enhancing TERS probes; for uniformity and comparability of Raman intensity of single spectra and spatial resolution of multispectral images, high reproducibility of these tips was sought. Optimised and reproducible STM-TERS tips were produced by devising and constructing an electronic control circuit for the electrochemical etching of silver wire. Tips with apices radii of (40 $\pm$ 10) nm were achieved. Best parameters for the fabrication of AFM-TERS gold-coated tips by sputtering were also determined by conceiving and exploring a novel configuration for TERS, the "isolated tip", to improve spectral intensity reproducibility.

A candidate reference sample for assessing the spatial capabilities of TERS was designed, manufactured and measured with STM-TERS. Compounds able to form ordered self-assembled monolayers (SAMs) were employed for this. Surfaces were produced with SAMs of two different organic molecules, and analysed after an optimisation study on their manufacturing steps. After topographic and chemical mapping by STM-TERS, a suitable substrate production process was identified.

The subject of TERS intensity reproducibility was also studied. The isolated tip mode was compared to measurements carried out with the most common methodology. The novel procedure reduced data dispersion by more than 40%.

A new concept was also conceived and achieved: "tip dimers". This new configuration, consisting in the contact of two TERS tips, conceptually equal to the commonly occurring SERS nanoparticle dimers, was sought to improve the sensitivity of the technique. A convenient substrate for the realisation of tip dimers was produced. Spectral intensities up to three times higher than those arising from the standard technique were measured.

Thiram, a law-regulated pesticide, was analysed, furtherly opening up TERS for much needed real-world applications. Traces of this chemical agent (in the order of magnitude of 1000 molecules) were successfully detected with tip dimers with high signal to noise ratio, suggesting a much lower limit of detection.

The accurate quantification of enhancement factor is an open issue in SERS and TERS. In this thesis, a study was conducted to face this problem, executing novel operating procedures: a measurement for the estimation of non-enhanced Raman intensity of an analyte with the same instrumental conditions as its amplified counterpart was performed by employing a liquid solution of the analyte in a solvent; furthermore, the number of molecules investigated by non-amplified Raman was quantified by a precise estimation of the focal volume of the microscope by probing it with monolayer graphene sheets, measuring their Raman intensity while scanning them in the three dimensions. Enhancement factors were calculated with their uncertainties for the three TERS configurations explored in this thesis for three analytes. It was found that thiram yielded higher enhancement factors with respect to commonly employed TERS analytes.

Acknowledgements

Financial support from the MetvBadBugs project is acknowledged. The project 15HLT01 MetvBadBugs has received funding from the EMPIR programme cofinanced by the Participating States and from the European Union's Horizon 2020 research and innovation programme.

Contents

List of Tables

List of Figures

List of Abbreviations

In order of appearance in the main text:

- TERS: tip-enhanced Raman spectroscopy;
- SERS: surface-enhanced Raman spectroscopy;
- SPM: scanning probe microscopy;
- SPR: surface plasmon resonance;
- LSPR: localised surface plasmon resonance;
- LFIEF: local field intensity enhancement factor;
- EF: enhancement factor;
- LRE: lightning rod effect;
- AFM: atomic force microscopy;
- STM: scanning tunnelling microscopy;
- NA: numerical aperture;
- Nd:YAG: neodymium-doped yttrium aluminum garnet;
- CCD: charge-coupled device;
- PID: proportional-integral-derivative;
- SI: International System of Units
- BIPM: *Bureau International des Poids et Mesures* (International Bureau of Weights and Measurements);
- VIM: International Vocabulary of Metrology;
- NIST: National Institute of Standards and Technology;

- ASTM: American Society for Testing and Materials;
- SRM®: Standard Reference Material®;
- SEM: scanning electron microscopy;
- MOSFET: metal-oxide-semiconductor field-effect transistor;
- LED: light-emitting diode;
- SWCNTs: single-walled carbon nanotubes;
- SAM: self-assembled monolayer;
- ISO: International Organization for Standardization;
- EBL: electron-beam lithography;
- PMMA: poly methyl-methacrilate;
- MIBK: methyl isobutyl ketone;
- MMC: 7-mercapto-4-methylcoumarin;
- FWHM: full width at half maximum;
- PDMS: polydimethylsiloxane;
- TEM_{00}: transverse electromagnetic mode of radial and angular orders 0 and 0;
- ERS: enhanced Raman spectroscopy;
- ERC: enhanced Raman conditions;
- RC: (non-enhanced) Raman conditions.

Part I

Introduction

Chapter 1

Electromagnetic model for surface-enhanced Raman scattering

Tip-enhanced Raman spectroscopy (TERS) is a measurement technique which takes advantage of the extremely high amplification of Raman by nanostructured surfaces, the base principle of surface-enhanced Raman spectroscopy (SERS), employing a single nanoparticle in the form of the apex of a specifically conceived scanning probe microscopy (SPM) tip, allowing topographic and enhanced Raman images with nanometric spatial resolution concurrently. To understand TERS, a theoretical dissertation of SERS can be employed, applying it to the case of a single, SERS-active nanostructured cone. While the exact mechanisms for surface-conveyed Raman amplification are not fully understood as of today, a treatise applicable to TERS experimental findings can be sought in the electromagnetic theory of SERS.

This approach explains the enhancement of the cross section of the Raman effect, as well as that of fluorescence phenomena, in proximity of a conductive surface in specific conditions as caused by the excitation of plasmons, quanta of plasma oscillations. Plasmons are collective oscillations of the free (conduction) electrons cloud theorised in the Drude and Sommerfeld models for electric conduction, resulting in collective charge density displacement relative to the positive (still) lattice nuclear charge. Specific wavelengths of the incident light may stimulate plasmons, causing their resonant oscillation at the interface of the conductor with vacuum or the dielectric medium, resulting in *surface plasmon resonance* (SPR), which produces a high magnification of electric fields near the surface. This can occur in or near the visible electromagnetic frequency range if the conductive surface is nanostructured (i.e. displays at least portions with nanometric curvature radii, such as in nanoparticles or surfaces having nanometric roughness) and the appropriate wavelength has a component which is orthogonal to it.

The most widespread materials for the production of SERS-active substrates or particles are silver and gold. This is due to the possibility of engineering plasmonic resonances with these metals in the visible or near-infrared spectral regions, while providing high chemical stability in common environmental conditions. Other metals such as platinum, palladium and copper can be exploited to induce the SERS effect and are sometimes employed, but they are less common because of inconvenient resonance wavelengths or chemical reactivity.

A description and a theoretical explanation for the SERS amplification, the electromagnetic theory, which justifies the effect at the base of the experimental findings of *Fleischmann, et al.* [1] with localised surface plasmon resonance (LSPR), derives from the solution of Maxwell's equations.

1.1 Permittivity in the Drude theory

The relative permittivity function $\epsilon(\lambda)$ of bulk materials (where λ is the wavelength of electromagnetic wave travelling through the material) plays an essential role in understanding the SERS effect. This quantity, a function of light frequency, is linked in dielectrics to their index of refraction by the relation $n(\lambda) = \sqrt{\epsilon(\lambda)}$. In the simplest dissertation of light phenomena in dielectrics, both ϵ and n are always considered real numbers ≥ 1, and often approximated as constants, which is why the function is often named *dielectric constant* in this context; however, in a more in-depth treatise of materials science, permittivity is a function of wavelength, and a complex number as well. In particular, to explain LSPR treatment of the topic of electric permittivity, both of conductors and dielectrics, as complex functions of λ must be carried out, since, in order for the SERS effect to arise, an appropriate conductive material of choice, almost always a pick from a narrow selection of metals, should present an interface with vacuum or a dielectric.

The Drude model for electrical conduction of materials considers a free electron gas roaming in the static crystalline atomic (ionic) structure, and includes a damping term in their free motion through the lattice by defining a parameter tied to electrical resistivity, the electron scattering rate $\gamma = \tau^{-1}$, where τ is the mean relaxation time between two consecutive collisions of electrons with the "stationary" ions. An electric field $\vec{E}$ may influence the material, otherwise at equilibrium, by displacing the electron cloud, while causing the arising of a charge displacement and a restoring force on the gas. Considering a single electron, this also leads to a non-zero dipole moment $\vec{\mu} = e\vec{r}$, where e is the electron (elementary) charge, and $\vec{r}$ is the displacement vector from the equilibrium. The effect of the summation of the behaviours of these electrons, of density n, results in a macroscopic polarisation density $\vec{P} = n\vec{\mu}$, which is a component of the electrical displacement field in a

medium $\vec{D}$, whose expression in time is:

$$\vec{D}(\vec{r},t) = \epsilon_0 \vec{E}(\vec{r},t) + \vec{P}(\vec{r},t) = \epsilon_0 \epsilon \vec{E}(\vec{r},t) \tag{1.1}$$

where t is the time variable, and ϵ_0 is the vacuum permittivity. From equation 1.1, an expression for the relative permittivity ϵ can be extracted:

$$\epsilon = 1 + \frac{|\vec{P}(\vec{r},t)|}{\epsilon_0 |\vec{E}(\vec{r},t)|} \tag{1.2}$$

From the Drude theory:

$$m_e \frac{\partial^2 \vec{r}}{\partial t^2} + m_e \gamma \frac{\partial \vec{r}}{\partial t} = e E_0 e^{-i\omega t} \tag{1.3}$$

in which the oscillating electric field $\vec{E} = E_0 e^{-i\omega t}$ is characterised by its amplitude E_0 and ω, which is the angular frequency of the wave, the following can be calculated:

$$\vec{r}(t) = r_0 \; e^{-i\omega t} \tag{1.4}$$

By combining equations 1.2 and 1.4, an expression for the relative permittivity of the material can be obtained:

$$\epsilon = 1 - \frac{\omega_p^2}{\omega^2 + \gamma^2} + i \frac{\gamma \omega_p^2}{\omega(\omega^2 + \gamma^2)} \tag{1.5}$$

where the plasma frequency of the material $\omega_p = \sqrt{\frac{ne^2}{\epsilon_0 m_e}}$ is introduced. In the expression of ω_p, the parameter m_e is the effective electron mass. Equation 1.5 includes the real and imaginary parts of $\epsilon(\omega)$, from which an equivalent form $\epsilon(\lambda)$ can be trivially extracted.

Figure 1.1 shows the real and imaginary contributions to the permittivities of silver and gold separately in the visible range and adjacent portions of the electromagnetic spectrum. It is noteworthy that the real parts of $\epsilon(\lambda)$ in both metals are relatively large in module, and negative. They also follow well the lossless Drude model, whose prediction can be read in expression 1.5 ignoring the imaginary part and the scattering rate γ. The imaginary part of $\epsilon(\lambda)$ is related instead to the absorption of light from the material (therefore an ideal, lossless material would have $\mathrm{Im}\{\epsilon(\lambda)\} = 0$). While silver has a low $\mathrm{Im}\{\epsilon(\lambda)\}$ in all the visible range, gold behaves like silver only in the portion of the visible range corresponding to wavelengths greater than 600 nm, as interband electronic transitions, additional contributions not considered by the Drude model, play an important role in its $\epsilon(\lambda)$.

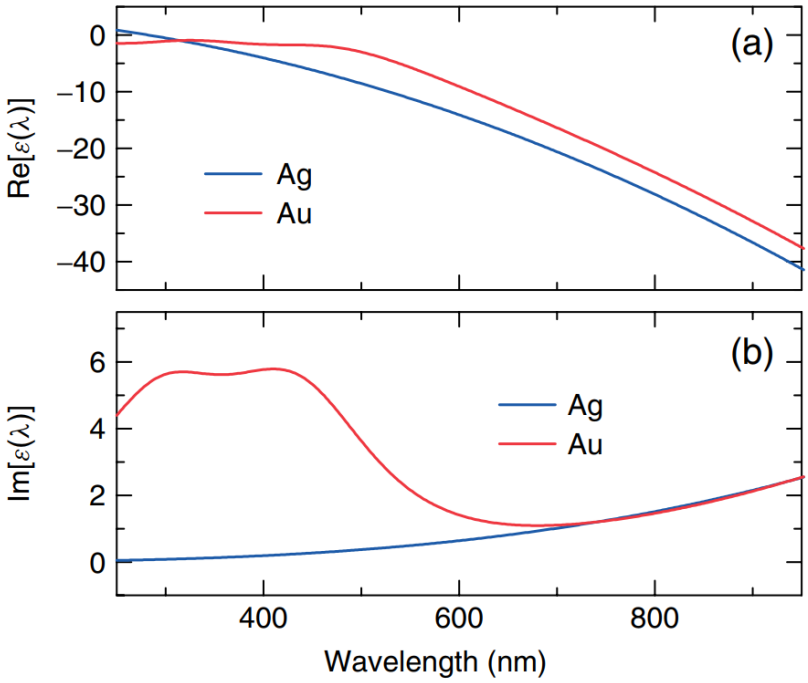

Figure 1.1: Accurate analytical representations of real (a) and imaginary (b) parts of the relative permittivities of silver and gold. Reprinted with permission from [2]. Copyright © 2010, John Wiley and Sons.

1.2 Surface plasmons in a flat interface

To understand the origin of plasmons, an interface between two media has to be considered: in the simplest of cases, an infinite planar surface separating two half-spaces of different materials, descripted by the equation $z = 0$ and therefore correspondent to the xy plane in Cartesian coordinates. In the case of an ideal, lossless dielectric at $z < 0$, thus having only a real component of its dielectric function $\epsilon_1(\omega)$ and a non-ideal metal at $z > 0$ with a complex electric permittivity $\epsilon_2(\omega)$, wave propagation at the interface is described by the Helmholtz equation for the electric field $\vec{E} = E_0 e^{-i\omega t}$:

$$\nabla^2 \vec{E}(\vec{r}, \omega) + \frac{\omega^2}{c^2} \epsilon(\vec{r}, \omega) \vec{E}(\vec{r}, \omega) = 0 \tag{1.6}$$

taking into consideration that the wavevector modulus is $k = \frac{\omega^2}{c^2} \epsilon(\vec{r}, \omega)$.

Solutions to this equation may be identified as p-polarised waves, whose electric field is at all times orthogonal to the surface, and s-polarised waves, whose electric field is instead always parallel to the surface. Considering electromagnetic waves propagating along the flat surface, a p-polarised wave must be selected. This

evanescent wave would have exponentially extinguishing electric field in the z direction at both sides of the interface, hence it can be expressed in the form:

$$\vec{E}_j = \begin{pmatrix} E_{xj} \\ 0 \\ E_{zj} \end{pmatrix} e^{i(k_x x - wt)} e^{\pm i k_{zj} z} \qquad j = 1{,}2 \tag{1.7}$$

where the x, y, z pedices indicate the component along the corresponding Cartesian axis, $j = 1{,}2$ corresponds to half-space 1 (dielectric) and 2 (metal), and the $\pm$ symbol is $+$ for $z > 0$ (metal) and $-$ for $z < 0$ (dielectric). Continuity conditions imply that $k_{x1} = k_{x2}$ at the surface, if a propagation along the x axis is supposed. Also the following is valid:

$$\epsilon_j k_0^2 = k_x^2 + k_{zj}^2 \tag{1.8}$$

where $k_0 = \frac{2\pi}{\lambda}$ is the wavevector modulus in vacuum.

An expression similar to 1.7 can also be stated for the magnetic field $\vec{H}$:

$$\vec{H}_j = \begin{pmatrix} 0 \\ H_{yj} \\ 0 \end{pmatrix} e^{i(k_x x - wt)} e^{\pm i k_{zj} z} \qquad j = 1{,}2 \tag{1.9}$$

again for both half-spaces, where the $\pm$ symbol is $+$ in the half-space corresponding to $j = 1$ and $-$ for $j = 2$.

Employing the Ampère-Maxwell law with 1.7 and 1.9:

$$\boldsymbol{\nabla} \times H_j = \epsilon_j \frac{1}{c} \frac{\partial E_j}{\partial t} \qquad j = 1{,}2 \tag{1.10}$$

equations for each half-space can be derived:

$$\epsilon_1 \frac{\omega}{c} E_{x1} = H_{y1} k_{z1} \tag{1.11}$$

$$\epsilon_2 \frac{\omega}{c} E_{x2} = -H_{y2} k_{z2} \tag{1.12}$$

Combining these with boundary conditions, i.e. continuity at the interface:

$$E_{x1} = E_{x2} \tag{1.13}$$

$$H_{y1} = H_{y2} \tag{1.14}$$

an expression for the electrical permittivities of the materials can be derived:

$$\frac{\epsilon_1}{k_{z1}} = -\frac{\epsilon_2}{k_{z2}} \tag{1.15}$$

By employing equation 1.8 and 1.15, the two components of the wavevector at the interface can be expressed as:

$$k_x = \sqrt{\frac{\epsilon_1 \epsilon_2}{\epsilon_1 + \epsilon_2}}\, k_0 = \sqrt{\frac{\epsilon_1 \epsilon_2}{\epsilon_1 + \epsilon_2}}\, \frac{\omega}{c} \qquad \lambda_{spp} = \lambda \sqrt{\frac{\epsilon_1 + \epsilon_2}{\epsilon_1 \epsilon_2}} \tag{1.16}$$

$$k_{zj} = \frac{\epsilon_j}{\sqrt{\epsilon_1 + \epsilon_2}}\, k_0 \qquad j = 1{,}2 \tag{1.17}$$

where λ_{spp} is the *surface plasmon polariton wavelength*. Note that this term is not a simple linear function of the incident wavelength λ because ϵ_j is itself a function of λ. For a surface mode to exist, k_x must have a non-zero real part. In most cases, though, this term is complex: its imaginary part accounts for the decay of the surface plasmon polariton as it propagates along the interface because of electron scatterings. $|\vec{E}|$ decreases exponentially in space, with a damping term equal to $\mathrm{Im}\{k_x\}^{-1}$. Therefore, if the metal has a small imaginary part of its electric permittivity with respect to its real part, as in the case of gold and silver, the small imaginary part of k_0 can be negligible. It is noteworthy that the wavelength is influenced by the permittivity of the dielectric at the interface as well. Nevertheless, k_x is real only if both the numerator and the denominator under the square root in equation 1.16 are either positive or negative.

Since the analysed case is a wave which is evanescent in the z direction, k_{zj} is imaginary in both half-spaces, and the electric field wave decays exponentially in both media. In the case of metals, the decay length k_{zj}^{-1} is in the order of magnitude of nanometres or tens of nanometres, while for dielectrics this can be few hundreds of nanometres.

Summarising the conditions for the permittivities:

$$\epsilon_1(\omega) + \epsilon_2(\omega) < 0 \qquad \wedge \qquad \epsilon_1(\omega)\ \epsilon_2(\omega) < 0 \tag{1.18}$$

which imply a negative permittivity of a medium which is, in modulus, larger than the positive permittivity of the other. This is the case of some metals (especially gold and silver) interfaced with vacuum and many dielectrics including air and water.

Considering an interface between metal and air, equation 1.16 can be combined with the lossless variant of expression 1.5 to obtain:

$$k_x = \frac{\omega}{c}\sqrt{\frac{\omega^2 - \omega_p^2}{2\omega^2 - \omega_p^2}} \tag{1.19}$$

which is resonant at $\omega = \frac{\sqrt{2}}{2}\omega_p$. Of course this derives from a lossless approximation, and an actual wave would be subjected to dampening.

From the complex permittivity of metals, it is possible to derive their orthogonal reflectance for planar surfaces $R = |\frac{n_2 - n_1}{n_1 + n_2}|^2$, with $n_j = \sqrt{\epsilon_j}$. Reflectances of gold and silver are reported in figure 1.2b. Silver has very high reflectivity, comparable to 100%, in the whole visible range (which is why it is traditionally employed for mirrors); gold has low reflectivity (about 50%) at wavelengths below 600 nm, which is the reason for its characteristic colour, but its R is comparable with silver at $\lambda > 600$ nm, which is why it is commonly used for mirrors for NIR applications.

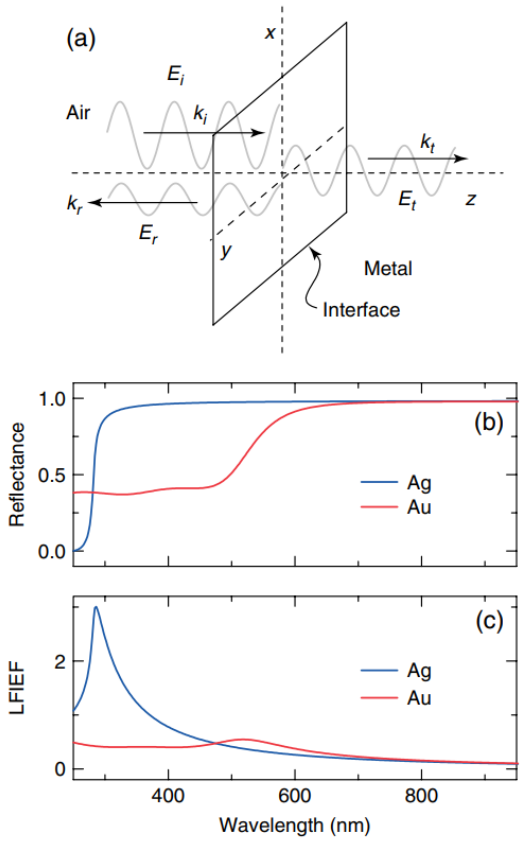

Figure 1.2: Scheme of an electromagnetic wave orthogonally incident on a metal-air flat, infinite interface (a), incoming from the air half-space, and reflectance at normal incidence (b) and local field intensity enhancement factors (LFIEF) (c) as functions of wavelength in a point in air near the surface, when the metals are silver and gold. Reprinted with permission from [2]. Copyright © 2010, John Wiley and Sons.

In order to quantify the Raman enhancement (or quenching) caused by surfaces, it is convenient to introduce a quantity, the *local field intensity enhancement factor* (LFIEF), which is a factor indicating how much the intensity of the electric field is changed with respect to the intensity that would take place without the surface:

$$\mathrm{LFIEF}(r,\omega) = \frac{|\vec{E}(r,\omega)|^2}{|\vec{E}_0(r,\omega)|^2} \tag{1.20}$$

where $\vec{E}(r,\omega)$ is the local field amplitude, inclusive of the surface contribution, and $\vec{E}_0(r,\omega)$ is the electric (excitation) incident field, which is the electric field vector that would exist if the conductive surface were not present. The value of the LFIEF is dependent on the electromagnetic frequency taken into consideration, and on the

position with respect to the surface. It is given, in a point adjacent to a surface for orthogonal incidence of excitation, by LFIEF $= |\frac{4n_1}{n_1+n_2}|^2$. The LFIEF for a point immediately above the flat, infinite interface between metal and air for both gold and silver is shown in figure 1.2c. It is noticeable that both coinage metals have LFIEF < 1 (which implies a quenching of the total radiation) in most of the visible range, and that silver has its only peak of LFIEF ~ 3 in the near ultraviolet.

These considerations might suggest that near surfaces, even made of coinage metals, not much would be gained in terms of electromagnetic intensity, hence of Raman enhancement. While this may be true for flat surfaces, high LFIEFs may be achieved in specific conditions, in particular when the surface is nanostructured.

1.3 Surface plasmons resonance in nanomaterials

To understand exactly what happens to the electric field in the proximity of non-flat surfaces, Maxwell's equations must be solved. Unfortunately, analytical solutions for Maxwell's equations exist only for the simplest geometries. A widespread approach to the problem is the *quasi-static approximation*. The method is applicable when the incoming electric field wavelength λ is much wider than the dimensions of the object whose surface is considered, so that the incoming electric field can be considered approximately constant across the dimension of the metallic structure. Another approximation is to consider the charge distribution across the surface of the metallic object as dipolar, ignoring higher-order effects such as quadrupoles. A common threshold for the quasi-static approximation is $\lambda > 10\ l$, where l is the dimension of the metallic structure in the direction of propagation of the wave. Acknowledging visible light, this condition implies approximately that $l < 100$ nm at most, which entails an object nanostructured at least in one dimension. In the case of significantly larger dimensions, both the hypothesis of a constant electric field and of the absence of charge distributions in higher modes than dipolar are not valid anymore.

Considering the case of a nanosphere of radius a immersed in an electric field $\vec{E_0}$, which can be considered constant throughout the nanoparticle diameter and its proximity, oriented in the x direction, a gauge transformation of Maxwell's equation may be applied to obtain Laplace's equation for electrostatics:

$$\nabla^2 \phi = 0 \tag{1.21}$$

where ϕ is the electric potential, which is related to the electric field by the following equation: $\vec{E}_0 = -\nabla\phi$.

Boundary conditions for the solution of this equation are that the electric potential is continuous at the surface of the sphere, and that the orthogonal component of the electric displacement $\vec{D}_0 = \epsilon\vec{E}_0$ is continuous as well. Given that solutions to

Laplace's equation are spherical harmonics, the first harmonic can be considered, and the electric potential takes the forms, in each of the two different parts of space (inside and outside the sphere):

$$\phi = A\ r \sin\theta \cos\Phi \qquad \text{for } r < a \tag{1.22}$$

$$\phi = \left(-|\vec{E}_0| r + \frac{B}{r^2}\right) \sin\theta \cos\Phi \qquad \text{for } r > a \tag{1.23}$$

in polar coordinates (r, θ, Φ) with origin in the centre of the nanosphere, which means that the portion of space described by $r < a$ is inside the sphere, with an electric permittivity ϵ_2, while for $r > a$, outside the sphere, a dielectric with permittivity ϵ_1 is present. In figure 1.3 a scheme of this system is shown.

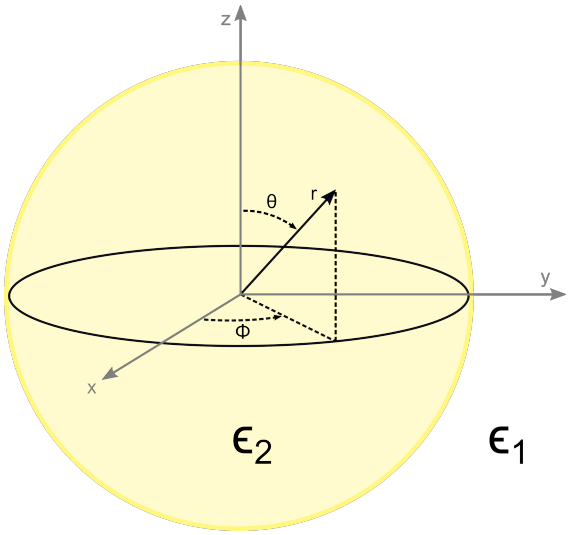

Figure 1.3: Scheme of the nanosphere in a medium in polar coordinates.

Combining these general expressions for electric potentials with the boundary conditions for the problem at hand, the coefficients A and B can be calculated to be:

$$A = \frac{-3\epsilon_1}{2\epsilon_1 + \epsilon_2} |\vec{E}_0| \tag{1.24}$$

$$B = \frac{\epsilon_2 - \epsilon_1}{2\epsilon_1 + \epsilon_2} |\vec{E}_0| \tag{1.25}$$

The total electric field outside the nanosphere can be calculated as the superposition of the incident electric field $\vec{E}_0$ and the electric field caused by the induced dipole moment $\vec{P}$. In Cartesian coordinates (mentioning again that the external

electric field is linearly polarised in the x direction, hence $\vec{E}_0 = |\vec{E}_0|\hat{x}$):

$$\vec{E}_{tot} = |\vec{E}_0|\hat{x} - \alpha|\vec{E}_0|\left[\frac{\hat{x}}{r^3} - \frac{3x}{r^5}(x\hat{x} + y\hat{y} + z\hat{z})\right] \tag{1.26}$$

in which $\hat{x}, \hat{y}, \hat{z}$ are the unitary vectors corresponding to the Cartesian coordinates and α is the polarisability, tied to the induced dipole moment by the relation: $\vec{P} = \alpha\vec{E}_0$. The polarisability is expressed by the following formula:

$$\alpha = \alpha(\lambda) = \frac{\epsilon_2(\lambda) - \epsilon_1}{\epsilon_2(\lambda) + 2\epsilon_1}a^3 \tag{1.27}$$

where the dependency of the electric permittivity of the metal $\epsilon_2(\lambda)$ and the polarisability $\alpha(\lambda)$ on the wavelength is explicitly stated, while that of the dielectric medium ϵ_1 is not, since the nanoparticles are usually immersed in a vacuum or air and it can be approximated as real and constant with respect to the electromagnetic wavelength in the visible range, while the permittivity of a metal is much more influenced by λ and has a non-negligible imaginary part.

The latter equations show that the intensity of the electric field outside a sphere is dependent on the incident electromagnetic wavelength, and can be heavily influenced by the choice of materials as well. In fact, when the denominator in expression 1.27 approaches zero, the polarisability, hence the electric field at the surface of the nanoparticle, increases greatly (effects which are ignored in this simplified treatment of the problem, for example the presence of an imaginary part of $\epsilon_2(\lambda)$, prevent the factor to increase indefinitely). This resonance condition is thus achieved when:

$$\epsilon_2(\lambda) = -2\epsilon_1 \tag{1.28}$$

in which again the dependency of ϵ_1 on the wavelength is ignored. This explains the great amplification of the LFIEF, hence the SERS enhancement, on the surface of some spherical metallic nanostructures.

In figure 1.4, the LFIEFs on surfaces of nanospheres of gold and silver are reported. It is evident that high LFIEFs can be attained by selecting the appropriate excitation wavelength, especially with silver. Note that the point of the surface taken into account in the figure is one of the end points of the diameter of the sphere parallel to the electric field. The volumes (external to the sphere) around this point and its polar opposite are the portions of space which exhibit the highest LFIEFs, and from which most of the SERS amplification arises, therefore they are commonly named *hotspots*. The nature of the dielectric surrounding the sphere, as well as the properties of the metal, determines the frequency of this resonance.

In figure 1.5, the same results of LFIEF calculations (again at the hotspots, which are again located at the extremes of the diameter parallel to the electric field) are shown for a two-dimensional geometry: the infinite-length cylinder with

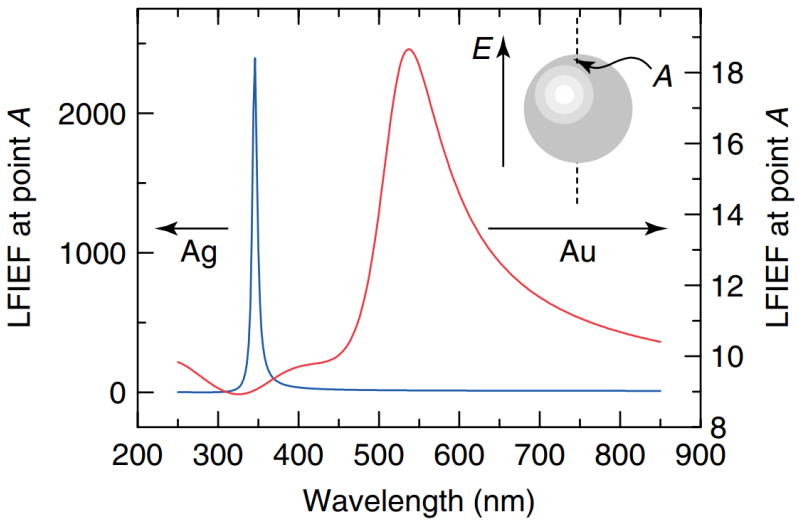

Figure 1.4: Local field intensity enhancement factors of silver and gold nanospheres in air as functions of electromagnetic wavelength. Inset shows the position of the considered point with respect to the polarisation of the incoming electric field, close but external to the metallic sphere. Reprinted with permission from [2]. Copyright © 2010, John Wiley and Sons.

nanometric radius, which can be analytically approached as well. In this case the induced dipole moment is proportional to:

$$|\vec{P}| \propto \frac{\epsilon_2(\lambda) - \epsilon_1}{\epsilon_2(\lambda) + \epsilon_1} \tag{1.29}$$

which yields lower LFIEFs than the nanosphere and has a different resonance condition as well, at:

$$\epsilon_2(\lambda) = -\epsilon_1 \tag{1.30}$$

The differences between the resonance conditions of the polarisabilities of the sphere and the cylinder suggest that the geometry of the particles is heavily influential on the resonance. This is in fact true, and is often used to improve the resonance of the SERS/TERS systems with the available excitation wavelength. This topic will be analysed in section 1.4.

Figures 1.4 and 1.5 report the LFIEF values for silver and gold structures. However, LFIEF is not a measure of the amplification of Raman per se. A quantity similar to the LFIEF which refers instead to the amplification of Raman signals with respect to the Raman intensity that would arise from a material if the enhancing surface were not present, the *enhancement factor* (EF), can be introduced for this purpose. When an analyte is approached to the particle surface, the amplification

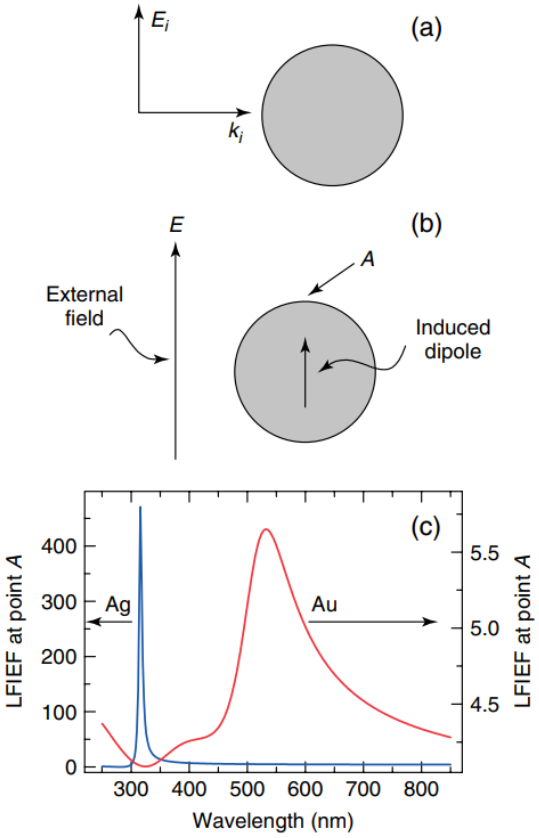

Figure 1.5: (a), (b): schematic representations of the two-dimensional (infinite length) nanowires considered for the following calculations, and indication of the position of considered point A, close but external to the metal, with respect to an external electric field. (c): local field intensity enhancement factors of silver and gold nanowires, as functions of wavelength, on point A. Reprinted with permission from [2]. Copyright © 2010, John Wiley and Sons.

of the electric field which the LFIEF describes is not only applied to the incident electric field, but to scattered light as well. In the approximation of Raman-scattered light having the same frequency as the excitation wavelength, which of course holds better the lower the Raman shift of the considered vibration signal is, the EF can be put in relation with the LFIEF with the following formula:

$$\mathrm{EF} = \frac{I}{I_0} = \frac{\zeta\ \mathrm{LFIEF}\ I_{in}}{\zeta|\vec{E}_0|^2} = \frac{\zeta\ \mathrm{LFIEF}|\vec{E}_0|^2\ \mathrm{LFIEF}}{\zeta|\vec{E}_0|^2} = \mathrm{LFIEF}^2 = \left(\frac{|\vec{E}|}{|\vec{E}_0|}\right)^4 \quad (1.31)$$

in which I and I_0 are the Raman intensity that arises with the surface and the intensity which would be without, I_{in} is the intensity of the incident field amplified by the metallic structure, therefore $I_{in} = \mathrm{LFIEF}|\vec{E}_0|^2$; $\vec{E}$ and $\vec{E}_0$ are the electric

fields present with and without the nanoparticle (hence $\vec{E}_0$ is the incident field), and ζ is the proportionality factor of the Raman scattered light with respect to the incident light, taking into account that the two are indeed directly proportional.

Of course, removing the approximation stating that the LFIEF on the excitation wave is equal to that on the Raman scattering:

$$\mathrm{EF} = \mathrm{LFIEF}(\lambda_{ex})\ \mathrm{LFIEF}(\lambda_{em}) \tag{1.32}$$

where λ_{ex} is the wavelength of the exciting radiation, and λ_{em} is the absolute wavelength of the acknowledged Raman band.

The enhancement factor is also dependent on the distance of the analyte with respect to the plasmon-resonant surface, as it is generated by it. While the substance is not required to be strictly in contact with the nanoparticle for the SERS effect to arise, the amplification is stronger in the immediate proximity of the surface, and rapidly decays with distance. Considering a metallic nanosphere with radius a, the electric field enhancement scales with the distance from the centre of the plasmonic structure r proportionally to r^{-3}. Employing the $|\vec{E}|^4$ approximation, the EF distance dependence is therefore proportional to r^{-12}, and taking into account that the surface scales with r^2, the following expression is approximately valid:

$$\mathrm{EF}(r) \propto \left(\frac{a+r}{r}\right)^{-10} \tag{1.33}$$

The Drude model, modified to keep into account interband transitions, can explain why the dimensions of the nanoparticles in SERS have a lower limit in order for them to be effective Raman enhancers. The electric permittivity ϵ of a metal can be expressed with this modified model as follows:

$$\epsilon(\omega) = \epsilon_b + 1 - \frac{\omega_p^2}{\omega^2 + i\omega\gamma} \tag{1.34}$$

in which ϵ_b is the altering term with respect to the simpler Drude model expression, which plays a role in the calculation, for example, for gold when $\lambda < 500$ nm, and γ is again the electron scattering rate, inversely proportional to the electron mean free path in the lattice. The polarisability of a small conductive sphere of radius R in a vacuum is:

$$\alpha = \frac{\epsilon - 1}{\epsilon + 2}\ R^3 \tag{1.35}$$

Combining these last two equations, an expression for the polarisability of this sphere as a function of the electromagnetic angular frequency ω can be extracted:

$$\alpha(\omega) = \frac{(\epsilon_b\ \omega^2 - \omega_p^2)R^3 + i\omega\gamma\epsilon_b}{\left[(\epsilon_b + 3)\ \omega^2 - \omega_p^2\right] + i\omega\gamma(\epsilon_b + 3)} \tag{1.36}$$

The polarisability thus obtained has a sharp maximum when $\omega = \frac{\omega_p}{\sqrt{\epsilon_b+3}}$; the width of this resonance is $\Delta = (\epsilon_b + 3)\gamma$. Therefore, if γ or ϵ_b are large, the resonance quality is reduced. Bulk coinage metals such as gold and silver have high conductivity, therefore low γ, but this factor begins to increase when the length of the metal approaches the mean free path, and gets smaller if the dimensions of the nanostructure are decreased. Because of this reason and the limits of the quasi-static approximation, SERS nanoparticles are usually efficient in a dimension interval between 10 nm and 100 nm, and the EFs exhibited by these scatterers rapidly decay above or below these limits.

1.4 Variables affecting plasmon resonance

The differences between the polarisability of the nanosphere and the nanocylinder suggest that the geometry of the particles is heavily influential on their resonance spectra. This is in fact true, and in SERS/TERS the shape of the nanoparticles is often engineered to improve the resonance of the system with the available excitation wavelengths.

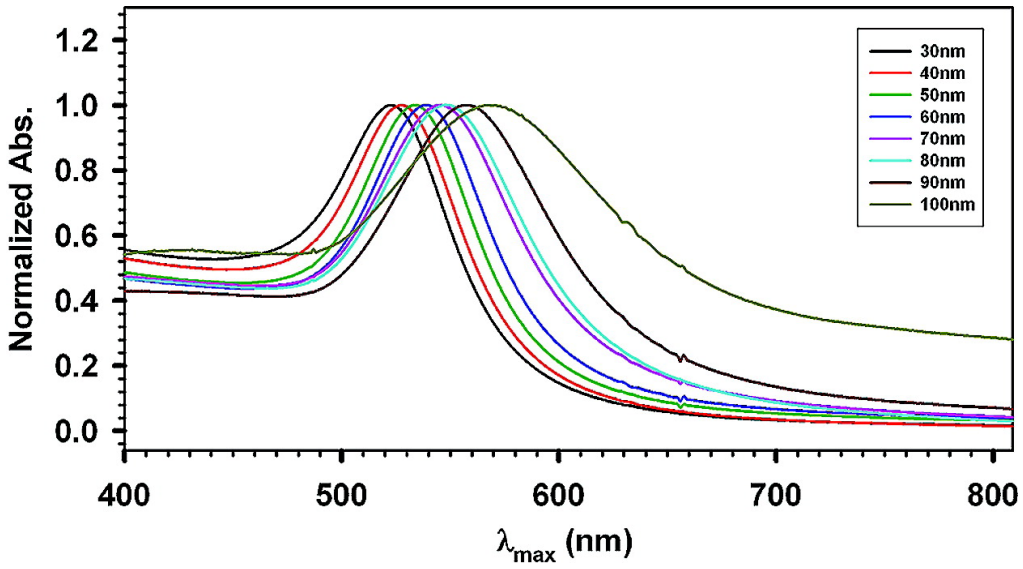

Figure 1.6: Normalised UV-Vis spectra of gold nanoparticles of different sizes in aqueous solution. A red shift of the plasmon resonance as the particles increase in size is visible. Reprinted with permission from [3]. Copyright 2007 American Chemical Society.

One of the most important factors for plasmon resonance is, not surprisingly, nanoparticle size. Assuming the quasi-static approximation, the problem becomes scale-invariant, as the dimension of the nanoparticle is not considered. Nevertheless, this approach requires the wavelength of the exciting radiation to be much greater than the dimension of the metallic structure. As already stated, the approximation does not hold for sizes much higher than 100 nm for spherical geometries and visible wavelengths. Even below this limit, the factor has an effect on the plasmon resonance. As heuristically understood, the resonance is subject to red shift when the nanoparticle size is increased. The intensity of the resonance tends to decrease as well with the accretion of the object, as a result of increased radiation losses, which worsen the resonance quality and the LFIEF, hence the EF. Larger structures also result in the activation of multipolar resonance modes, which in turn cause the occurrence of new peaks and alterations in the LFIEF resonance spectra with respect to the dipolar approximation. Figure 1.6 shows the shift in plasmon resonance of nanometric objects of different sizes.

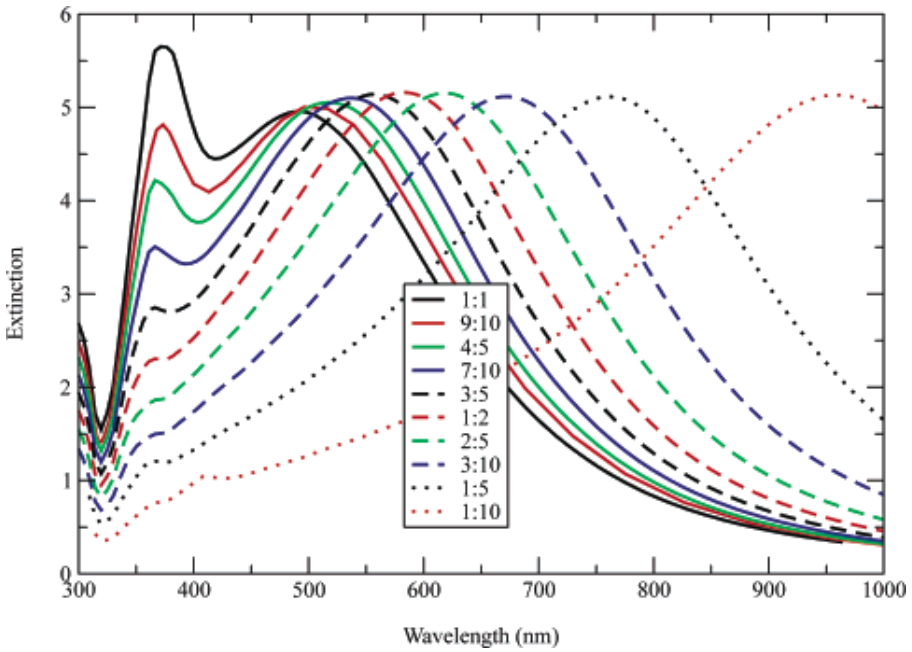

Figure 1.7: Calculated extinction spectra of oblate spheroids with different aspect ratios with the same volume (equivalent to the volume of a sphere of radius 80 nm). The spectra are normalised. Reprinted with permission from [4]. Copyright 2003 American Chemical Society.

The nanoparticle shape influences the plasmon resonance as well. Exact electrodynamic calculations can be carried out for oblate and prolate spheroids, which can be taken as examples and compared to isotropic nanospheres. The problem can be solved with the same quasi-static approach employed before. The aspect ratio of the spheroids can be factored in by a shape value ξ, which is a function of the two different axes of the spheroid:

$$\xi = \left(\frac{b^2}{a^2} - 1\right)^{-\frac{1}{2}} \tag{1.37}$$

where a and b are the two axes of the spheroid in question, and $b \geq a$. The aspect ratio influences the polarisability of the spheroid with a shape factor χ:

$$\chi = -1 - 2\left[\xi^2 - \frac{\xi\ (\xi^2 + 1)}{2} \cos^{-1}\left(\frac{\xi^2 - 1}{\xi^2 + 1}\right)\right]^{-1} \tag{1.38}$$

The spheroid polarisability is:

$$\alpha = \frac{\epsilon_2 - \epsilon_1}{\epsilon_2 + \chi\epsilon_1} \frac{b^3(1 + \chi)\xi^2 + 1}{3\xi^2} \tag{1.39}$$

using the same notation as the last section for the electric permeabilities ϵ_j. Calculated extinction spectra for oblate spheroids of different aspect ratios are shown in figure 1.7.

In general, less basic shapes than spheres and cylinders are likely to have more than one resonance peak and more complicated LFIEF functions. Different zones of the surfaces of the objects may also have different LFIEFs, and their maxima may be at separate wavelengths. An example of this can be observed in figure 1.8. In this figure, a good example of *lightning rod effect* (LRE) for surface- and tip-enhanced Raman is visible, which is the concentration of electric fields at the apices of sharp features. This is a separate, although related, phenomenon with respect to the classic lightning rod effect, which arises in a truly electrostatic system, since the LRE in SERS occurs with oscillating electric fields at visible frequencies. Anisotropic three-dimensional shapes can also induce much higher LFIEFs than the sphere, especially if they present sharp features, because of the LRE. It is also noteworthy that the orientation of a non-isotropic nanoparticle can be very influential on the magnitude and profile of the LFIEF. When the LRE has a significant contribution to the total electric field, the highest LFIEFs, therefore the best EFs, are achieved when the polarisation of the incident light is parallel to the bisector of the angle of the pointed feature on the surface of the nanoparticle. The LRE and the correct polarisation of the excitation electric field is an essential part in the achievement of tip-enhanced Raman spectroscopy, which will be discussed in more detail in section 1.5.

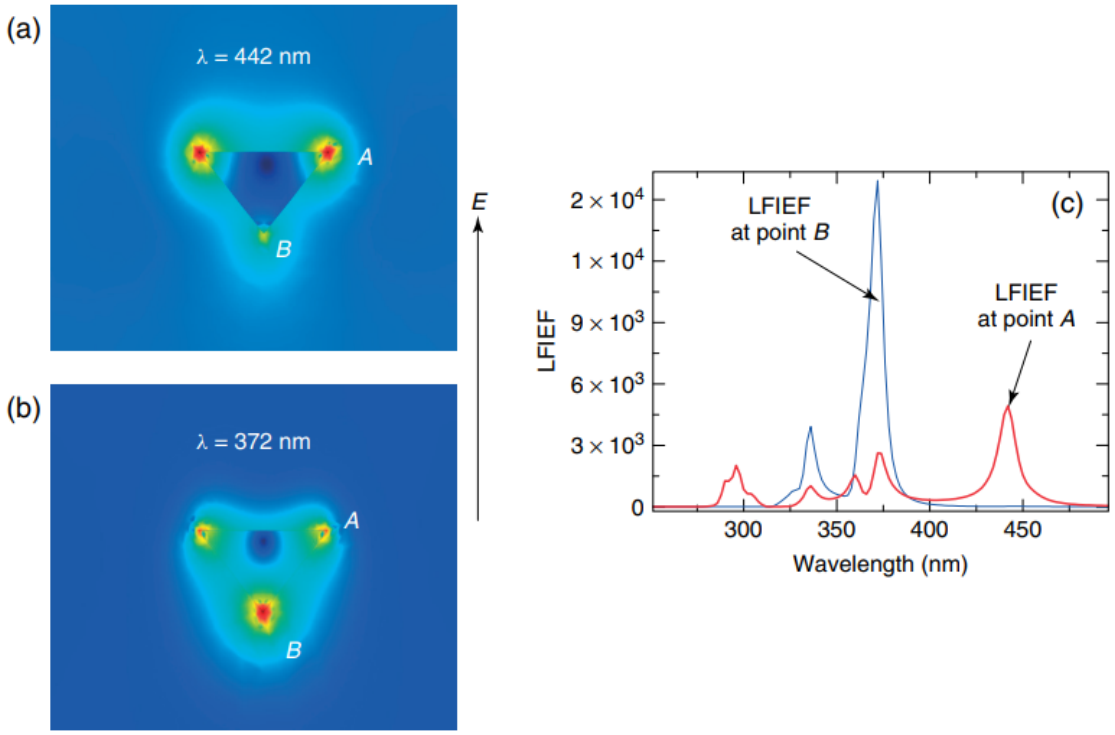

Figure 1.8: Local field intensity enhancement (LFIEF) of a triangular silver nanoparticle excited by a linear electric field, showing the plasmonic lightning rod effect. (a): intensity LFIEF map in a logarithmic false colour scale (red: highest, blue: lowest) considering a 442 nm wavelength. (b): the same map for a wavelength of 372 nm. (c): LFIEF as a function of wavelength considering two different points on the nanoparticle surface A and B, indicated in the maps. Adapted with permission from [2]. Copyright © 2010, John Wiley and Sons.

Another factor that affects the plasmon resonance of a nanoparticle is its surroundings. As inferred by the previously presented equations, the dielectric function of the medium ϵ_1 in which the metal is immersed alters the polarisability function. This effect is sometimes employed for "plasmon tuning" in SERS and TERS by coating the scattering nanostructures with a dielectric layer of specific permittivity and thickness to shift the resonance peak to a more convenient value (while preserving the metallic surface from undesired chemical reactions as well). Plasmon resonances in fact are subject to greater red shifts the higher the electric permeability of the medium is. Figure 1.9 shows the scattering cross section of a gold nanoparticle immersed in dielectrics with different refractive indices.

Another important effect related to the environment in which the nanoparticle resides, and a phenomenon of most interest for SERS and TERS, is *plasmon coupling*. When a nanoparticle is in proximity with another metal structure, such

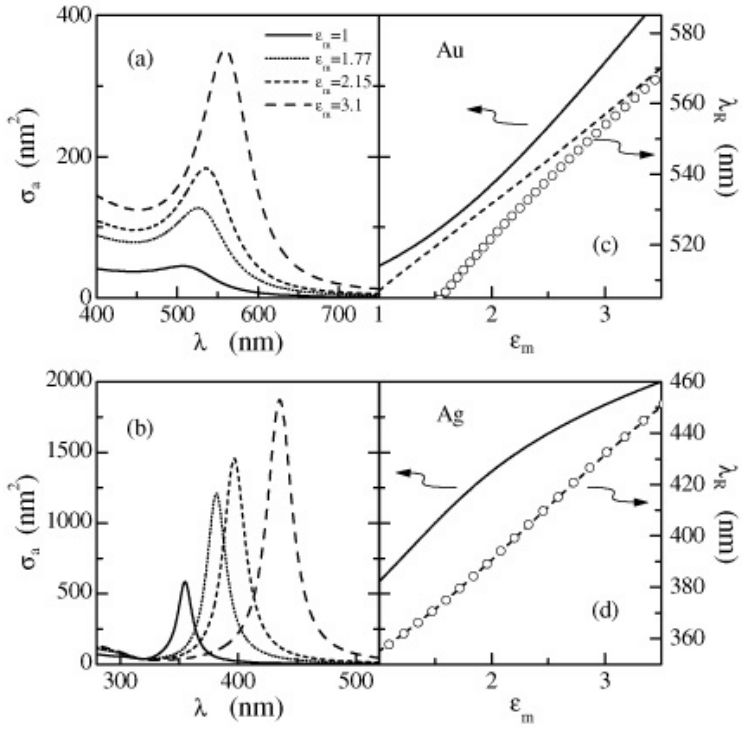

Figure 1.9: Left: absorption cross sections of single gold (a) and silver (b) nanospheres (with 15 nm diameters) embedded in dielectric matrices with different permittivities ϵ_m. Right: surface plasmon resonance (SPR) wavelengths λ_R (dashed lines), absorption cross sections at SPR maxima (full lines), and λ_R calculated with equation 1.28 (dotted line) of the same gold (c) and silver (d) spheres as functions of the permittivity of the surrounding medium ϵ_m.

as the case of two significantly plasmon-resonant nanospheres, the dipole effects induced by an external electric field, hence the plasmon oscillations of each, tend to interfere with each other. This process tends to be significant when the structures are closer than ∼20 nm, approximately the lateral dimension of the hotspot, and the electric field has a component oriented in the direction of their mutual distance, which is, in this example, the direction connecting the centres of the spheres.

In detail, the coupled resonance tends to strongly magnify the LFIEF in a small region between the two surfaces with respect to the superposition of the solutions to the problem considering isolated SPRs. For instance, in the case of a dimer comprised of identical silver nanospheres of radius 25 nm immersed in air, separated by a distance of 2 nm, and excited by an electric field parallel to the dimer long symmetry axis, numerical simulations suggest that 80% of the SERS signal generated by a uniform distribution of molecules in the space around the spheres

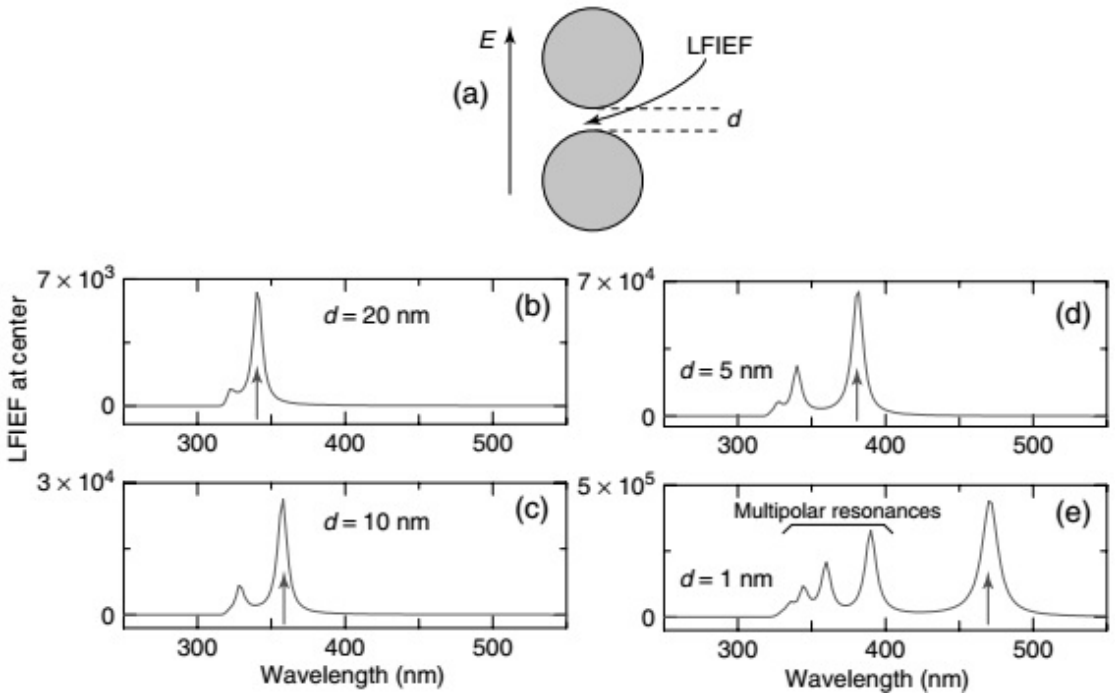

Figure 1.10: Local field intensity enhancement factors (LFIEFs) in dimers formed by two identical 50 nm radius silver cylinders (a), separated by different distances d, calculated in the electrostatic approximation in the center of the dimer. (b): $d = 20$ nm. (c): $d = 10$ nm. (d): $d = 5$ nm. (e): $d = 1$ nm. The LFIEFs grow when the separation decreases, and multipolar resonances effects start to consistently contribute to the spectra at shorter distances. Adapted with permission from [2]. Copyright © 2010, John Wiley and Sons.

is yielded only by the 0.64% of the molecules which reside in a circle delimited by a 9° angle around the dimer axis traced from the centre of the nanospheres. The substances in this dimer region experience Raman enhancements up to 10^7 times larger than the rest. Taking advantage of the boost in the SERS EF occurring in the gap between plasmonic surfaces, which also occurs to a lesser degree when a single nanostructure is put in proximity to a flat conductive surface with appropriate electric permittivity, the already substantial limit of detectability of SERS can be furtherly lowered. This is often the preferred setup for single molecule detection in SERS and TERS. This arrangement is sometimes referred to as *gap mode*. In figure 1.10, differences in the LFIEF(λ) profiles in SERS nanoparticle dimers with different separation distances are displayed. Figure 1.11 shows the difference in the electric field intensity in TERS arising from an isolated tip and a tip in proximity to a flat gold surface (i.e. in gap mode).

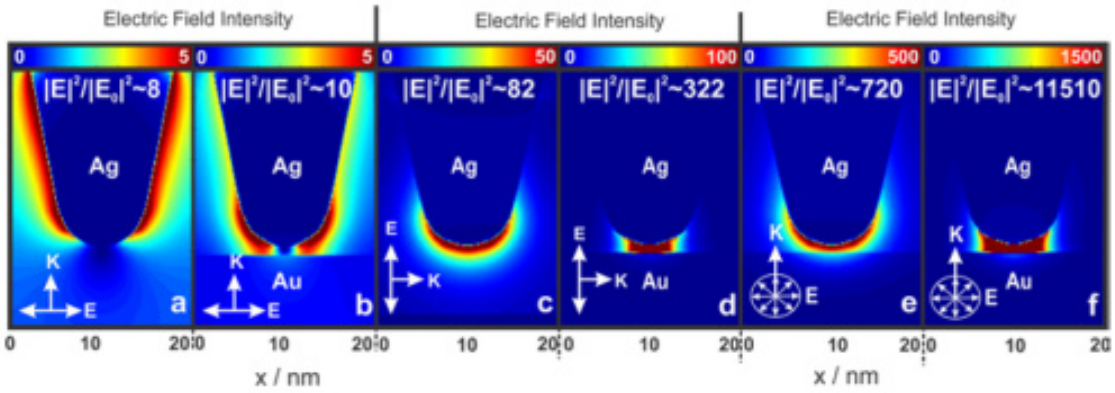

Figure 1.11: Finite-difference time-domain calculations of the electric field intensity distribution at the apex (radius $r = 10$ nm) of a silver tip illuminated by a 532 nm excitation wavelength with different polarisations. (a): isolated tip, light polarisation orthogonal to the tip axis. (b): tip approached to a flat gold surface (1 nm distance), polarisation orthogonal to the tip axis. (c): isolated tip, polarisation parallel to the tip axis. (d): tip approached to a flat gold surface (1 nm distance), polarisation parallel to the tip axis. (e): isolated tip, radial polarisation. (b): tip approached to a flat gold surface (1 nm distance), radial polarisation. Reprinted with permission from [6].

1.5 Tip-enhanced Raman spectroscopy

The topic of this thesis, tip-enhanced Raman spectroscopy (TERS), derives from the considerations examined in the previous sections. Since its conception and its first experimental demonstration, published in the year 2000 by *Stöckle, et al.* [7], TERS has found increasing applications in diverse research fields such as material science, electronics, and biology. This novel measurement technique is achieved by coupling SERS with scanning probe microscopy (SPM): in TERS a single nanoparticle, in the form of a specifically manufactured SPM tip, is illuminated by a laser beam which is focussed by a high-magnification optical microscope objective on the probe apex; the radiation is then collected and analysed with a Raman spectrograph, as in SERS. The combination of surface plasmon resonance by a tuned electric field aligned to the tip axis and the lightning rod effect result in a very high Raman enhanced spectrum arising from the nanometric hotspot which forms at the apex of the SPM tip, which in most cases is comparable or more

intense than the background signal originating from the rest of the illuminated volume. Figure 1.11 shows the influence of the direction of the electric field on the LFIEF in TERS measurements.

The spatial resolving power of optical microscopy (therefore that of regular SERS as well) is limited by diffraction, and it can be estimated with the Rayleigh criterion, which states that the minimum distance between two resolvable point with this technique is:

$$\delta = \frac{1.22\ \lambda}{2n \sin\theta} \approx \frac{\lambda}{2 \text{ to } 3} \tag{1.40}$$

where θ is the maximum half-angle of the cone of light focussed by the microscope objective lens, n is the refractive index of the medium, and λ is the light wavelength. A widespread rule of thumb for this limit is to consider as δ half of the wavelength, at most approximately 200 nm to 350 nm for visible light. Since most of the Raman signal in TERS arises from the hotspot, with significantly smaller dimensions than the diffraction-limited volumes investigated with unaided Raman and SERS, it can be understood how TERS is able to significantly improve the spatial resolution of Raman while, at the same time, achieving single molecule detection. Because the probe is guided with a SPM system, TERS is able to concurrently acquire chemical images of surfaces by SERS and to map their topography by SPM, which itself is capable of measurements well below the diffraction limit, and in certain conditions may achieve atomic resolution.

TERS probes must conform to the strict conditions dictated by surface plasmon resonance discussed in the last sections of this chapter. To achieve this, almost all TERS tips have apices with curvature radii <100 nm, and whose surfaces are made of either gold or silver. Probes for SPM have specific requirements of their own, which are imposed by the chosen SPM feedback, that is the probe-sample interaction measured by the system to drive the tip on the surface. The most popular choices for TERS are atomic force microscopy (AFM) and scanning tunnelling microscopy (STM).

AFM is governed by the van der Waals forces between the probe and the sample, sensed by the position of a laser spot reflected on the cantilever, which is an elastic strip on which the tip is attached. The laser path is precisely correlated to the forces exerted on the apex by the deflection of the cantilever (a *light lever*). Because of the cantilever requirements of AFM probes, TERS tips employed in this mode are often standard AFM probes coated with silver or gold. Van der Waals energy between two atoms follow a distance dependency which is approximated by the Lennard-Jones potential:

$$U(r) = U_0 \left[\left(\frac{r_0}{r} \right)^{12} - 2 \left[\frac{r_0}{r} \right]^6 \right] \tag{1.41}$$

in which r is the distance between the atoms, U_0 is a constant, and r_0 is the equilibrium distance, which is also the minimum of this function. The term elevated at the 12^{th} power takes in account the ionic repulsion forces that arise at very short range because of the Pauli exclusion principle, while the term at 6^{th} power is the contribution of longer range dipole-dipole attraction between atoms.

AFM-TERS is advantageous as it can be employed on virtually every surface, but the presence of stray radiation by the light lever laser may interfere with Raman spectra. In addition, lower EFs are reported in literature with AFM-TERS with respect to those acquired with STM-TERS, most likely because of the core of the AFM-TERS tips, which cannot be made of SERS-active materials such as gold or silver due to their softness, that influences the plasmon resonance. Another issue is the probe-sample distance: in contact mode this can be lower than 1 nm, but in AFM the apices in contact with surfaces can easily become contaminated and constantly wear out during scans (this phenomenon is more influential for tips coated with the soft metals necessary for TERS); in semi-contact and non-contact modes, the average tip-analyte distances are much greater (generally >5 nm), which implies lower enhancements.

The measured interaction during STM is instead the tunnelling current between the probe and sample surface when they are electrically polarised with respect to each other in a conductor-insulator-conductor junction. STM can be performed on (doped) semiconductors when the appropriate polarisation conditions are applied. Measurable tunnelling currents arise if the distance between conducting materials is in the order of magnitude of 1 nm, when the tunnelling effect of electrons is relevant. The effect results in a net tunnelling current density $j_t(V)$ when the junction, polarised by a voltage V, varies by a distance between the electrodes Δz. This current density has the following expression:

$$j_t(V) = j_0(V)\ e^{-\frac{2}{\hbar}\sqrt{2m\phi}\ \Delta z} \qquad \text{for} \qquad eV \ll \phi \tag{1.42}$$

for metal-insulator-metal junctions, where $\hbar$ is the reduced Planck constant, ϕ the work function of the metal (typical values are $\phi \sim 4$ eV), and e and m are the electron charge and mass respectively. The function indicates an exponential decay of the current when the probe is retracted from the sample: for a work function of $\phi = 4$ eV, the exponential attenuation factor is $\sim$2 Å^{-1}, which suggests that increasing the tip-sample distance by 1 Å results in a decrease of the tunnelling current of approximately an order of magnitude. Because of this extreme sensitivity to distance, almost 90% of the STM current originates from the atom of the tip closest to the surface. With an effective probe size of a single atom, STM is capable of atomic resolution.

STM-TERS does not require specific probe geometries, therefore it is possible to employ full-metal tips. This, along with the small and finely controllable apex-sample distance, usually results in stronger Raman enhancements than AFM-TERS and exceptional spatial resolution as well. The most glaring limitation of STM-TERS is that the sample surface cannot be insulating.

As of today, spatial resolutions of 1.7 nm in ambient conditions and atomic resolution in ultra-high vacuum have been reported with TERS; the technique has been increasingly popular for analyses on single molecules as well as for measurements in liquids, which comprise convenient mediums for studies on catalysis and on biological systems. [2–38]

Part II

Experimental

Chapter 2

Experimental setup

In order to attain tip-enhanced Raman scattering, the illumination of the apex of an appropriate Raman-enhancing probe by a monochromatic, polarised light source, usually a laser, is needed. To maximise TERS excitation power density while minimising unsought irradiation and consequent background signals from the volume surrounding the hotspot, light is focussed on the tip by means of a high-magnification microscope objective. The enhanced Raman signal must be collected, and its spectrum has to be analysed with a spectrometer, usually after filtering out the much more intense Rayleigh scattering radiation. Usually a confocal microscopy system is employed, in order to block most out-of-focus light. The typical TERS setup therefore consists of the following elements:

- Scanning probe microscopy system
- TERS probe
- Excitation laser
- Optical microscope objective (for excitation)
- Optical microscope objective (for collection)
- Notch or edge filter
- Monochromator
- Confocal microscopy system
- Raman spectrometer
- Insulation from light, vibration, environment, sound...

2.1 Apparatus geometry

Several practical realisation types of TERS systems exist. In figure 2.1, top-, side- and bottom-illumination setups are illustrated while applied to AFM-based TERS (for this nomenclature, the probe is assumed to be placed above the sample), although other configurations were reported in literature as well. In figure 2.1a and 2.1b, the experimental setup employed in this thesis is shown, a *top-illumination* system. For top-illumination, also called *upright* or *top-visual*, a special (top-visual) AFM probe is necessary (this type of tip is sometimes referred to as *corner tip*, or *tip at the end of the cantilever*). This kind of probe differs from the most common AFM probes (shown in figure 2.1c and 2.1d) because of

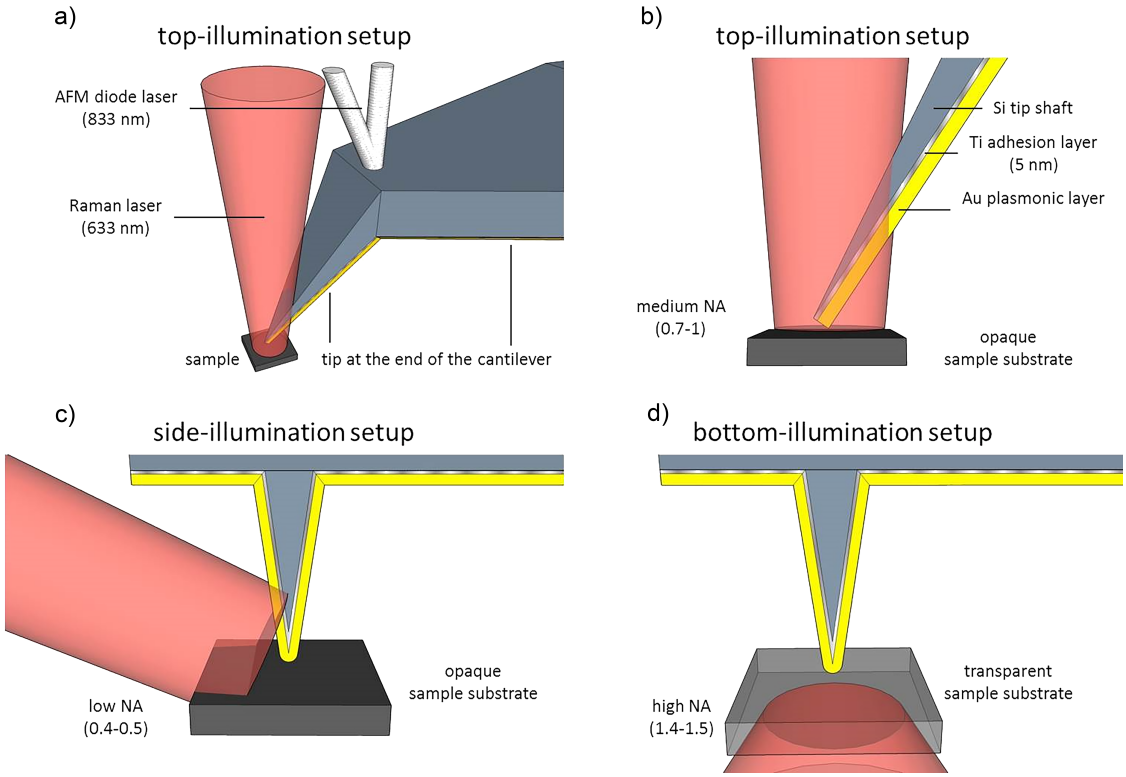

Figure 2.1: Schematic diagrams of different configurations developed for objective-based TERS, applied to AFM-TERS with a gold plasmonic layer and a 633 nm excitation laser. Overall perspectival view of the top-illumination setup employed in this thesis (a), and cross-sectional views of top- (b), side- (c), and bottom-illumination (d) setups. Note that gold adhesion to the silicon is aided by a titanium layer for the probes in figure. The schemes (a) and (b) depict the configuration employed in this thesis.

the position and the orientation of the shaft with respect to the cantilever: it is possible to see the apices of these top-visual tips both from above and below, when placing the cantilever horizontally on the sample surface, since the probe shaft is slightly tilted with respect to the perpendicular to the cantilever, which is the optimal geometry for enhancement with a vertical excitation polarisation. The top-visual AFM probes employed in this work have their tip shafts at an 83° angle with respect to the cantilevers, instead of the 90° of normal AFM probes, which cannot be utilised in top-visual systems because of the shadow effect from the cantilever.

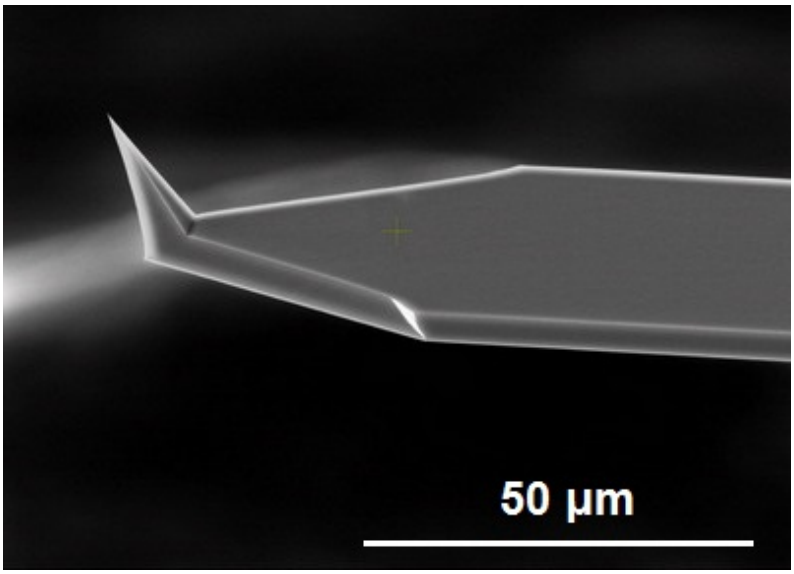

Figure 2.2: Scanning electron microscopy image of a *VIT_P* AFM probe, in which its special geometry as a "tip at the end of the cantilever" can be appreciated. The particular probe depicted in the image is pristine, made of pure monocrystalline silicon without any plasmonic layer. © NT-MDT™ SI.

The total absence of cantilever shadow effects and almost negligible coverage of the apex by the tip shaft allows illumination and collection of the signal from the top. For STM measurements in a top-visual apparatus, the probe has to be placed slightly tilted as well, in order to achieve a geometry equivalent to the one shown in figure 2.3.

To overcome the cover effect of the cantilever or the probe shaft while utilising standard probes, bottom- or side-illumination can be employed (figure 2.1c). While top- and bottom-illumination setups employ a single objective for both excitation and collection, side-illumination may use two distinct optical paths and objectives for these purposes. The main disadvantage of top and side configurations is the need of a long working distance objective, necessary to fit the probe between the

sample and the collection lens itself: from this the inability arises to employ optics with the highest numerical apertures (NA) available in the medium of choice, which would allow maximum illumination and collection efficiencies. Objective-apex distances in a side-illumination apparatus are particularly high, hence the NA in such systems is usually the lowest of the three configurations. In figure 2.1d the bottom-illumination configuration is illustrated: the use of a transparent substrate allows the use of water- or oil-immersion objectives for maximum NA without the need of special probe geometries. The greatest limitation of bottom-illumination with respect to the other arrangements is the need of transparent substrates, because of their complete inability to measure the surfaces of opaque or bulk samples.

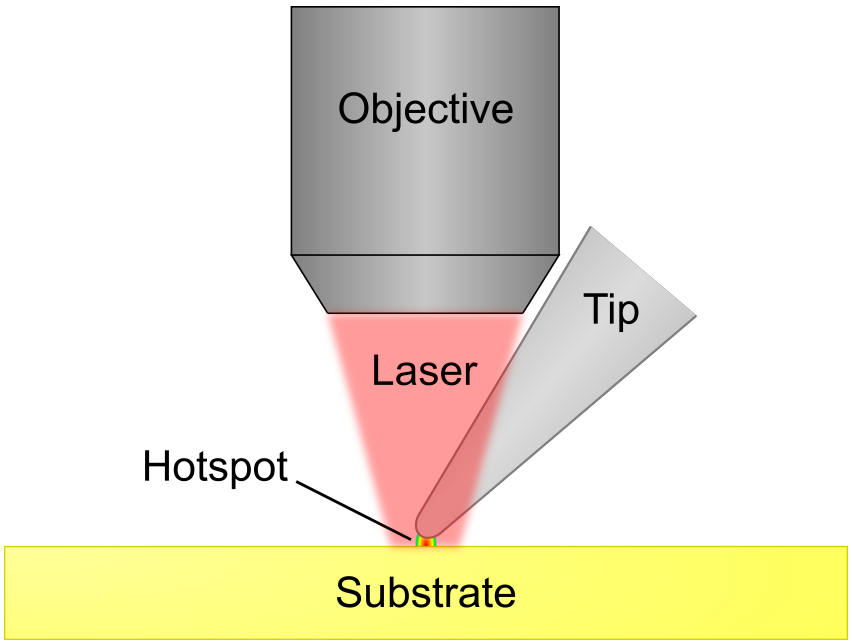

Figure 2.3: Scheme of a top-visual TERS apparatus in function. The objective focusses light on the apex of the tip, which must be slightly tilted in order for its shaft not to obscure the hotspot. Since the tips fits between the sample and the objective, the latter has to have a long working distance.

The experimental apparatus employed in this thesis is, as previously stated, top-illumination. This specific realization of a TERS system is made by coupling a standalone SPM apparatus with a commercial Raman spectrometer, both specifically modified for the task.

2.2 Raman spectrometer

A commercial dispersive Raman system, a *DXR™ Raman Microscope* by Thermo Scientific™, is employed both as a Raman excitation source and as a spectrometer for the filtering and the spectral analysis of the collected scattered TERS radiation.

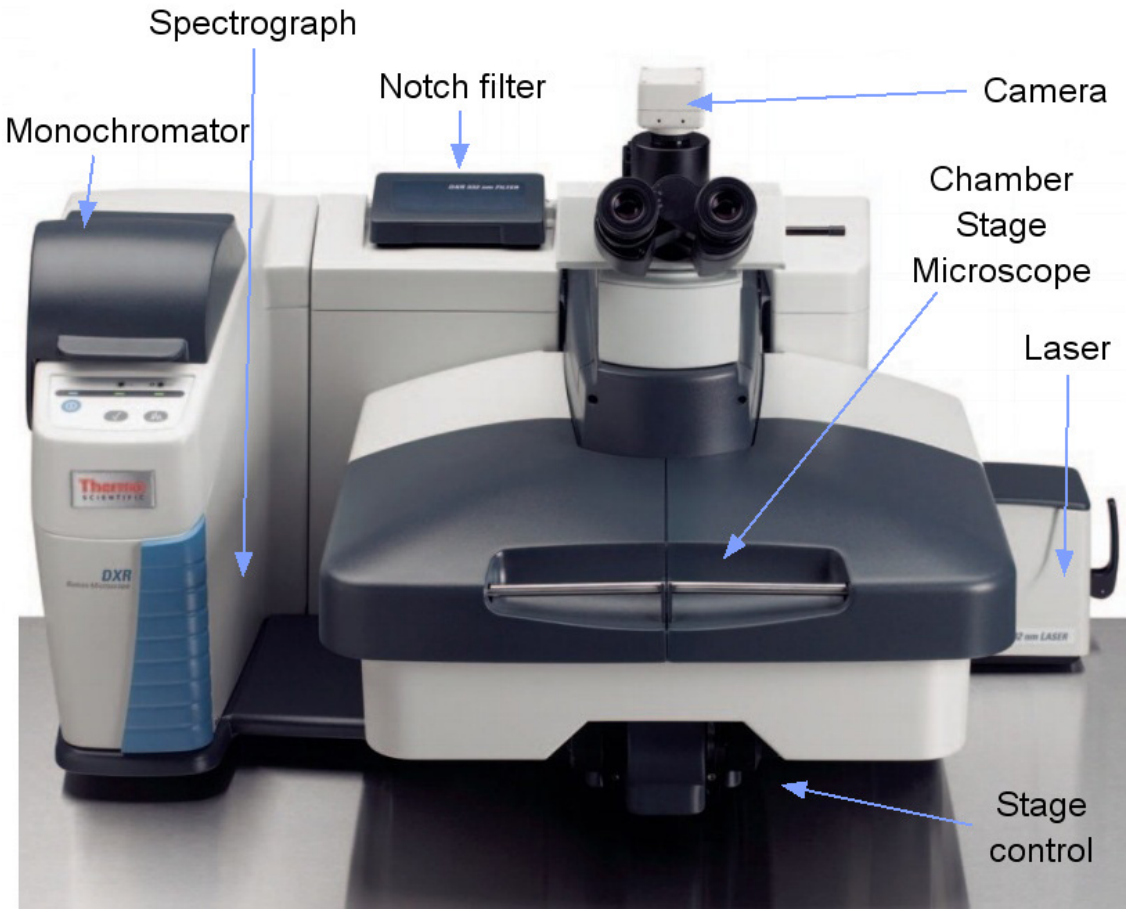

Figure 2.4: Picture of a standard DXR™ Raman Microscope, with relevant parts indicated. Note that the DXR stage, oculars and optical camera are not in use during TERS measurements, since they are replaced by the SPM equivalent equipment. © Thermo Fisher Scientific.

A picture of a standard DXR™ Raman Microscope is shown in figure 2.4. The DXR™ Raman Microscope is characterised by its flexibility: this machine stands out for the possibility of changing spectral resolution and range by switching

diffraction gratings in the monochromator and rapidly equipping different excitation lasers. This is especially useful when performing resonant Raman and plasmon-enhanced Raman (SERS, TERS), because a prerequisite for these techniques is the wavelength matching of the excitation radiation with a range of frequencies. In particular, the excitation lasers available in this specific system are the 532 nm solid state, diode-pumped, frequency doubled Nd:YAG, and the electrically pumped 633 nm He-Ne gas. Both sources work continuously. For the former, the exit laser spot diameter is <3 mm, and the power range available is 0.1 mW – 10 mW, while the diameter of the latter beam is approximately 2 mm, and its power range is 0.1 mW – 8 mW. These power ranges are measured at the source by an internal power meter: the power is continuously monitored and automatically adjusted by a feedback connected to the power regulator (a mirror of varying transmittance along its surface, moved by a servo motor when needed). Polarisation scramblers are employed on standard instruments of this type to depolarise the beams, but they were removed on the modified model utilised in this work.

The DXR™ Raman Microscope is characterised by having few moving parts, the only ones being internal lenses for the alignment of the excitation and collection paths. They are always blocked except during the alignment procedures needed for optimisation or after laser or monochromator grating exchange. This spectrometer records the entire spectrum of interest in a single window. The instrument employs edge filters for cutting out the Rayleigh scattering gathered during the acquisition, which filter out radiation with Raman shift less than $\sim$50 cm^{-1}. The sensor of the spectrometer is a charge-coupled device (CCD) detector array, composed of 1790 columns of pixels by 200 rows. The microscope is confocal: four confocal apertures can be chosen: two slits (25 µm, 50 µm) and two pinholes (25 µm, 50 µm). Smaller apertures cut out more out-of-plane light, but also reduce the intensity of the overall signal. In the monochromator, two types of diffraction gratings are available: a "full range" grating (600 lines/mm), with an average spectral resolution of 5 cm^{-1}, dependent on the wavelength, and a spectral range between 50 cm^{-1} and 3500 cm^{-1}, and a "high resolution" diffraction grating (900 lines/mm), with a lowered spectral range of 50 cm^{-1} to 1800 cm^{-1}, but a better average spectral dispersion of 3 cm^{-1}. The instrument allows exclusively the detection of Stokes scattered radiation.

2.3 Scanning probe microscope

The SPM element of the TERS apparatus employed in this thesis is based on the *Ntegra* scanning probe microscope, manufactured by NT-MDT™. This instrument features high modularity and flexibility, being capable of measurements with diverse techniques (AFM, STM, shear force microscopy, scanning thermal microscopy...) simply by switching some of its separable parts. In this work, both its AFM and

STM capabilities are exploited. As an SPM, the Ntegra is capable both of atomic resolution and large-area scans (up to 90 µm × 90 µm × 9 µm), by means of switching its stage scanners. As most scanning probe microscopes, the scanner parts of this machine are based on piezoelectric ceramic tubes. An overview of this instrument is shown in figure 2.5.

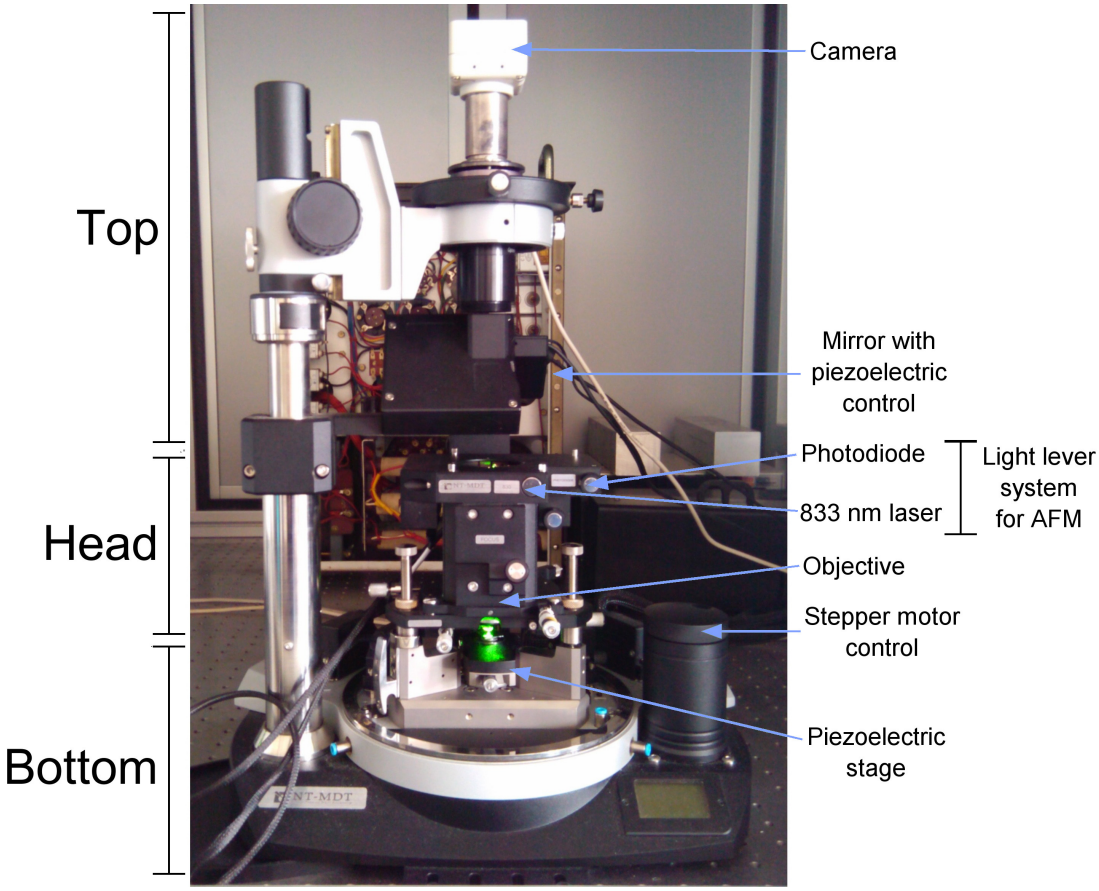

Figure 2.5: Picture of the Ntegra scanning probe microscope described in this work with annotations on the most relevant parts of the instrument. The picture was taken during a TERS experiment, as can be seen by the green laser shining above the sample stage.

In the Ntegra, during measurement the scanner moves the sample, placed under the probe, in a raster pattern while the tip and the optics stay put. The SPM is composed of three main volumes (excluding the separate electronics module). The top is where the camera, its optical condenser and the piezoelectric elements in control of a specific mirror for TERS measurements (more on that is reported in

section 2.4) reside. The bottom contains the sample stage and a vertical stepper motor for coarse approach. The middle part, the removable head, is the location of the excitation and collection objective (a long working distance *Mitutoyo M Plan Apo 100*, magnification 100× with a numerical aperture of 0.7, working distance of 6 mm and focal distance of 2 mm), and it also contains the replaceable pieces and probe holders for different SPM techniques, and the light lever system for AFM. This system transduces the deflection of the cantilever into an electrical quantity, and it is made up of a 833 nm laser diode focussed on the probe cantilever, by which it is reflected on a four-quadrant photodiode measuring its shifts with respect to the centre. The centre of the photodiode is a position of the laser reflection which corresponds to a constant, preset deflection of the cantilever, hence force on the tip, used as a reference for the measurement of tip force variations during scans. The optical path of the laser diode is long, to amplify the small shifts in the angle of the probe resulting in a relatively ample movement of the laser spot on the measuring photodiode: a light lever can improve the detection of cantilever displacement by a factor 1000. Unfortunately, the presence of this light source can be a cause of background in specific spectral regions of TERS spectra. In STM, the laser diode is turned off, and a source of voltage between the probe and the sample is active instead (ranging from −10 V to +10 V), and it is coupled to a nanoamperometer which measures the small tunnelling currents that occur (the full scale of the Ntegra ranges between −50 nA and +50 nA).

In scanning probe microscopy, a measurement of the interaction between the tip and the sample surface is continuously made. In *constant feedback mode*, this signal is compared to the *setpoint*, a previously set, target value to be reached by the interaction signal. The difference between the signal and the setpoint, the *error signal*, is used by the *PID* (proportional-integral-derivative) controller, where a *feedback* signal is generated to move the sample closer or further with respect to the tip, in order to reach the setpoint and reduce the error signal to zero. If the system is stable, this feedback process ideally keeps the distance between tip and surface constant. The output of an SPM measurement operated in this mode is the changes in height of the scanner which are registered in a 2-dimensional matrix (a map) as point values, from which the topography of the surface can be reconstructed. In *constant height mode*, the signal is measured but not compared to a setpoint, while the scanner does not elongate and stays invariant in height, registering the variations in the signals as the separation between probe and sample changes. Constant height mode is more sensitive with respect to constant feedback, but its output is the local changes in the measurement of the tip-sample interaction signal along the surface, and not directly lengths. Because of this, and since the tip-sample separation distance is a critical factor for the intensity of TERS spectral measurements, constant height mode was not relevant to this thesis, and constant feedback mode was always used in this work.

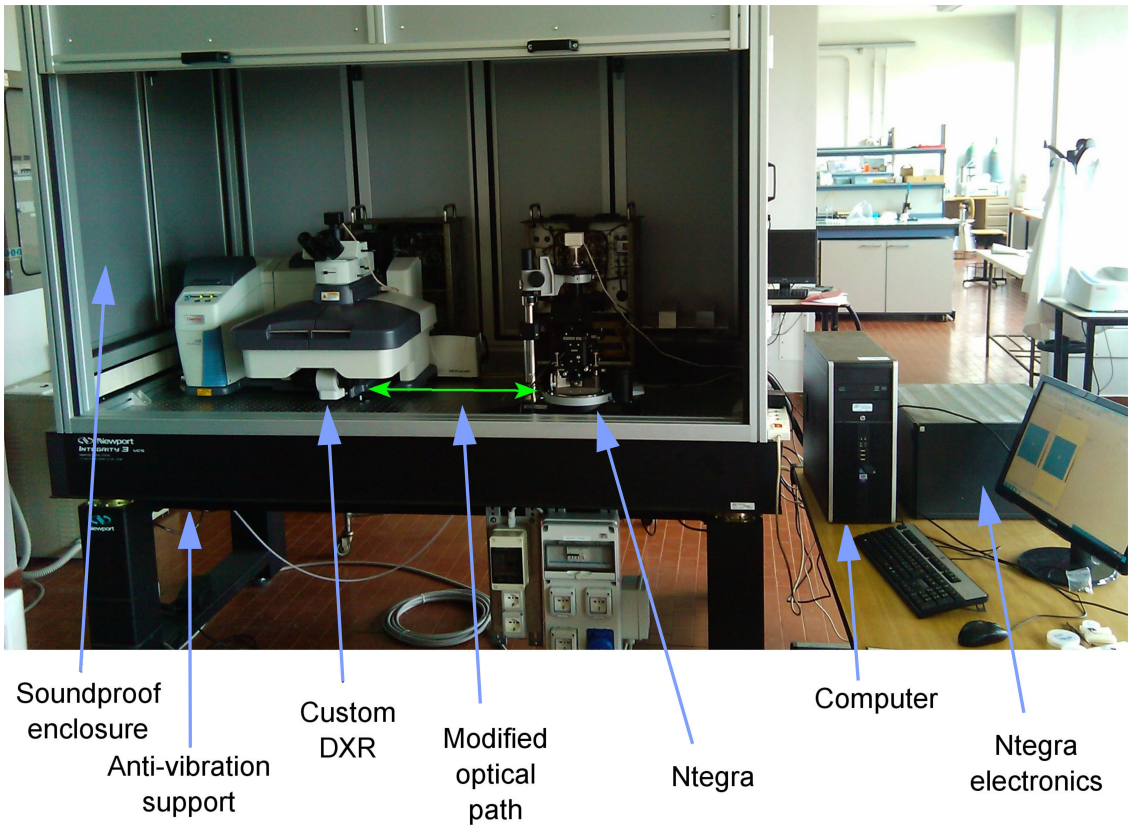

Figure 2.6: Photo of the coupled TERS setup with indications on the main parts. The green arrow illustrates the optical path in air between the spectrometer and the scanning probe microscope.

2.4 Specific measures for TERS

Figure 2.6 shows a picture of the assembled TERS setup in use in this thesis. Both the DXR™ Raman Microscope and the Ntegra were modified to work together in this setup, and coupled in a soundproof enclosure which also insulated the system from external light. This apparatus operates in ambient conditions. The whole system is fixed on a passive air-damped anti-vibration table, *Integrity 3* by Newport. The optical path of the DXR™ Raman Microscope is extended with respect to its standard path, by removing the objective and sample stage and by creating a hole in the chamber walls aligned to the SPM. The CCD is also cooled at −60 °C by a Peltier cooler to boost sensitivity by minimising noise, and the depolarisation filter is removed in order to maintain the native linear laser polarisation. The junction between the Raman spectrometer and the SPM is fiberless, therefore not subject to significant thermal fluctuations. The Ntegra itself is perforated and equipped with mirrors to bring the optical path to its top, where a piezoelectric element

similar to those on which the sample stages are based moves a mirror. This is a fundamental part of the TERS system, since it allows fine and on-the-run alignment of the Raman laser to the tip apex, and raster scans of the light spot on the sample for confocal Raman maps and hotspot searches before actual TERS mapping, as shown in figure 2.7.

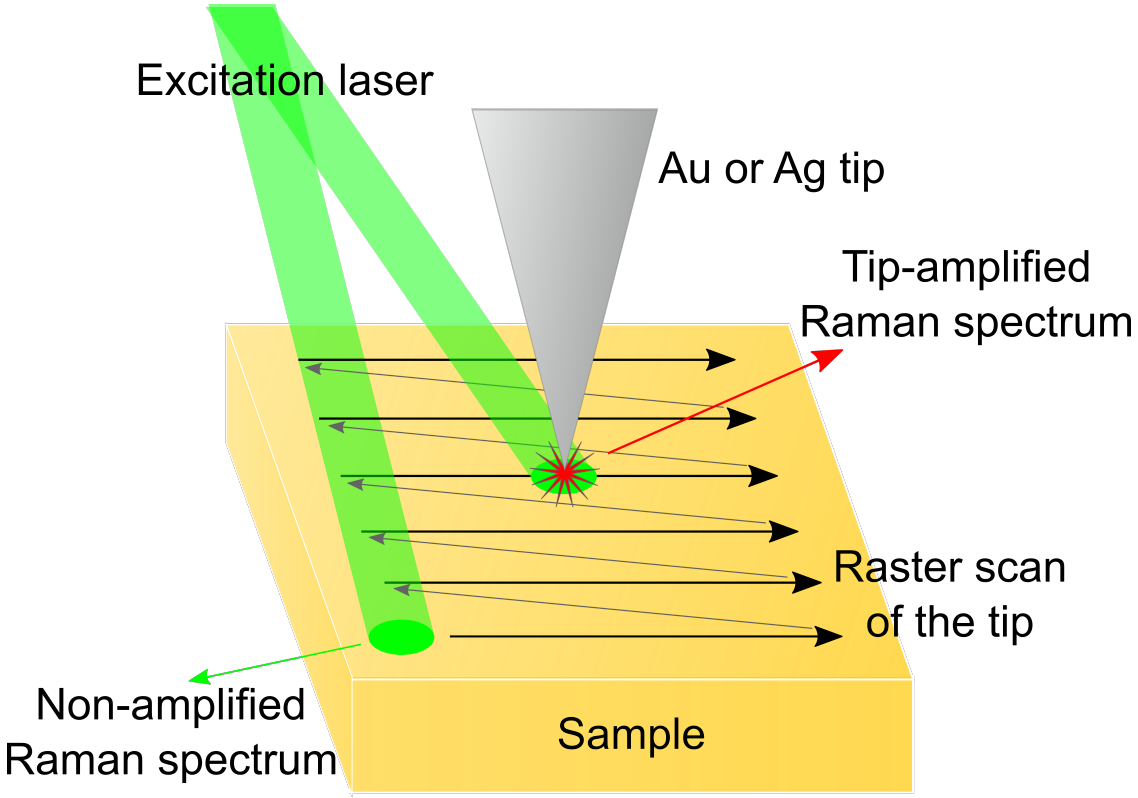

Figure 2.7: Schematic depiction of TERS apparatus operation. The excitation laser can be freely moved on the surface thanks to the piezoelectric tube which commands a mirror: this is useful both to employ the instrument as a Raman mapping system (with the probe removed), and to search for the hotspot while the tip is approached to the sample. After the hotspot is found, the laser spot can stay fixed while the tip-laser ensemble raster scans the surface (in the apparatus employed in this thesis the sample is moved by another piezoelectric tube stage, while the tip and the laser spot stay still).

The optical path passes through the long working distance 100× objective which focusses the laser on the sample stage, where it is reflected and scattered. The backscattered radiation is gathered by the same objective and travels along the same optical path, brought into the spectrometer, where it passes through the edge

filter, and then on the reflective diffraction grating monochromator, and eventually shines on the CCD. While the excitation laser of a standard DXR™ Raman Microscope suffers little losses along its optical path, the modified path described above causes a loss of about 50% of the illumination power at the SPM stage holder. The excitation power values declared in this work do not correspond to the nominal values measured at the source, but to the actual value measured with a THORLABS™ *PM100D* power meter instead.

Chapter 3

Calibration

The reliable measurement of quantities has been a cornerstone for such diverse fields as science and engineering and trade and commerce, dating back to millennia ago. *Metrology*, as the science concerning this, involves not only the act of comparing a physical quantity with a known unit of measurement, but also the equally important realisation, establishment, and dissemination of common standards (or *etalons*) among communicating parties. As of today, this is carried out in the scientific community by the worldwide adoption of the International System of Units (SI), whose creation started after the French Revolution, in 1799, with the adoption of the decimal metric system and artifacts for the metre and the kilogram. An internationally maintained organisation, the *Bureau International des Poids et Mesures*, International Bureau of Weights and Measures (BIPM) was successively instituted with the task of maintaining said standards, and later its scope and responsabilities were extended to other fields of measurement science than the appraisal of weight and length, leading to proposals of adding other units to the international system, which eventually became the SI we know today. Because of the unimaginable advances of contemporary science and technology from the point of view of the adopters of the first artefacts for the units of measurement, and the ever-growing precision of scientific instrumentation assessing the instability of such a method for the definition of units, as of today the BIPM does not hold actual artefacts as standards anymore, but instead adopts a new principle for the realisation of physically invariant quantities as the seven units of the new SI, starting from seven fundamental constants and as many definitions and deriving the units from experiments with specific requisites. The BIPM advises the use of at least one such process, called *mise en pratique* (practical realisation), for each unit of measurement. This is the foundation of modern metrology.

Metrology is the science of measurement, defined by the BIPM in one of its official documents, the VIM – International Vocabulary of Metrology, as:

> Science of measurement and its application.

> [...]
>
> Metrology includes all theoretical and practical aspects of measurement, whatever the measurement uncertainty and field of application. [39]

A key concept of modern metrology is the *metrological traceability* of measurements:

> Property of a measurement result whereby the result can be related to a reference through a documented unbroken chain of calibrations, each contributing to the measurement uncertainty.
>
> [...]
>
> A "reference" can be a definition of a measurement unit through its practical realization, or a measurement procedure including the measurement unit for a non-ordinal quantity, or a measurement standard. [39]

where the (metrological) traceability chain is:

> [A] sequence of measurement standards and calibrations that is used to relate a measurement result to a reference. [39]

Measurement uncertainty is central to modern metrology, defined as:

> Non-negative parameter characterizing the dispersion of the quantity values being attributed to a measurand, based on the information used.
>
> [...]
>
> Measurement uncertainty includes components arising from systematic effects, such as components associated with corrections and the assigned quantity values of measurement standards, as well as the definitional uncertainty. Sometimes estimated systematic effects are not corrected for but, instead, associated measurement uncertainty components are incorporated. [39]

Assessment of the uncertainty of a measurement is an integral part of the measurement itself, since no measurement is exact.

The practical realisation of metrological traceability is carried out through the process of calibration, which is:

> [The] operation that, under specified conditions, in a first step, establishes a relation between the quantity values with measurement uncertainties provided by measurement standards and corresponding indications with associated measurement uncertainties and, in a second step, uses this information to establish a relation for obtaining a measurement result from an indication.

> [...]
>
> Calibration should not be confused with adjustment of a measuring system, often mistakenly called "self-calibration", nor with verification of calibration. [39]

With the establishment and employment of these concepts, and by following the metrological traceability chain to the practical realisations of the SI units, *metrological comparability* between measurement results is possible, by tracing and comparing them to common standards worldwide, encompassing biases and errors, since these are comprised into the measurement uncertainty and evaluated during calibration. "Measurement standard established using a primary reference measurement procedure, or created as an artefact, chosen by convention" [39] are named *primary measurement standards*, while standards achieved through calibration with respect to primary standards are *secondary measurement standards*.

The following sections of this thesis are dedicated to the calibration of the TERS apparatus employed in this work. [39–41]

3.1 Spectral calibration

Wavelength calibration. Widespread methods for the wavelength calibration of Raman spectrometers are the analysis of Raman spectra of reference materials, such as monocrystalline silicon, polystyrene or cyclohexane, and the employment of spectral lamps, such as neon glow lamps, for the measurement of their emission spectra. Though the calibration process with the latter method is more laborious and requires additional instruments covering the spectral range of the spectrometer, low-pressure gas discharge lamps have the major advantage of having definite, well-established emission lines and metrological traceability to the International System of Units. Criticalities of this calibration method are the proper alignment of the lamp to the optical path, and the need for knowledge of exact wavelength of the emission of the Raman excitation laser. While the issue is negligible for helium-neon, argon, krypton and other gas lasers because of their precise, well-known and narrow emission lines, this can prove problematic for other types of lasers, such as solid-state and especially wavelength-tunable lasers and laser diodes: when utilising these emitters, it may be more convenient to resort to reference materials calibrations via direct Raman shift measurement, if a method for the precise assessment of their frequency is unavailable.

In this thesis, a 633 nm helium-neon laser was employed, and the DXR™ Raman Microscope spectrometer was calibrated by using a low-pressure neon glow lamp, in the spectral range between 50 cm^{-1} and 3500 cm^{-1}. The neon lamp is a convenient tool for calibration in these conditions because of its many strong and narrow

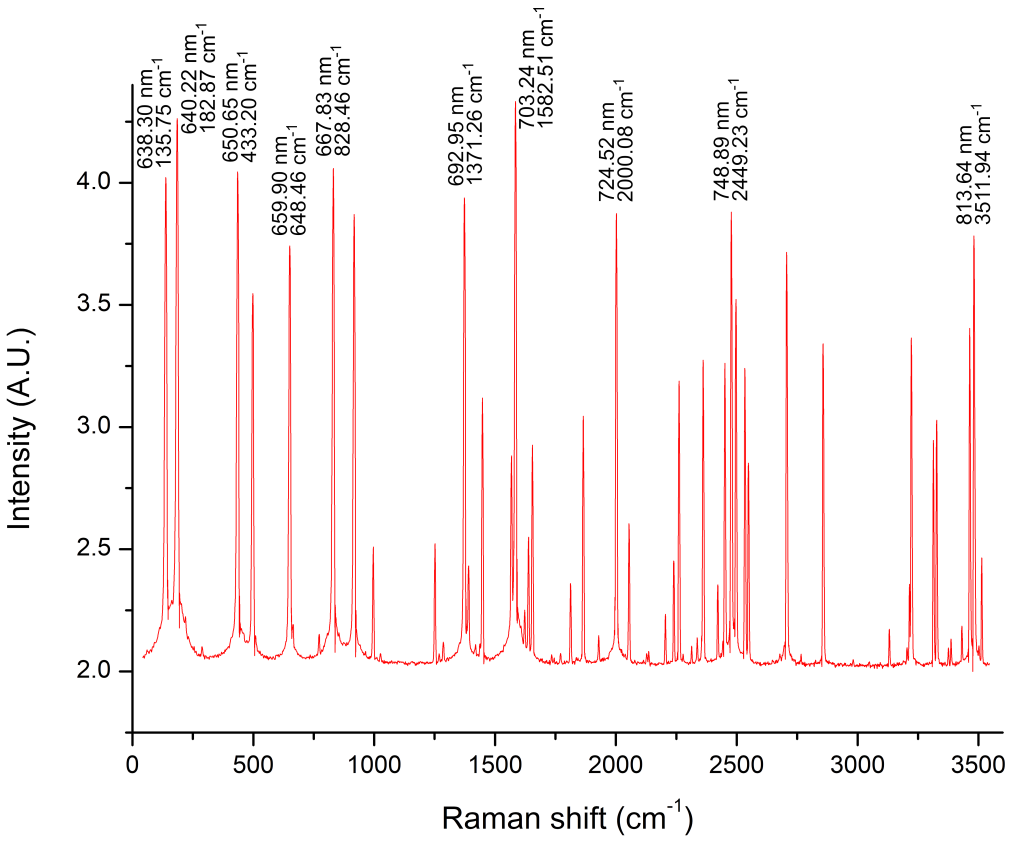

Figure 3.1: Neon glow lamp spectrum acquired with the spectrometer employed in this thesis, as used for calibration. The monochromator is set for the 633 nm laser, with the 600 lines/mm diffraction grating (50 cm^{-1} – 3500 cm^{-1} range). Some lines are assigned to tabulated values to be utilised as reference for adjustments.

emission lines, well distributed throughout the spectral region of interest. The calibration procedure was carried out as follows. A measurement of the neon emission spectrum was taken with a low magnification objective (10×) and the lamp surface was brought into focus. Then, a spectrum was acquired with the desired monochromator configuration, with particular care in setting the acquisition parameters in order not to saturate the CCD while having high signal to noise ratio. The resulting data (a sample spectrum is shown in figure 3.1) was then compared with tabulated neon lines: a set of strong lines spread out on the whole monochromator spectral range was chosen, and each peak wavenumber position was compared to the pixel on which the centre of the measured line fell, then adjustments were made to change those pixel values to the tabulated data. Given the very low spectral width of the gas emission lines, no regression was necessary to determine the pixel positions of the maxima. The values of the remaining pixels were then determined by interpolation. For example, for the calibration of the

632.8 nm laser (absolute wavenumber: 15802.41 cm^{-1}), the apex of the 703.24 nm neon line (absolute wavenumber: 14219.90 cm^{-1}) in the measurement shown in figure 3.1 fell on pixel #610. The Raman shift value assigned to that pixel was thus: 15802.41 cm^{-1} − 4219.90 cm^{-1} = 1582.51 cm^{-1}.

Intensity calibration. Traditionally, dispersive Raman systems with laser excitation sources were not subject to instrumental intensity response corrections. Nevertheless, accurate intensity calibration of the Raman spectrometer throughout its spectral range is imperative for several current widespread applications of Raman (e.g. carbon-based materials analysis), and it was a crucial point in the scope of this thesis as well, as can be appreciated in section 6.1 and subsequent. An intensity calibration method for Raman spectrometers should be based upon broadband light sources of known spectral irradiance. An established procedure to do this is the measurement of the output of a white-light calibration lamp, which can be calibrated relatively to a traceable irradiance source, and the use of these data to apply the proper corrections during or after Raman acquisition. Unfortunately, this approach can present several practical issues. Incandescent lamps, even tungsten-halogen ones, have declining performance in time, and should frequently be recalibrated in order to be effective standards; furthermore, they are not spatially uniform in irradiance, and exhibit polarisation effects. Practical issues of sample placement and focus may also render this method quite impractical.

The National Institute of Standards and Technology (NIST) and the American Society for Testing and Materials (ASTM) subcommittee on Raman Spectroscopy (E13.08) developed another kind of procedure, applicable to Raman and fluorescence spectroscopy, requiring a Standard Reference Material® (SRM®) consisting in a fluorescent glass which, when irradiated with a specific wavelength (engineered to correspond to a typical Raman excitation laser frequency), luminesces with a known, predictable intensity response over a wide spectral range. These standards were found to yield a spectral response estimated as a fifth-order polynomial, in the following shape:

$$\begin{aligned} I_{SRM}(\Delta\nu) = A_0 + A_1 \times (\Delta\nu) + A_2 \times (\Delta\nu)^2 \\ + A_3 \times (\Delta\nu)^3 + A_4 \times (\Delta\nu)^4 + A_5 \times (\Delta\nu)^5 \end{aligned} \tag{3.1}$$

where $I_{SRM}(\Delta\nu)$ is the intensity as a function of Raman shift $\Delta\nu$ and the A_n ($n = 1...5$) are the experimentally-evaluated coefficients. Uncertainties (defined as 95% confidence intervals) range from 2% to 4% for most relative shifts intervals.

The practical realisation of the intensity correction was carried out in this thesis as follows. Firstly, an intensity measurement on the SRM® ($S_{SRM}(\Delta\nu)$) was made, followed by the acquisition of the Raman spectra to be corrected ($S_{MEAS}(\Delta\nu)$) with the same data spacing as the reference material profile. The reference intensity profile was then calculated using each abscissa point in $S_{SRM}(\Delta\nu)$ and $S_{MEAS}(\Delta\nu)$ by

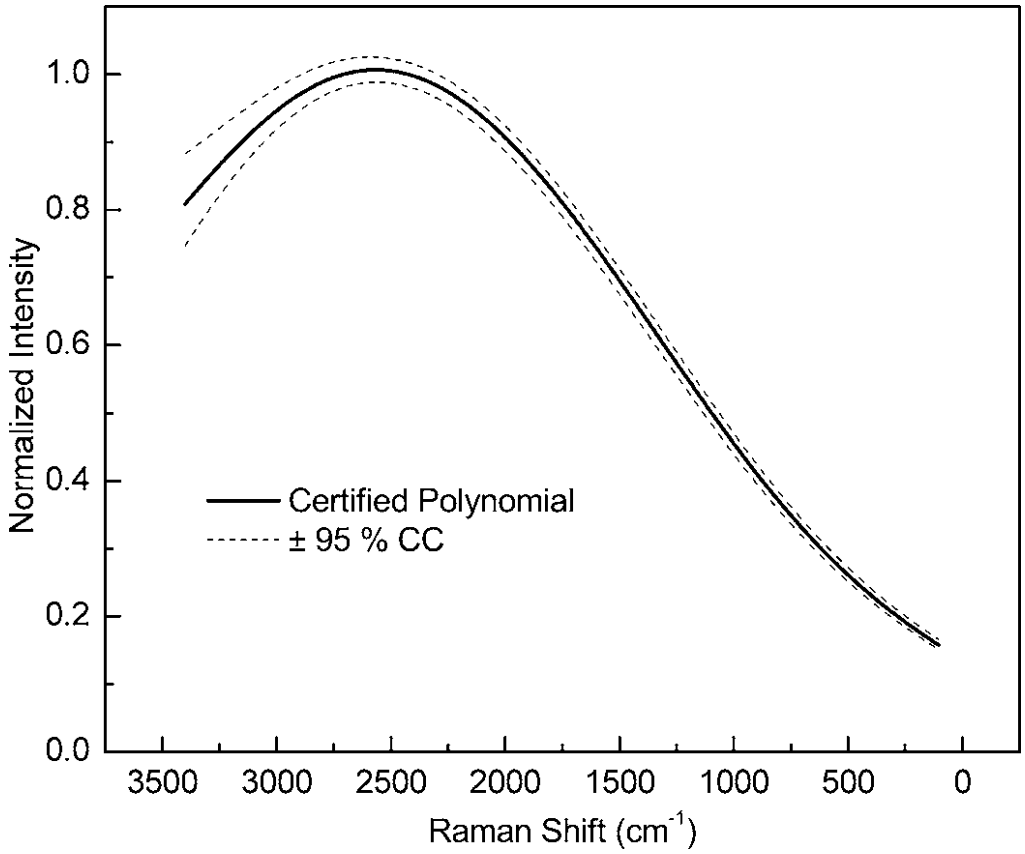

Figure 3.2: Calculated intensity response (solid line) of the fluorescent glass standard for intensity spectral calibration (SRM® 2241), a polynomial of the fifth order. The dashed curves indicate the 95% confidence limits. [42]

employing equation 3.1 (the profile will be referred to as $I_{SRM}(\Delta\nu)$). A correction curve could then be calculated as:

$$C_{SRM}(\Delta\nu) = \frac{I_{SRM}(\Delta\nu)}{S_{SRM}(\Delta\nu)} \tag{3.2}$$

With this curve, the corrected Raman spectra $S_{CORR}(\Delta\nu)$ could thus be obtained:

$$S_{CORR}(\Delta\nu) = C_{SRM}(\Delta\nu) \times S_{MEAS}(\Delta\nu) \tag{3.3}$$

Note that both the shape and the intensity profile of the SRM is highly sensitive to temperature, and it is certified be employed in the 20 °C – 25 °C range. [42, 43]

3.2 Spatial calibration

SPM measurements can be traceable to the International System of Units, specifically to the definition of the metre. In order to do so, the unbroken chain of comparisons from the *mise en pratique* to the actual measurement with estimated uncertainties dictated by the BIPM starts from the practical realisation of the metre, fixed in terms of the second and the speed of light. Therefore, in combination with a time standard, this can be achieved in two ways. A direct measurement of light travelling time can be conducted, with a time of flight measurement of electromagnetic wave well-defined packets (such as laser pulses). This procedure is mainly employed in long distance assessments (i.e. above 1 km, e.g. Earth-Moon separation measurements), since its precision is mainly limited by uncertainties generated by delays due to electronics. The other widespread approach is conducted with optical interferometry: this is the most accurate method and most suitable for sub-metre realisations. The procedure is based on the shifts of intensity (phase) of coherent, monochromatic light subject to self-interference after propagating along a measurement pathway and a reference one. Accurate knowledge of the frequency of the employed light source is paramount, along with other parameters such as the refractive index of air (therefore pressure, humidity, temperature, composition), and this is achieved by employing a femtosecond frequency comb, linking the metre and the second. An interferometric approach may be employed for the realisation of a so-called "metrological SPM", in which the movement of the sample with respect to the tip is constantly monitored with a measurement independent from the stage control, carried out by one or more interferometers for one-, two-, or three-dimensional motion tracking. This is the best approach for metrological traceability since it incorporates a primary calibration method, and automatically eliminates scanner errors without software corrections or modelling, but it requires heavy investments in equipment and setup, hence reducing its practicality in most environments. Another practice is the substitution approach, in which the SPM to be calibrated is subject to assessment of its metrological properties in order to make it possible to extract the actual position and calculate its uncertainty for any position of the scanner. A third option, the most widely employed, is the comparison method: alongside the target surfaces to be analysed, a calibrated secondary standard is measured, made of a stable material (e.g. silicon or silicon oxide for AFM, or metal for STM) and presenting repeating features of different height, generally in the form of raised or lowered one-dimensional gratings or two-dimensional squares. An example of an AFM measurement of such a calibration sample is shown in figure 3.3.

In this work, the comparison method was employed. This approach, although quite convenient for its celerity, portability and ease of use, might require several samples if different scales are involved, and extensive care has to be taken to avoid common SPM artefacts both in the calibration step and the actual measurement

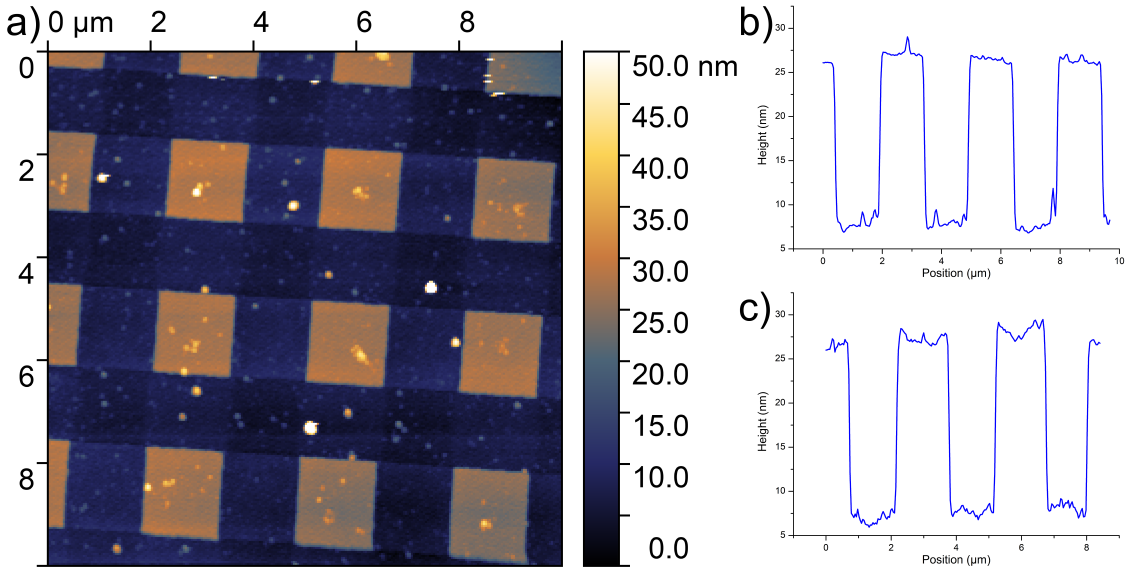

Figure 3.3: SPM measurement of a typical silicon oxide calibration grating, consisting in a flat surface with an array of raised squares. a) image of the surface. b) average horizontal profile of several horizontal lines. c) average horizontal profile of several vertical lines.

itself. The procedure consists in scale calibration and identification of linearity and orthogonality deviations, common artefacts with piezoelectric scanners. Furthermore, in vertical measurements (defining "vertical" the direction of the distance between probe and sample plane), the discrepancies in distance as a function of SPM feedback signal (e.g. van der Waals forces, conductivity) along the surface and humidity can be source of uncertainty. Moreover, after horizontal calibration (along the plane orthogonal to the vertical direction), it may be needed to take into account tip convolution, a major source of error in SPM. To avoid tip convolution issues, a simple scaling and orthogonality correction method is to measure the separation length between equivalent edges of the calibration sample (e.g. the average distance between rising edges in a grating) in two horizontal perpendicular directions while measuring plateau height for vertical scaling: this is the method that was employed in this thesis; for one-dimensional samples, the measurement is repeated with the specimen rotated by 90°. The standard employed in this work is model TGQ1 by NT-MDT™ and the Ntegra is calibrated by AFM. [39–50]

Part III

Results

Chapter 4

Probe preparation for TERS

Scanning probe microscopy was conceived years before TERS, and thus now it is much more widespread, being routinely employed in surface analysis and nanotechnology. Several methods for the production of probes exist for this family of techniques, and, in general, these depend on the specifics of the feedback employed in the measurement: many SPM declinations require specially prepared tips of difficult preparation demanding industrial production, leading to batch preparations which could hardly be modified or personalised. For instance, AFM tips are usually made of monocrystalline silicon, silicon oxide or silicon nitride, manufactured with top-down processes involving several steps of photolithography, mask-aided wet etching and anisotropic silicon etching, leaving little room for recipe variations which would be essential for enhanced Raman spectroscopy. Since only recently TERS became popular enough to spark commercialisation of specialised probes for it, commercial TERS tips are marketed by few, are quite expensive, mostly have low yield, and are not optimised for each experimental apparatus, given the variety of excitation wavelengths, materials, and existing geometries. Furthermore, most tips have a limited lifetime even in storage conditions, rendering impracticable to ship them: for example, silver probes are best employed within 48 hours from production [51, 52], becoming almost completely inactive after this time. Consequently, the optimal solution for laboratories is generally either to fabricate their own tips, or to adapt existing probes for TERS themselves. Given the differences in feedback types between the most widespread techniques for TERS, AFM and STM, the probe preparation processes for TERS are radically different depending on the underlying SPM approach [48–50].

4.1 AFM tips

AFM requires probes with quite strict specifications in order for them to function properly with the light lever system. Their geometries consist of a sharp tip whose shaft height is in the order of the micrometres, and comes as perpendicular as possible to the sample surface. The tip shaft is attached to or near the end of a flexible cantilever, which is a wide, thin strip of hard, elastic material, with resonance frequency and force constant optimised for a specific AFM mode: for contact mode, a long cantilever with low resonance frequency and low force constant is typical, while a high resonance frequency and high force constant resulting from a short cantilever is the better choice for semi-contact mode, since the probe is conceived to vibrate with frequencies which are usually in the order of the hundreds of kHz. In order to transpose these properties to TERS-active probes with gold or silver apices, generally commercial AFM probes are coated with these noble metals, in a bottom-up approach.

This practice can lead to several issues for the goal of manufacturing greatly enhancing tips with high yield, especially if high reproducibility and stability are sought as well. Several viable metal deposition techniques exist, leading to radically different results; the parameters, which can be chosen with a degree of arbitrariness, also influence the quality of the film. There are even contrasting opinions in literature on which properties should such deposition have for the best enhancement results [29, 53, 54]. Nevertheless, the most important parameter for high efficiency probes is the metal layer thickness. Indeed, this attribute dictates the plasmonic resonance profile of the tip, hence the LFIEF and the enhancement factor at each specific excitation wavelength: coating a probe increases the radius of its apex, which grows as more material is accumulated on it. Because the enhancement spurs from the apex itself, like a SERS nanoparticle, the control of its dimensions is crucial to maximise the performance of the system. Since, as in this thesis, it is commonplace to mount non-tunable excitation lasers on TERS implementations, the deposition thickness is varied instead for optimal plasmonic tuning with the excitation frequency. Sometimes other parameters are varied as well for this purpose, such as the thickness of optional dielectric layers covering the metal or placed between the metal and the base probe (shifting the peak plasmon resonance frequency), or the geometry of the metal layer itself. It should be noted that this approach increases the apex size, resulting in a less performing tip, in terms of spatial resolution, with respect to a standard AFM probe: while most pristine AFM probes have apices of diameters smaller than 10 nm, TERS tips apices are required to have diameters roughly between 10 nm and 100 nm to resonate in the visible range, as the theory of electromagnetic SERS enhancement dictates.

In this thesis, AFM-TERS was performed with gold-coated probes and a 633 nm excitation laser after the development and the optimisation of a tip preparation process. Generally, gold yields lower enhancement probes with respect to silver,

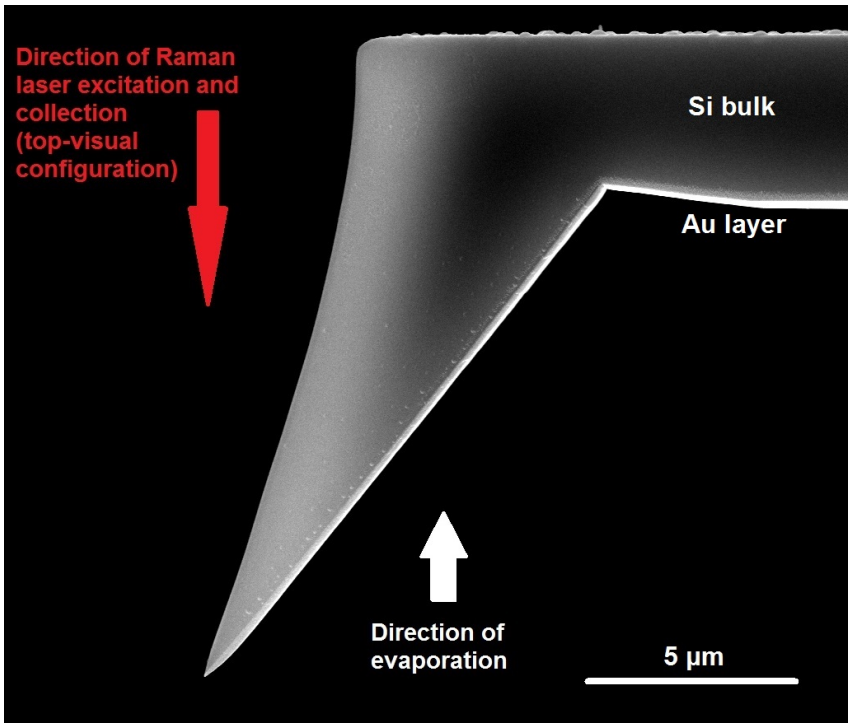

Figure 4.1: Scanning electron microscope image of the tip shaft of an AFM sputtered corner tip, with indications about the direction of the optical path and the sputtering. The end of the cantilever is visible on the right.

but is much more stable in time, as silver tips, while stored and utilised in ambient conditions, are subject to considerable oxidation and sulfuration processes: since AFM-TERS tips are usually fabricated in batches, gold tips are more convenient. Monocrystalline top-visual silicon probes (*VIT_P_C-A* by NT-MDT™, with apex curvature radius <10 nm, tip shaft height 15 µm, cantilever dimensions 450 µm × 50 µm × 2.5 µm, nominal force constant 0.8 N/m, nominal resonant frequency 16 kHz) optimised for contact mode were used as a base, and were coated with a thin gold (99.999% by Alfa Aesar) layer for plasmonic enhancement. Unfortunately, this combination of materials by themselves yielded metal films which were not stable in time, and were not very mechanically resistant as well. For the purpose of durable TERS probes which are to come in contact with hard surfaces and scan them, this is not ideal.

To solve these issues, a thin adhesion layer was employed between the silicon and the gold, with which the commercial probes were coated as a first step in the production process: titanium was chosen as the material for the adhesion layer. Controlling the thickness of the titanium was as crucial as attaining the reproducibility of the gold layer itself: adhesion layers are known to reduce the efficiency of the plasmonic Raman enhancement, with thicker films generating tips

with lower enhancement factors [55–58]. For the deposition of both the titanium and the gold layers, sputtering was employed. In this thesis, the process for the production of the probes just described was devised and optimised.

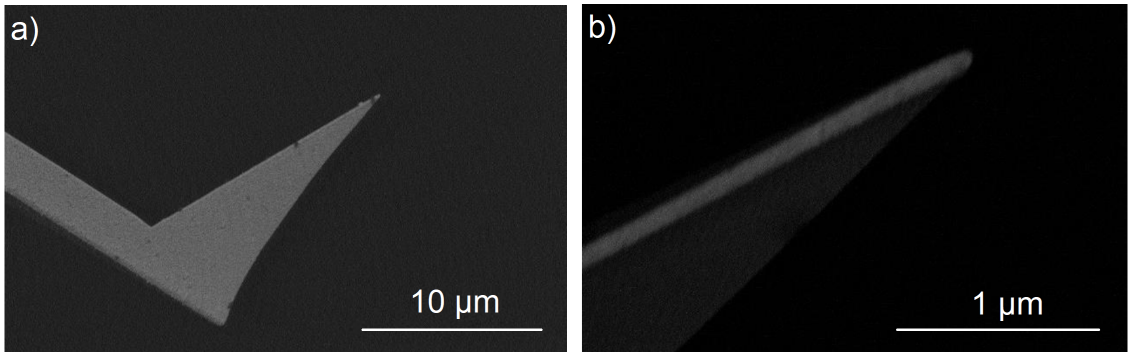

Figure 4.2: Scanning electron microscope images of an AFM corner tip after the optimised gold film sputtering deposition with the 5 nm titanium adhesion layer (not visible). Both images were taken with a backscattered electron detector, revealing elastic electron scattering, hence differences in the atomic composition in the images, since heavier elements (gold) backscatter electrons more strongly than lighter elements (silicon), so they appear brighter. a): 7000× magnification side view of the sputtered tip. The probe shaft and part of the cantilever are visible. b): same perspective view at 80000× magnification with different contrast. In this picture, the gold film is easily distinguishable from the silicon base: the directional nature of this deposition technique can be noticed, as the layer is much more prominent on the top side of the silicon, which faced the sputtering target. The nominal thickness of the gold film, as measured by stylus profilometry on a silicon chip put adjacent to the probe during the sputtering process, is 90 nm, while a visual estimation of the actual film thickness on this tip is 60 nm.

The probe production procedure was the following: a batch of clean commercial silicon AFM tips were placed inside the chamber of the magnetron radio frequency sputter coater, optionally along with a partially covered sample cut from a flat monocrystalline silicon wafer. Since sputtering is an anisotropic process, the probes were oriented towards the gold plate, as shown in figure 4.1, at a distance of 10 cm from the target. High vacuum was then created in the chamber, to a pressure of 2×10^{-4} Pa. Argon gas was pumped into the chamber until it reached a pressure of 0.1 Pa, then current was applied (with a power of 100 W) to generate plasma, sequentially eroding a titanium target for 35 s in order to deposit a 5 nm layer, then switching to a gold target. In this work, every parameter was maintained constant throughout the study, while the gold sputtering duration was varied in order to

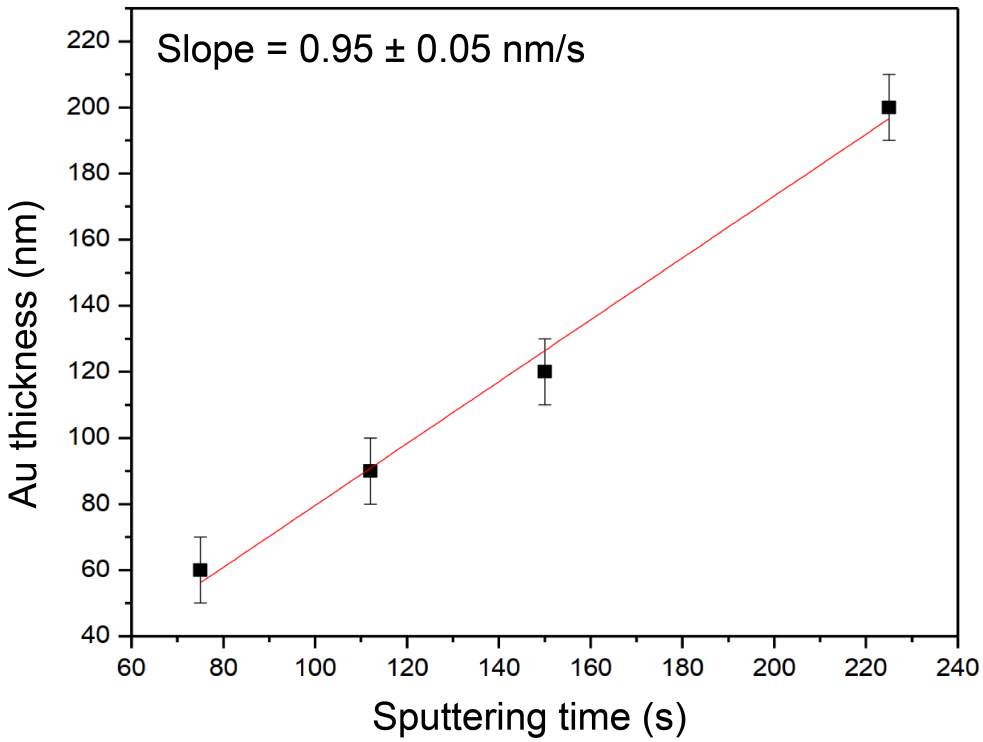

Figure 4.3: Calibration curve of nominal gold thickness by sputtering with the parameters employed in this work as a function of deposition time, assuming a linear progression. By linear regression, it can be inferred that, in the investigated range of 75 s to 250 s, the film growth speed was (0.95 ± 0.05) nm/s, corresponding to a thickness range of 60 nm to 200 nm.

create gold apices of different sizes, which were then measured to assess the best tuning with the 633 nm wavelength laser. Since sputtering is a directional process, the resulting gold layer was mainly present on the side of the probes adjacent to the metal targets. This could be easily seen with scanning electron microscope (SEM) imaging. In figure 4.2, SEM images of such probes are displayed.

After the deposition, the probes were ready to use, and removed from the sputtering chamber. For the measurement of the layer thickness just created, the flat silicon chip was uncovered, revealing a step between gold and silicon oxide which was proportional in height to the thickness of the gold layer deposited on the tip, but was much more easily measurable. This was employed to obtain a nominal value of film thickness to associate with the sputtering time, which was not the exact thickness of the gold film, nor it was correspondent to the diameter of the apex (the diameter of the nanoparticle to which the tip is ascribable). Layer thickness and sputtering time were found to be directly proportional, with a factor of (0.95 ± 0.05) nm/s, within the analysed range of 75 s to 250 s, yielding films

of thicknesses ranging from 60 nm to 200 nm. The calibration curve for this is shown in figure 4.3. The values and the uncertainties of the thicknesses of the plasmonic layers derive from 5 repeated measurements on different parts of the layer step on the silicon chips, performed with a *Talystep 1* stylus profilometer (by Taylor-Hobson).

The TERS results of the optimisation of the manufacturing procedure by analysing the enhanced Raman intensity of the probes as a function of nominal film thickness are presented in chapter 6.1, in which a novel approach for precise assessment of the Raman enhancement potential are introduced. This methodology was applied to this study to determine TERS intensities arising from the tips.

4.2 STM tips

Scanning tunnelling microscopy was employed in this thesis as well as AFM as a control signal for TERS. STM can be performed with probes with much less strict requirements than those necessary for AFM: the indispensable condition is the conductivity of the tip (as well as that of the substrate). Consequently, a simple approach can be undertaken for STM tip manufacturing: the most basic STM probe is a simple tip shaft of unrestricted shape and dimensions, which inevitably ends in a single atom protruding the most from it, with a macroscopic attached conductive volume for manipulation and electric contacts. Therefore, the majority of STM probes are fabricated in a top-down approach starting from a plain metal wire, which serves this purpose entirely, if provisions are taken to make it terminate in a nanometric cusp.

There are two main methods for the production of STM tips starting from a filament: the wire stripping method, and wet etching. The former is the most rapid, inexpensive and uncomplicated: an operator cuts the metal strand with a sharp blade, such as scissors, a razor or a scalpel, at a 45° angle with respect to the wire, while applying the appropriate amount of mechanical tension to the fiber. By doing so, the wire ruptures and frays ending in acuminate threads, usually pointed enough to be used as STM tips. While approaching this probe to the analyte surface, the outermost of these points will be the closest to the sample, generating most, if not the whole tunnelling current by itself, making it possible to ignore the rest of the threads. However, there are several issues with this approach, especially when considered with a view to fabricate TERS tips. The procedure is very operator-dependent, requiring expertise just to obtain a usable STM probe. Furthermore, the location of the outermost thread with respect to the shaft is uncontrollable, which most of the time renders the focussing of the Raman excitation laser on its apex impossible with a top visual TERS apparatus, since the shaft can obscure its

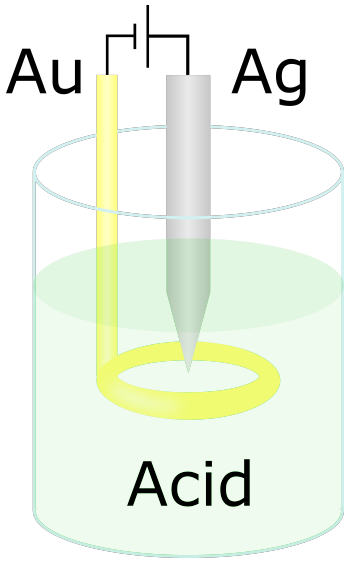

Figure 4.4: Diagram of the electrochemical cell employed for the production of silver STM-TERS tips in this thesis (electronic circuitry depicted as a direct voltage generator).

view by the objective. Moreover, the shape and dimensions of the nanoparticle at the extremity of the probe are out of control as well. Because of these reasons, this approach is inadequate for the manufacturing of STM-TERS tips.

A more suitable method for the fabrication of controllable, reproducible STM-TERS tips is wet etching, consisting in immersing the raw material in an appropriate etchant solution, which erodes it until a sharp apex is formed. This procedure has various advantages over mechanical stripping: the resulting probes have a conical shape with a defined geometry, aspect ratio, and apex radius, which are delineated by physical and chemical specifications such as etching solution composition, etching time, and apparatus layout and parameters, with virtually no operator dependence.

In this thesis, electrochemical etching was employed for the production of full silver tips. These probes were engineered to best resonate with a 633 nm excitation laser, and to have a high aspect ratio, in order to minimise shadow effects from the shaft, which can be an issue in the top-visual apparatus where they were to be employed, while still being robust enough to withstand van der Waals forces while interacting with the samples at typical STM working distances ($\sim$1 nm). The restriction on the material is an additional concern pertaining to TERS which is not present in conventional STM measurements, since for the latter technique there is no constraint in the choice of probe material except conductivity, thus allowing the election of employment of very hard metals and alloys, such as tungsten or platinum-iridium, unlike the soft gold and silver necessary for TERS.

Electrochemical etching consists in the etched material being one electrode in an electrochemical cell. Controlling the voltage allows different chemical reactions at the electrode surface with respect to unbiased etching, as well as changing the rate of erosion. The main factors to establish in this setup are the etching solution chemical composition and concentration, the shape of the electrodes, their reciprocal position and placement with respect to the solution surface, the electrode bias voltage, and the etching time. In figure 4.5, the etching diagram inside the cell during fabrication of a probe is illustrated. This technique utilises the meniscus that forms in the etching solution on the wire: the metal is corroded more quickly near and inside the meniscus, resulting in a uneven erosion leading to the cutoff of the immersed part of the metal strand, referred to as *drop-off*, and leaving behind a conical sharp tip. Its shaft often presents a "pagoda-like" structure caused by the movement of meniscus during the etching process, as can be seen in figure 4.6, which shows a SEM image of a STM-TERS silver tip manufactured with the described procedure.

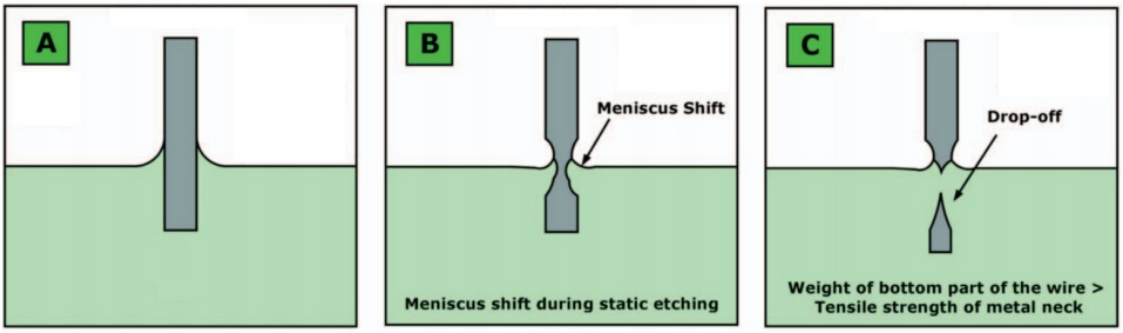

Figure 4.5: Scheme of the dynamics of electrochemical etching as described in this work. (a): before etching. The solution (green) forms a meniscus on the wire (grey). (b): during etching. The wire is partially eroded, while the meniscus changes its position, causing the conical shape to develop. (c): after drop-off. The lower part of the wire detaches, leaving a nanostructured tip. The apex itself is still submerged by the acid, hence the etching process continues, unless the voltage is stopped; even without voltage the apex is eroded, although at a much slower rate. [59]

The probes employed in this work were produced starting from a 250 µm cylindrical silver wire (99.99% purity silver, Sigma-Aldrich), employed as an anode in an electrochemical cell, straightened out and vertically dipped and suspended, partially immersed, in a solution consisting in a 1:2 volume ratio of perchloric acid (70% $HClO_4$ from Merck in water) and methanol (special grade, produced by Carlo Erba) respectively. The cathode was built from a pure gold wire of diameter 1 mm,

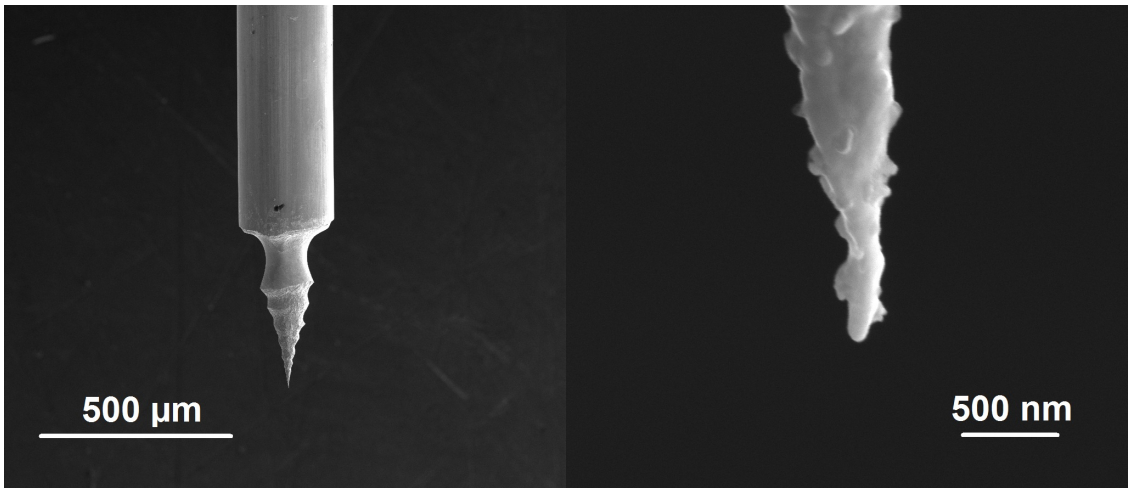

Figure 4.6: Scanning electron microscopy image of an optimised STM-TERS tip, shown as an example. In the lower magnification image (left), the uncorroded wire and the pagoda-like structure due to the solution meniscus shifting during etching can be seen. In the higher magnification image (right), the nanometric apex is visible, along with part of the shaft.

modelled in a ring shape centred on the anode and whose plane is orthogonal to the anode axis and parallel to the solution surface. The ring, of diameter 15 mm, was placed just below the surface of the etching solution.

In this system, when the cell is biased the silver on the surface of the anode reacts with the water, resulting in silver oxides and gaseous hydrogen, both of which could be seen in this setup to the naked eye in the form of loss of reflectivity of the metal and sporadic gas bubbles on the surface of the submersed wire respectively. The cell was contained in a cylindrical glass beaker with a height of 5 cm and a diameter of 3 cm. For each probe, 20 mL of fresh etchant solution were used. Continuous voltage was applied to the cell with an Amel *Mod. 2055* potentiostat to generate an initial current between the electrodes of 50 nA, monitored with a Keithley *2100* multimeter in series with the cell. After less than a minute, in a successful etching the wire near the solution surface was fully eroded, and the bottom part of the silver strand detached.

Preliminary tests on the system had shown that fine control of the voltage applied to the cell after the drop-off was of utmost importance to manufacture reproducible, efficient, plasmonically active probes with this process. Both SEM imaging and TERS activity checks showed a very high variability in the etching yield when the voltage was manually stopped after the drop-off. This can be explained by the protraction of the erosion process of the newly-formed apex, gradually but rapidly getting blunter as the electrochemical reactions continued (see figure 4.7). This process heavily influenced the ends of the resulting probes at the nanoscale,

often leading to uncontrollable, blunt tips when the voltage cut was variable in time scales bound to operator reflexes, considering that the median human reaction time is in the hundreds of milliseconds.

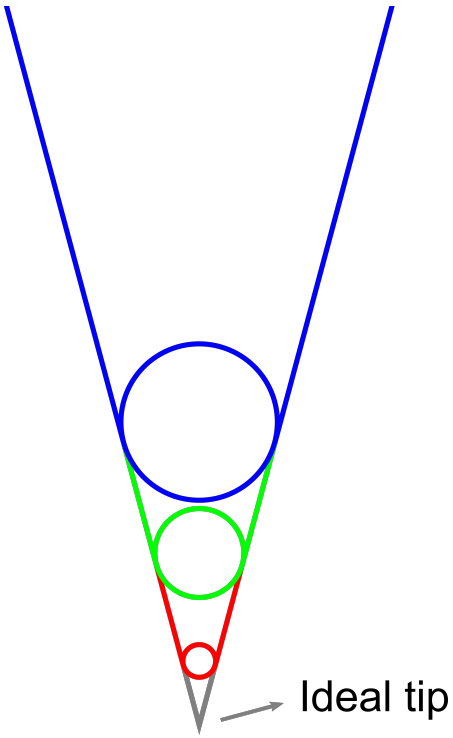

Figure 4.7: Diagram of apex radius changing with etching time after the drop-off. The apex radius increases with the etching time, therefore a process without electronic control on the voltage has very low reproducibility. Even after the voltage to the cell is cut, the blunting of the tip carries on, although much more slowly: the operator should remove each probe from the cell and rinse it within seconds from the drop-off, which is why the event was signalled in the apparatus built in this thesis by the change of state of the LED in the electronic control.

To solve these issues, a home-made electronic circuit was devised and implemented, which monitored the etching current and cut the voltage bias to the cell after drop-off, with a variable trigger condition for fine-tuning of the dimensions of the resulting probes. The schematic diagram of the circuit is displayed in figure 4.8, to which the nomenclature in the following explanation refers.

The electronics took advantage of a *BS170G* MOSFET transistor (Q1), in which the totality of the cell current flowed during the whole operation (the current passing in the path through capacitor C1 was negligible except at the very start and end

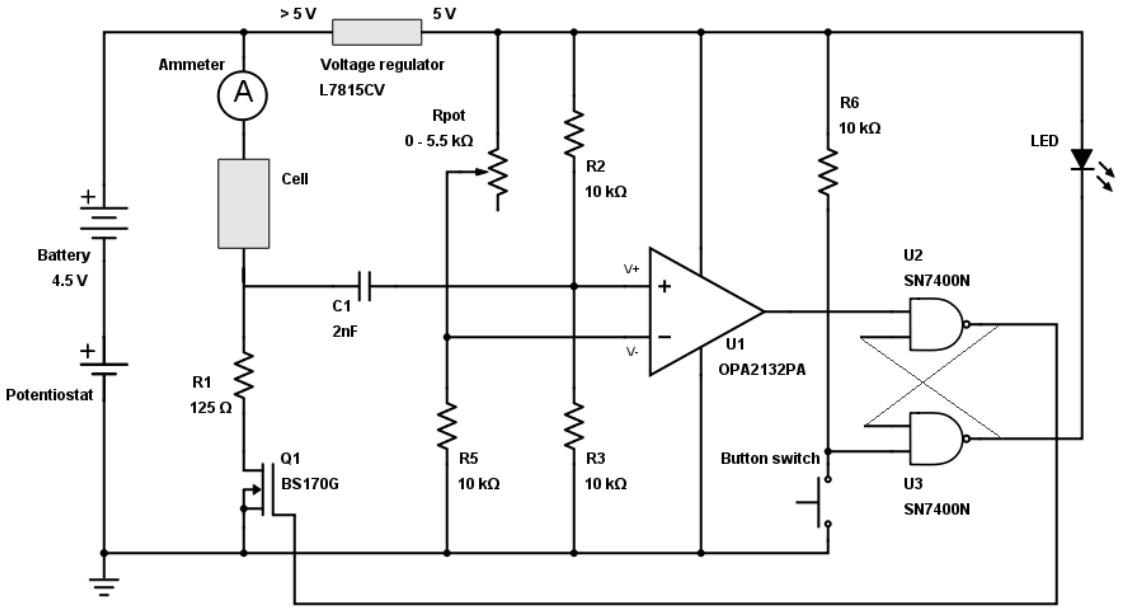

Figure 4.8: Schematic diagram of the electronic circuit devised and employed for controlled electrochemical etching of the STM-TERS silver tips employed in this work.

of the etching process), therefore the MOSFET was required to be able to conduct high current loads (>50 mA for the parameters employed in the procedure followed in this thesis). This transistor was employed as a switch to open, after drop-off, the circuit branch consisting in the ammeter A (the Keithley *2100* multimeter set up to a full scale of 100 mA, and not to change its scale automatically), the electrochemical cell, a resistor R1, and the aforementioned MOSFET. Note that this branch was equivalent to the circuit of the minimal working setup for manual voltage cut-off, with the additional implementation of the transistor. Because of the limitation in maximum output voltage of the potentiostat (5 V), a 4.5 V Duracell battery (with a measured output voltage of 4.6 V $\pm$ 0.1 V) was connected in series to the Amel potentiostat to provide up to 9.5 V. The operating procedure devised for the fabrication of these tips, as for the manual voltage shutdown described earlier, required to set the voltage in order to provide an initial etching current of 50 mA: in this particular configuration, the voltage required was found to be consistently 3.5 V (potentiostat) + 4.6 V (battery) = (8.1 $\pm$ 0.1) V total (measured with a multimeter for verification).

To control the MOSFET gate electrode, the control part of the circuit was biased by the same voltage source as the etching branch, but decoupled with a voltage regulator, which brought down the voltage to 5 V from the variable bias of

the cell. The two parts of the electronics were connected by C1, a capacitor which insulated it during operation, except for the end of the etching, where the voltage at the cell-R1-C1 node abruptly changed because of the wire drop-off, sending current into the capacitor, acting as a high-pass filter, and changing the voltage at the non-inverting V+ input of an operational amplifier U1, employed as a voltage comparator. V+ was otherwise kept at 2.5 V by a voltage divider consisting in equal resistors R2 and R3. The operational amplifier compared this voltage with its inverting input, biased and kept constant throughout the etching by a resistor R5 and a potentiometer Rpot acting as a variable resistor. Rpot regulated the variable trigger condition V−, the voltage to which the operational amplifier compared V+, dictating changes in the final etching result at the nanoscale. Figure 4.9 shows the output of the ammeter during the etching of a typical tip. Note that, in this graph, the time step interval is 30 ms, and the drop-off appears instantaneous as it is not temporally resolved within this time interval: indeed, it is reported that in this kind of etching the current falls within hundreds of nanoseconds [59], in this case from approximately 40 mA to 0 mA, enough to trigger the circuit shutdown.

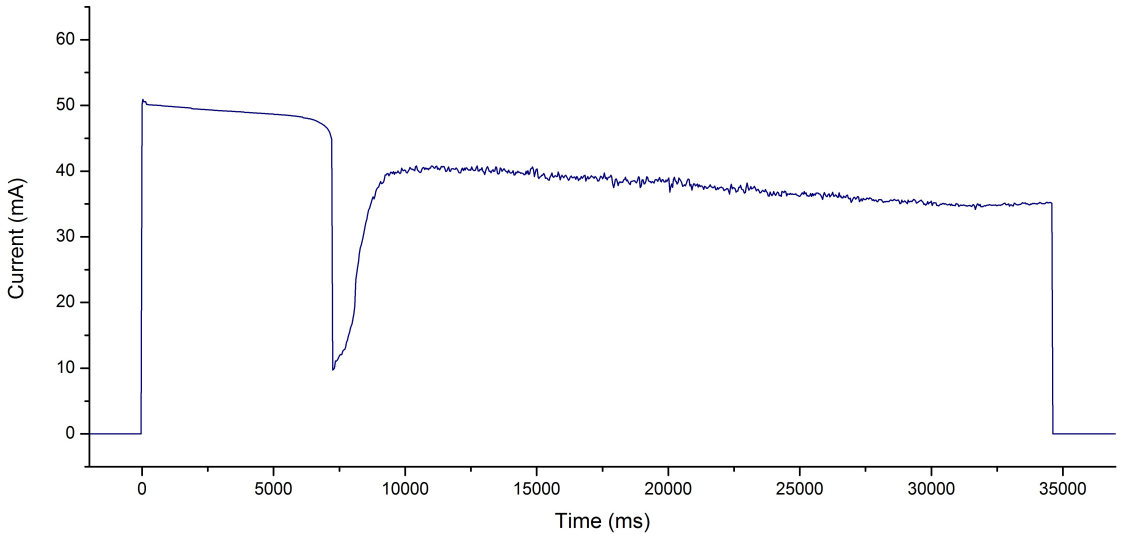

Figure 4.9: Graph of the current flowing through the cell during electronically-controlled etching, as measured by the ammeter installed as shown in figure 4.8. The process took less than a minute per tip. The resistance of the cell rose in time during etching as the surface of the wire decreased, until drop-off, when an abrupt drop in current occurred, which caused the voltage shutdown by the circuit. The large dip in current visible around 7500 ms is associated to a macroscopic detachment of material from the surface of the anode.

When the voltage at V+ fell below the preset value at V−, the output of U1 changed state and switched from 5 V to 0 V. This node was connected directly to the set input of a set/reset flip-flop composed by two NAND ports. The set input was kept low as the output of the operational amplifier while the etching was undergoing, hence one of the two outputs of the set/reset was set to high in this phase. This output was connected to the gate of the MOSFET transistor Q1 controlling the electrochemical cell current, keeping it open while in this state. The other (inverting) output of the flip-flop was connected to the cathode of a plain LED, whose purpose was to promptly signal the end of the etching to the operator. Its anode was biased at 5 V, therefore emitting light while the etching was undergoing. After the drop-off, the flip/flop changed state as the operational amplifier did, inverting the outputs: the LED was turned off while the gate voltage at Q1 was brought to 0 V, cutting the current to the electrochemical cell entirely, stopping the etching.

The reset input of the flip-flop was biased by resistor R6 to 5 V, and connected to a button switch that short circuited it to ground to reset the whole circuit, to be pressed by the operator for the production of successive probes after a shutdown: when the button was pressed, the etching started again if the anode of the electrochemical cell was replaced, causing significant current to flow in it. It is noteworthy that the etching of the tip does not stop completely when the voltage between the electrodes is 0 V. Since the process slowly carried on, it was important to remove the newly formed probe from the etching solution within seconds from the drop-off of the wire: the LED switching off was convenient for this very purpose. The probe had to be thoroughly rinsed with ethanol to remove both the acid and the microscopic Raman-active crystals which could form on its surface, which could cover the apex; the tip was then dried out with a nitrogen flux.

While the circuit itself guaranteed low variance in the probes that this process yielded, an optimisation step had to be taken for setting the free parameter controlling the voltage V−, i.e. the setting of the potentiometer Rpot. For this thesis, a study employing SEM imaging of the tips and TERS tests on standard samples was carried out. The best Rpot value, yielding probes whose apices had average curvature radii of 40 nm with a dispersion of approximately ±10 nm, was around 3000 Ω, to which the potentiostat was kept throughout the thesis for the production of the tips employed in the STM-TERS study in chapter 5. [18, 29, 51–65]

Chapter 5

Candidate reference material for TERS spatial calibration

As a rather novel technique, TERS lacks standardised methods of calibration and procedures for the characterisation of its dimensional measurement capabilities. In TERS, spatial resolution can be substantially different whether topographic mapping or chemical imaging is considered. Indeed, this is caused by the great difference in the nature on the phenomena involved in the two interactions. In AFM, the interaction between the probe and the sample is spatially limited to the area in which the bulk of the van der Waals forces arise, which is roughly equal to the projection on the sample surface of the sphere best approximating the apex (usually estimable to a circle of diameter <10 nm); alternatively, in STM most of the tunnelling current is generated by the closest atoms of the tip and the sample, hence the interaction can be considered to be restricted to probe of almost atomic dimensions. The tip-enhanced Raman signal is instead produced in a volume around the apex, the hotspot, which is greatly variable with tip geometry and alignment of the shaft with the electromagnetic excitation polarisation, if any; furthermore, the distance between the probe and the analyte has a major effect on the TERS signal. Because of these differences between the physics behind the two sources of imaging, which translate into discrepancies in the lateral resolution of the mapping varieties offered by the technique, common SPM calibration is not sufficient for assessing spatial properties of TERS systems, and common SPM standards are not suitable for studying their chemical imaging properties. Nevertheless, reference samples are vital to pave the way to metrological TERS, and to drive this measurement technique to industrial or routine research applications. In fact, appraising reproducibility of dimensional measurements between laboratories and TERS varieties (AFM and STM, excitation wavelength, gold and silver probes, objective geometry, tip angle with respect to sample...) is still an unexplored

domain for this technique. In this thesis, a candidate universal reference sample for the determination of TERS spatial resolution and characterisation was devised, engineered, manufactured and tested.

The results of the work on this standard were published in 2018, and are accessible through the following reference [60].

5.1 Conception

The choice of material and geometric features of a reference sample focussed on spatial calibration is crucial for its usability and for the prospects of its dissemination. The standard should be as physically and chemically stable as possible, both in time and during measurements. For the purpose of measurements at the nanoscale, the spatial features should be easy to locate, either by the addition of markers or by having large areas, visible with optical microscopy, containing repeated, equally spaced identical elements.

For SPM calibration, the most widespread type of calibration surfaces is described in section 3.2: grids (one- or two-dimensional) of physical trenches and/or plateaus. A surface of this kind is usually made of a uniform hard, inert material. Therefore, this type of reference samples is not suitable for the characterisation of the spatial properties of TERS chemical measurements: the surface should feature at least two substances with much different, possibly non-overlapping chemical fingerprints, and at least one should have a high plasmonically enhanced Raman cross section.

Several kinds of samples were considered for the fabrication of the reference specimen for TERS. Because a uniform material was unsuitable, simple structures manufactured by etching or lithography of a bulk substance were discarded. A better option was offered by nanometric objects deposited on inert materials, such as single-walled carbon nanotubes (SWCNTs), graphene, or nanostructures lying on monocrystalline silicon, silicon oxide or nitride, or films constituted by metals such as gold and platinum-iridium. Of course, a conductive surface is preferrable, since it would allow the employment of the reference standard for STM-TERS as well as AFM-based measurements. While SWCNTs and graphene could be very good choices because of their chemical stability, their definite geometries, and their considerable Raman activity and recognisable fingerprint, some issues arise. Nanotubes are some of the thinnest object available, a property which makes them ideal for the characterisation of the geometry of the TERS hotspot; however, a protocol for distributing and strongly fixing the SWCNTs on the surface should be developed so that they are isolated and not moved during the scans, leaving no loose or bundled nanotubes. The presence of particles not soundly fixed makes the probe prone to collect them on its apex, an event which would render the tip

completely ineffective, requiring its cleaning or substitution. Their distribution on the surface would also be unordered. Graphene flakes display borders jagged with angles which are multiples of 60°, making them a unique sample for testing SPM and TERS mapping capabilities and the identification of measurement artifacts; unfortunately, no convenient methods for the production of graphene flakes of dimensions controlled to the extent needed for this study are currently available. The high non-enhanced Raman cross sections of these materials are a problem as well, since they provoke a considerable amount of background, which arises from the excited areas outside the hotspot but still illuminated by the laser during measurement (the *far-field* zone), which perturbs and may even invalidate the measurements, depending on the enhancement factor of the TERS tip employed.

Other nanostructures such as gold or silver nanoparticles functionalised with a highly Raman active material are good candidates as well, but their production is often characterised by a substantial dispersion in their sizes and shapes, and a uniform distribution on a surface without self-aggregation and with good adhesion to the inert metal surface can result problematic, narrowing the choice of materials to very few options. Even after overcoming these issues, the localisation of the optically invisible nanoparticles on the surface would prove to be difficult, and their spatial arrangement would be random. Like carbon nanotubes, SERS-active nanoparticles also contribute greatly to the far-field background. Furthermore, even with completely isolated nanoparticles firmly fixed to the surface with appropriate distances to each other, the resulting sharp differences in height of the analyte surface could affect the output of the measurements during mapping depending on the choice of scanning parameters. They would produce, in this case, image artifacts either in the form of deformations of the spatial features or significant variations of the spectral intensities, including their absence. Besides, utmost care should be taken in order to leave no loose particles on the specimen, else the probe would be likely to become contaminated by them, and to be ruined.

Instead, in this study the choice of materials for the calibration sample fell on a family of organic molecules, thiols, which strongly chemisorb on gold and silver. Thiols are known to form ordered self-assembled monolayers (SAMs) on these metals: this behaviour makes them ideal candidates for a chemical standard. A thiol SAM selectively chemisorbed on a gold film with nanometric geometrical features overcomes all the above-mentioned issues with the other materials which were considered: the surface of such a sample would be flat, with the only difference in height from pure gold to SAM on gold being the one-molecule thickness of the SAM; the far-field would be very low, not measurable with non-enhanced Raman; the structures could be repeated throughout the specimen.

The reference sample was concieved to be potentially employed in every TERS apparatus. In order for it to be viable for measurements with both AFM- and STM-based feedbacks, it had to be conductive; while any metal would satisfy this requirement, gold was chosen both for its high chemical stability in ambient conditions,

and because a surface made of gold or silver, albeit flat, while investigated with TERS gives rise to gap mode (surface-coupled) plasmonic activity, which in turn greatly improves the signal to noise ratio of enhanced chemical maps, allowing the adoption of faster spectral parameters (exposure time, number of averaged scans) for more rapid measurements and lower excitation power, making the sample less prone to photodegradation and heat damage. Even though the reference substrates fabricated in this work did not allow light transmission, the same concept can be applied with other manufacturing materials and techniques for the production of transparent samples suitable for a bottom-illumination TERS apparatus instead of gold evaporation on Si/SiO_2. Good candidates would be a glass support with a thinner, uniformly deposited gold film, or a template-stripped gold surface (see reference [62] for more information on this). In any case, the roughness of the gold film should be as low as possible: on a surface which is too rough or that presents considerable masses of gold, in fact, the SERS effect might arise even without the presence of the tip, which is undesirable because it would give place to a Raman background potentially even higher than the signals from TERS itself.

The patterns typical of SPM reference standards are the most convenient for the calibration of this kind of systems, and TERS is no exception. Hence, for the samples manufactured in this study, a parallel line pattern was adopted, although this was only for simplicity, as a square pattern would be equally valid. This concept of sample is twice convenient: for rather thick thiol lines of known dimensions, the TERS system can be calibrated, and measurements may be compared between different instruments, laboratories and conditions, while very thin lines may be adopted for hotspot mapping, in the exact same fashion of tip mapping in basic SPM, which involves the imaging of structured of comparable dimensions or smaller than the probe apex. The small differences in height between the bare gold and the SAM can also be employed for concurrent usage of the sample as a standard for the topographic imaging in TERS, together with the aforementioned chemical imaging offered by the differences in the presence of the thiol itself.

5.2 Manufacturing

Production of the flat gold layer. The first step in the manufacturing process for nanopatterned thiol self-assembled monolayers on bare gold was the production of the gold substrate itself. The physical characteristics of this layer were critical to the usability of the final sample. Low roughness, absence of SERS signals after molecule deposition, robustness under stress induced by AFM, lack of contaminations, and complete coverage of the hard surface underneath employed as a support were sought. Therefore, electron-beam physical vapour deposition in high vacuum was employed. Chips of 280 nm thick silicon oxide grown on n-type antimony-doped

monocrystalline silicon (by Si-Mat) were employed as the bases for the metal films. The substrates were placed in the vacuum chamber at 5 cm from the spot where the 20 cm^3 capacity molybdenum crucibles, in which titanium and gold resided, were brought during the respective evaporation steps. After a pressure of 10^{-5} Pa was attained, these targets were bombarded by an electron beam originating from a tungsten filament heated by Joule effect. The electron-beam evaporation conditions for these depositions were 60 nA emission current and an electron accelerating voltage of 6 kV, resulting in a nominal evaporation rate of 1 nm/s for 5 seconds for the titanium adhesion layer, and the same emission current and accelerating voltage were employed for the evaporation of gold, resulting in a nominal deposition rate of 1.5 nm/s; probes were subject to variable evaporation times corresponding to different amounts of metal deposited on the surfaces. These evaporation rates were measured by means of a calibrated quartz crystal microbalance placed in the chamber. Several substrates of quite varying gold thicknesses (600 nm to 20 nm) were produced, then analysed to check their suitability for the purposes of this study.

A fundamental parameter for the adequacy of the gold surface as a substrate for the patterned thiol candidate reference standard was its flatness: this is due to the plasmonic activity of nanostructured gold and its potential SERS activity. In fact, a sufficiently rough gold or surface may enhance Raman signals of molecules deposited on it while excited by radiation in the visible range, much like groups of nanoparticles, and this would be unfavourable for the purposes of this study. Therefore, several gold films were evaporated, and their roughness characterised with AFM. The samples were tested for SERS activity as well by performing confocal Raman maps on the substrates, after deposition of SAMs of thiophenol, a thiol often employed in SERS and TERS, and a de facto standard analyte molecule for these measurement techniques [62]. The SAMs were achieved by immersing the surfaces in a 5 mM solution of thiophenol ($\geq$99%, by Sigma-Aldrich) in ethanol (ethanol absolute anhydrous $\geq$99.9% from Carlo Erba) for 18 hours, then rinsing them thoroughly with pure ethanol and drying them with a dry nitrogen flux.

In figure 5.1 semi-contact AFM images of gold-evaporated surfaces with varying deposition times, which translated into metal layers of different thicknesses, are reported. It is noticeable by the maps that grains became smaller with thinner gold layers, hence less deposited material, and that in general the surfaces were smoother at lower evaporation times (thicknesses). Confocal Raman maps on these samples after thiophenol deposition exhibited that thicknesses of hundreds of nanometres of gold resulted in SERS-active surfaces (although not quite efficient ones), with several hotspots on average in maps of 25 μm^2, resulting in a SERS signal of variable intensity always present throughout the specimens; 60 nm gold layers demonstrated much less hotspots, although scattered SERS-active areas were detected. Samples coated with 20 nm of gold displayed no discernible SERS signals

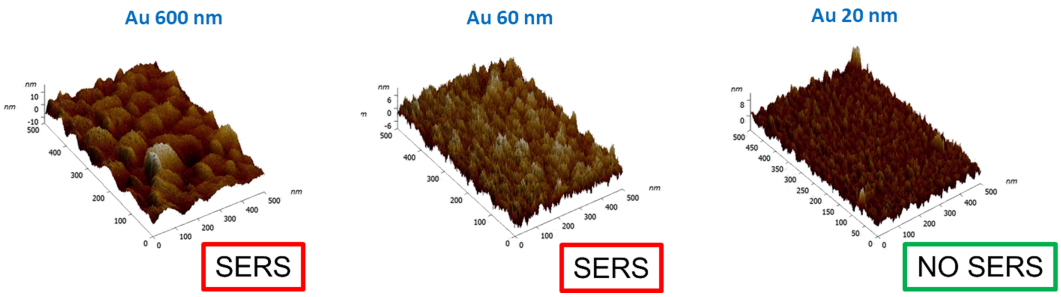

Figure 5.1: Three-dimensional renderings of semi-contact AFM measurements of gold films of different thicknesses produced with electron-beam physical vapour deposition. The gold layers were deposited on 280 nm silicon oxide grown on monocrystalline silicon, with a titanium film of 5 nm between metal and oxide as an adhesion layer. The annotations in figure indicate whether the SERS effect was visible or not on the surfaces after deposition of a monolayer of thiophenol by incubation of the specimen in a 5 mM thiophenol solution in ethanol. Left: 600 nm gold thickness, ISO 4287 parameters S_a = 2.7 nm, S_q = 3.6 nm. Several hotspots could be measured on any zone of the surface. Middle: 60 nm gold thickness, ISO 4287 parameters S_a = 1.9 nm, S_q = 2.3 nm. While this sample was much flatter than the 600 nm specimen, sporadic hotspots were still found. Right: 20 nm gold thickness, ISO 4287 parameters S_a = 1.3 nm, S_q = 1.7 nm. No SERS was measurable even after extensive mapping of the surface. The vertical axes in the figures are not to scale.

with normal spectral parameters employable for SERS and TERS, therefore this thickness was chosen for the gold layer as substrates for the next steps in the manufacturing of the spatial calibration standards.

The roughness measured with AFM could be quantified with the calculation of parameters following ISO 4287 [66], the international standard for measurement and definition of surface texture and roughness, such as the arithmetical mean deviation R_a and the root mean squared deviation R_q of the surface height with the following formulae:

$$R_a = \frac{1}{n}\sum_{i=1}^{n}|y_i| \tag{5.1}$$

$$R_q = \sqrt{\frac{1}{n}\sum_{i=1}^{n}y_i^2} \tag{5.2}$$

where n is the number of sampled points on the surface, and y_i is the vertical displacement of the point i from the horizontal plane which is the average of all data points in the measurement.

Gold layers of 600 nm had a roughness of $S_a = 2.7$ nm, $S_q = 3.6$ nm; thinner films of 60 nm yielded surfaces of roughness $S_a = 1.9$ nm, $S_q = 2.3$ nm; the selected substrate conditions of 20 nm thick gold resulted in ISO 4287 surface roughness parameters of $S_a = 1.9$ nm, $S_q = 2.3$ nm.

Physical robustness tests conducted with AFM showed that the films were stable and solid, and they did not cause the silicon oxide to peel off or to easily deform, withstanding vigorous perturbation with contact AFM, while substrates fabricated in the same fashion but without the titanium adhesion layers turned out to be extremely delicate, and could be damaged by light contact AFM. Examinations with STM tips revealed that even the 20 nm thickness films were fully conductive throughout their entire surfaces, indicating, along with the AFM measurements, that the SiO_2 surfaces were totally covered by the evaporation.

Nanopatterned thiol monolayer fabrication. After the production of the flat gold substrate, the thiol SAMs were deposited selectively on the surface by means of nanopatterned masks covering the gold surface, selectively exposed by electron-beam lithography (EBL), then developed to expose bare gold. After this procedure, the substrates were soaked in a thiol solution until a SAM of the selected molecule fully formed; consequently, the remaining masks were lifted off, resulting in flat gold surfaces with nanometric, custom patterns of strongly chemisorbed thiol monolayes.

A scheme of the fabrication process of each sample is reported in figure 5.2. Poly methyl-methacrylate (PMMA) was spin-coated on the clean gold surface at 6000 rpm for 60 s. The resulting sample was covered by a film of PMMA resist of thickness 50 nm. The resist underwent EBL, and a line pattern was designed in order to obtain a striped mask with trenches of exposed gold. After EBL, the substrates were developed in a 1:3 v/v solution of methyl isobutyl ketone (MIBK) in isopropyl alcohol for 30 seconds, then rinsed thoroughly in pure isopropyl alcohol and pure water, and finally dried with nitrogen.

In this work, the spacing of the impressed stripes was not constant, with the objective of studying the effect of overexposure in this production step. In fact, this is a critical point in EBL, since it is possible for electrons to interact with the resist in such a way that they are scattered and/or produce secondary electrons, in both cases causing partial exposure of surrounding areas whose development may not be intended (overexposure resulting in overdevelopment of the resist). Employing excessive doses, the deriving mask may therefore be deformed with respect to the original design. On the other hand, inadequate doses result in partial exposure, leading to a mask whose trenches, in this case, would not be deep enough to uncover the gold layer beneath or whose resist would only partially removed (underexposure, hence underdevelopment).

Several specimen were produced, and each underwent electron-beam lithography being exposed to different electron doses in the same spatial pattern, ranging from 200 $\mu C/cm^2$ to 870 $\mu C/cm^2$, each with a beam acceleration voltage of 30 kV. The

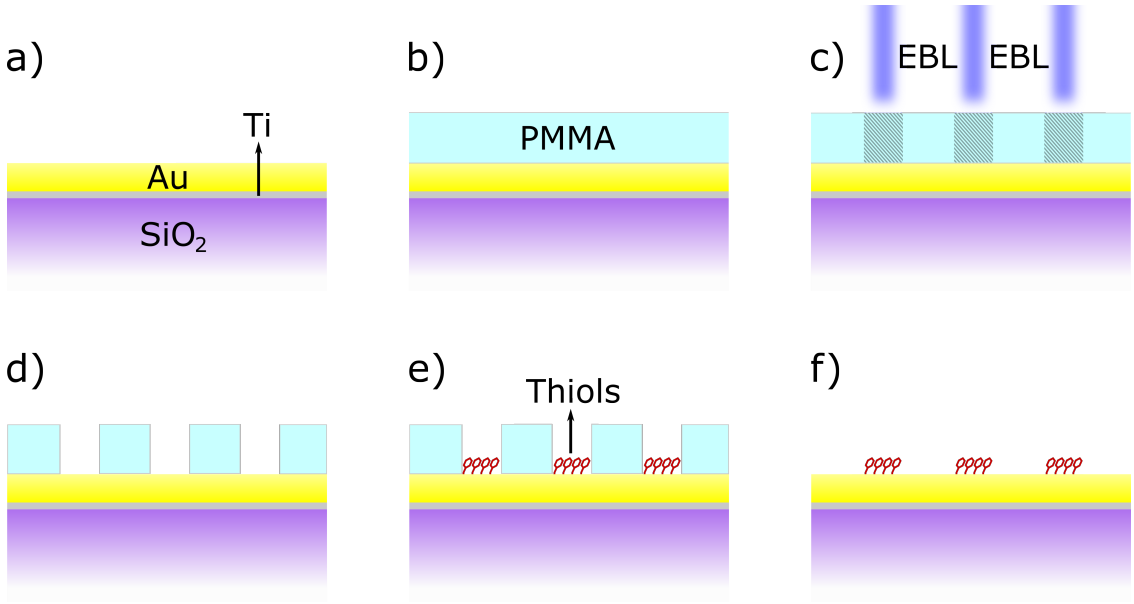

Figure 5.2: Diagram of the steps of the manufacturing process of the candidate reference sample for TERS spatial measurements, consisting in a flat gold surface with a nanopatterned self-assembled monolayer of thiols. (a): a 20 nm flat gold film is deposited on 280 nm thick silicon oxide grown on monocrystalline silicon by electron-beam physical vapour deposition with a 5 nm thick titanium adhesion layer, as described in section 5.2. (b): the surface is spin-coated with 50 nm of poly methyl-methacrylate as a resist. (c): the resist is selectively exposed to electron-beam lithography. (d): the mask is developed in methyl isobutyl ketone, revealing the gold film underneath in the intended areas of the surface. (e): the sample is then soaked in a thiol solution for 18 h, allowing the selective formation of the SAM. (f): the surface is sonicated in acetone to lift off the mask, leaving bare gold with a nanometric pattern of thiol SAM. Adapted with permission from [60]. Published by The Royal Society of Chemistry.

samples were then measured with semi-contact AFM to characterise the masks and to identify the optimal electron dose range for this manufacturing procedure. In figure 5.3, three examples of AFM images are shown, displaying the three different conditions of underexposure, overexposure, and optimal conditions, along with line profiles for each. Knowing that the masks were approximately 50 nm thick, easy identification of suitable masks could be conducted by measuring the height of the trenches and verifying whether they were smaller than this dimension.

It was found that electron doses below 600 $\mu C/cm^2$ resulted in underdeveloped masks, and samples irradiated with doses above 750 $\mu C/cm^2$ showed clear signs of overdevelopment. Measurements on the former specimen, in fact, demonstrated steps of thickness well below 50 nm (the PMMA resist thickness) at the lowest

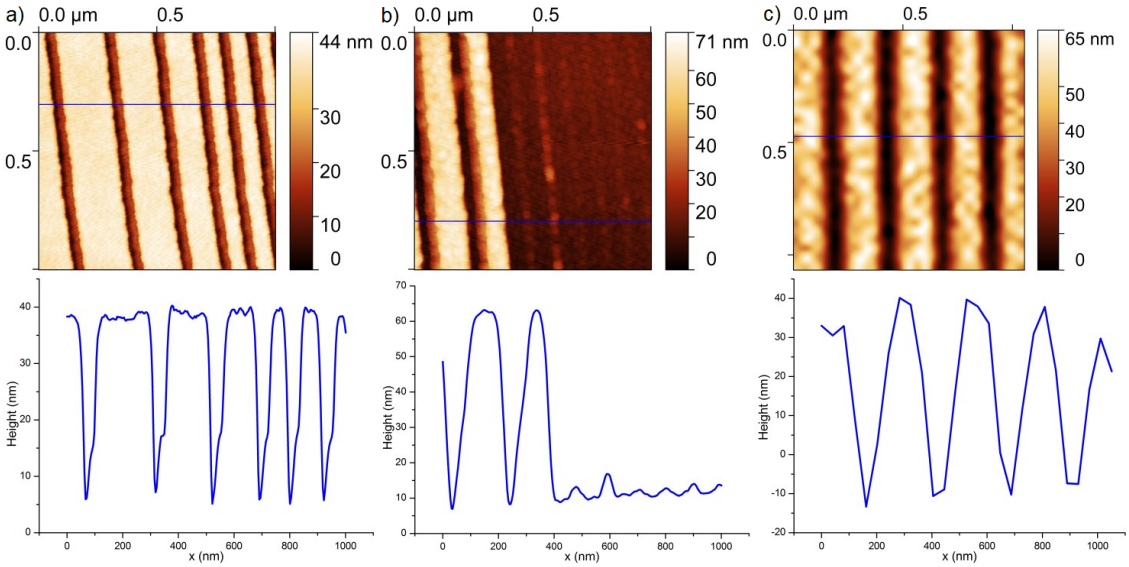

Figure 5.3: Semicontact AFM images (top row) of developed masks exposed to different beam doses during previous electron-beam lithography; for each measurement a corresponding profile (bottom row), taken along the blue lines indicated in the maps, is reported as an example. (a): underdeveloped sample, exposed to a 450 µC/cm^2 dose; the geometry of the EBL lines is preserved along the surface, but the line profile shows that the depths of the depressions in the resist are much lower than its height of 50 nm; furthermore, the profile of the trenches is not rectangular, being deeper in the middle. (b): overdeveloped sample, exposed to a 800 µC/cm^2 dose; several parts of the mask are completely lost due to electron diffusion during EBL, leaving only traces of PMMA on the gold surface, and the shape of the indentations in the remaining mask is lost. (c): surface fabricated with an optimal exposure of 670 µC/cm^2; the gold surface underneath the mask is uncovered, as can be seen from the indentations, which have the same height as the resist thickness; the bases of the trenches are rectangular as intended, and the design of the surface is preserved. Reprinted with permission from [60]. Published by The Royal Society of Chemistry.

doses, while higher ones below but near 600 µC/cm^2 displayed trenches of 50 nm at their highest depth, though they were non-rectangular in profile, which means that the gold layer was only partially exposed by the yet incompletely developed mask. At doses higher than 750 µC/cm^2, some parts of the mask which were designated to remain unexposed were measured as missing, especially in zones of the samples where the distance between the trenches were the closest. This behaviour was caused by excessive electron diffusion in unintended parts of the mask (overexposure). Between the limits of underexposure and overexposure (in the 600 µC/cm^2 to 750 µC/cm^2 range), the resulting depressions were near-rectangular

and had the same height as the mask, hence this was considered as appropriate exposure for the sample. Therefore, an intermediate value of 670 µC/cm^2 was chosen as the optimal dose in this study.

The optimised samples were then immersed in concentrated solutions of thiols. Thiols are a family of molecules which contain a –SH group: sulphur has good affinity with gold and silver, hence these compounds can form ordered self-assembled monolayers (SAMs) on surfaces made of these metals. In this study, two thiols were used as analyte molecules: thiophenol (benzenethiol), a commonplace molecule for TERS and SERS measurements (first introduced in this thesis in section 5.2), which is hazardous to human health, being irritant and very toxic by ingestion, absorption through skin and inhalation [67], and 7-mercapto-4-methylcoumarin (MMC), a non-hazardous substance [68] with much higher Raman cross section in the conditions employed in this study (a property of great utility in the accurate calculation of TERS and SERS enhancement factors, see section 6.3), generating higher enhanced Raman spectra as well. For both analytes, the substrates were soaked for 18 hours either in a 5 mM thiophenol (≥99%, by Sigma-Aldrich) solution in ethanol (ethanol absolute anhydrous, ≥99.9%, from Carlo Erba), or a 1 mM MMC (≥97%, from Sigma-Aldrich) solution in ethanol. After this step and thorough rinses in pure ethanol to remove potential agglomerations of material, the surfaces were sonicated in acetone (≥99.8% from Carlo Erba) for 5 minutes continuously at 37 kHz at a temperature of 30 °C and successively dried with a pure nitrogen flux. After this, the manufacturing was concluded, and the surfaces were ready for measurement.

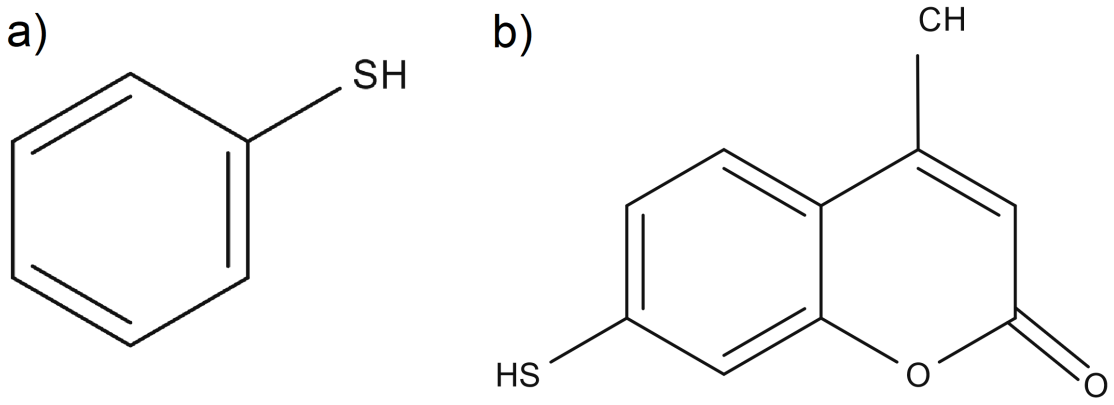

Figure 5.4: Molecular structural formulae of the thiols employed in this study. (a): thiophenol. (b): 7-mercapto-4-methylcoumarin (MMC). [69].

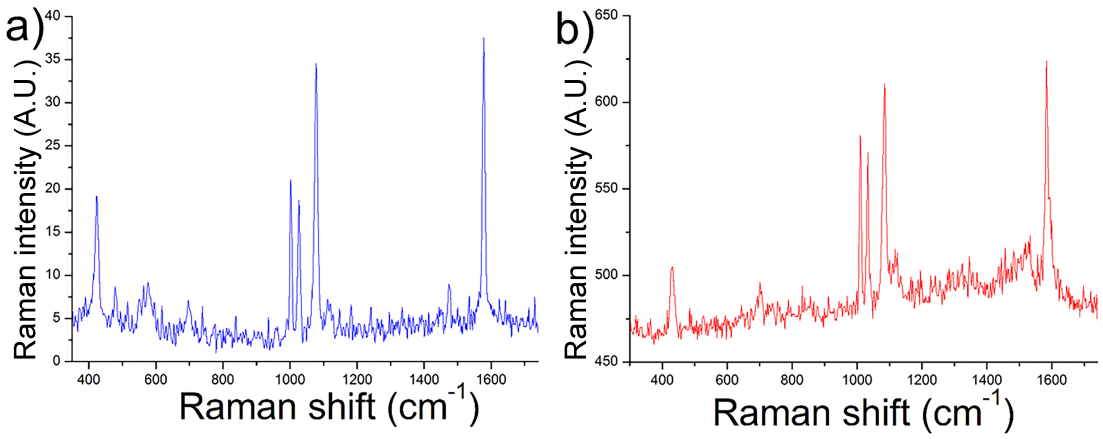

Figure 5.5: Enhanced Raman spectra of thiophenol chemisorbed to gold, excited by a 633 nm laser. (a): SERS spectrum, amplified by gold nanoparticles. Excitation power 0.25 mW, exposure time 0.5 s. (b): TERS spectrum with a silver tip, also acquired with a laser power of 0.25 mW and an integration time of 0.5 s.

Raman shift (cm^{-1})	Vibration
417	$\nu_{CS} + \nu_{AuS}$
998	$\nu_{CC} + \delta_{CH}$
1022	$\nu_{CC} + \delta_{CH}$
1074	$\nu_{CC} + \delta_{CH}$
1581	ν_{CC}

Table 5.1: Assignment of the most prominent plasmon-enhanced Raman bands of thiophenol chemisorbed on gold (ν is stretching, δ is bending). [62]

5.3 TERS imaging

TERS images on the completed samples based on thiophenol and MMC were performed with silver STM-TERS tips and a 633 nm He-Ne laser. STM was chosen as the feedback for this study because of its stricter requirements: since the substrates were devised to be suitable for both STM and AFM controls, successful analysis with the former are sufficient to assess the compatibility with both.

Note that another approach for the use of similar reference samples based on the same concept would be to stop the fabrication process right after the thiol deposition, before the lift-off step, and to employ the surfaces for AFM-TERS as

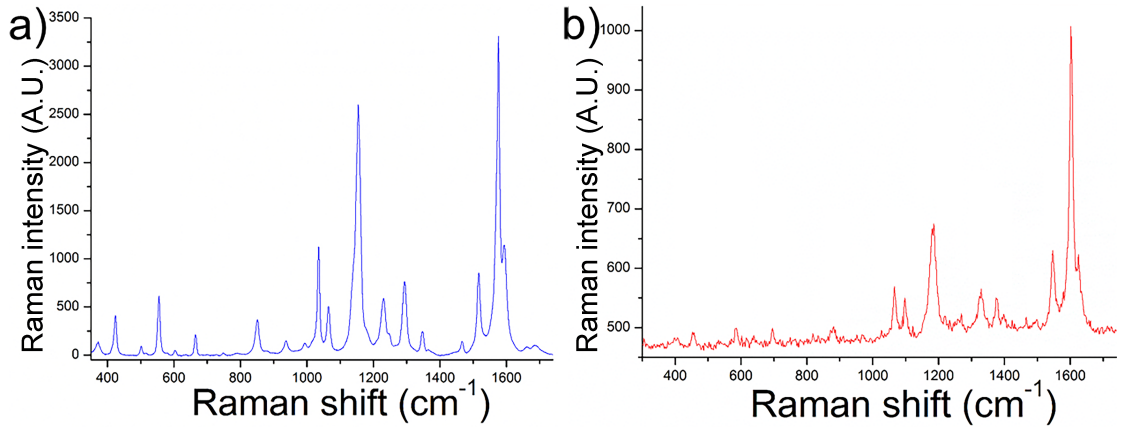

Figure 5.6: Enhanced Raman spectra of 7-mercapto-4-methylcoumarin adsorbed to gold, with a 633 nm excitation wavelength. (a): SERS spectrum, amplified by silver nanospheres, with laser power 8.0 mW and integration time 1.0 s. (b): TERS spectrum with a silver tip, acquired with an excitation power of 0.25 mW and an exposure time of 0.5 s.

Raman shift (cm^{-1})	Vibration
438	Skeletal vibration
570	Ring vibration
685	Skeletal vibration
1057	Characteristic ring vibration
1102	Characteristic ring vibration
1169	ν_{CO}
1318	ν_{CO}
1366	ν_{CC}
1384	δ_{CH_3}
1544	$\nu_{CC} + \delta_{CH_{ring}}$
1593	ν_{CC}

Table 5.2: Assignment of the most prominent 7-mercapto-4-methylcoumarin plasmon-enhanced Raman bands (ν is stretching, δ is bending).

samples with nanometric steps of alternating PMMA and SAM nanostructures. This course of action would have the advantage of having a vertical calibration topographic AFM reference included with the horizontal chemical TERS standard. However, the surface would be partially insulating, excluding the possibility of utilising it in STM-based TERS systems. Furthermore, PMMA is not quite convenient as a material for AFM etalons, as it is easily wearable in contact AFM force conditions. Moreover, the polymer would be a major source of Raman background, arising from the far-field illuminated areas.

The probes employed in the measurements on the samples presented in this thesis were prepared as described in section 4.2, with optimised conditions and the homemade voltage control circuit. All the maps were performed with the same spectral parameters in order for them to be comparable with one another. A single spectrum with an exposure time of 0.5 s constituted each pixel, while the laser power at the sample was 0.25 mW. The STM bias voltage was kept constant at 0.1 V throughout the measurements as well, and the maps were carried out in horizontal raster scans.

TERS chemical intensity images were computed and coloured by employing the intensity of a single enhanced Raman signal depending on the substance. These were calculated by considering the ± 50 cm^{-1} spectral regions centered on the nominal wavenumbers corresponding to the signals; the peaks were best fitted by least square regression with a Lorentzian curve, after a linear baseline background subtraction.

In figure 5.7 the results of STM-TERS measurements on a finalised sample with thiophenol SAM are reported. The image is based on the intensity of the 1074 cm^{-1} Raman signal ($\nu_{CC} + \delta_{CH}$) [62]. The pixel size is approximately 7.5 nm $\times$ 7.5 nm. The maps were carried out in horizontal raster scans. Parallel lines of thiophenol SAM can be appreciated, a geometry corresponding to the indents in the PMMA resist, as it can be noted observing both the map and the line profiles of both. The zones between the SAM lines yielded no Raman signals: no thiophenol intensity was detected on the areas previously covered by the mask, and no TERS spectrum corresponding to PMMA was registered as well. This indicates the validity of the procedure for the lift-off, which completely dissolved the resist, while it did not disperse the SAM. Confocal measurements of the analysed area were recorded as well ("tip out" spectra), resulting in completely flat spectra as expected, since a single thiophenol SAM on a SERS-inactive surface is not detectable with confocal Raman in conditions suitable for TERS with the experimental setup employed in this thesis.

Figure 5.8 shows a TERS image on a nanopatterned thiophenol SAM equivalent to the previous figure, but on a different sample, with smaller features, to test the limits of the sample production process. The EBL system beam diameter, in fact, is several tens of nanometres wide, hence limiting to this dimension the minimum width of the trenches of a fully developed mask. However, underdeveloped

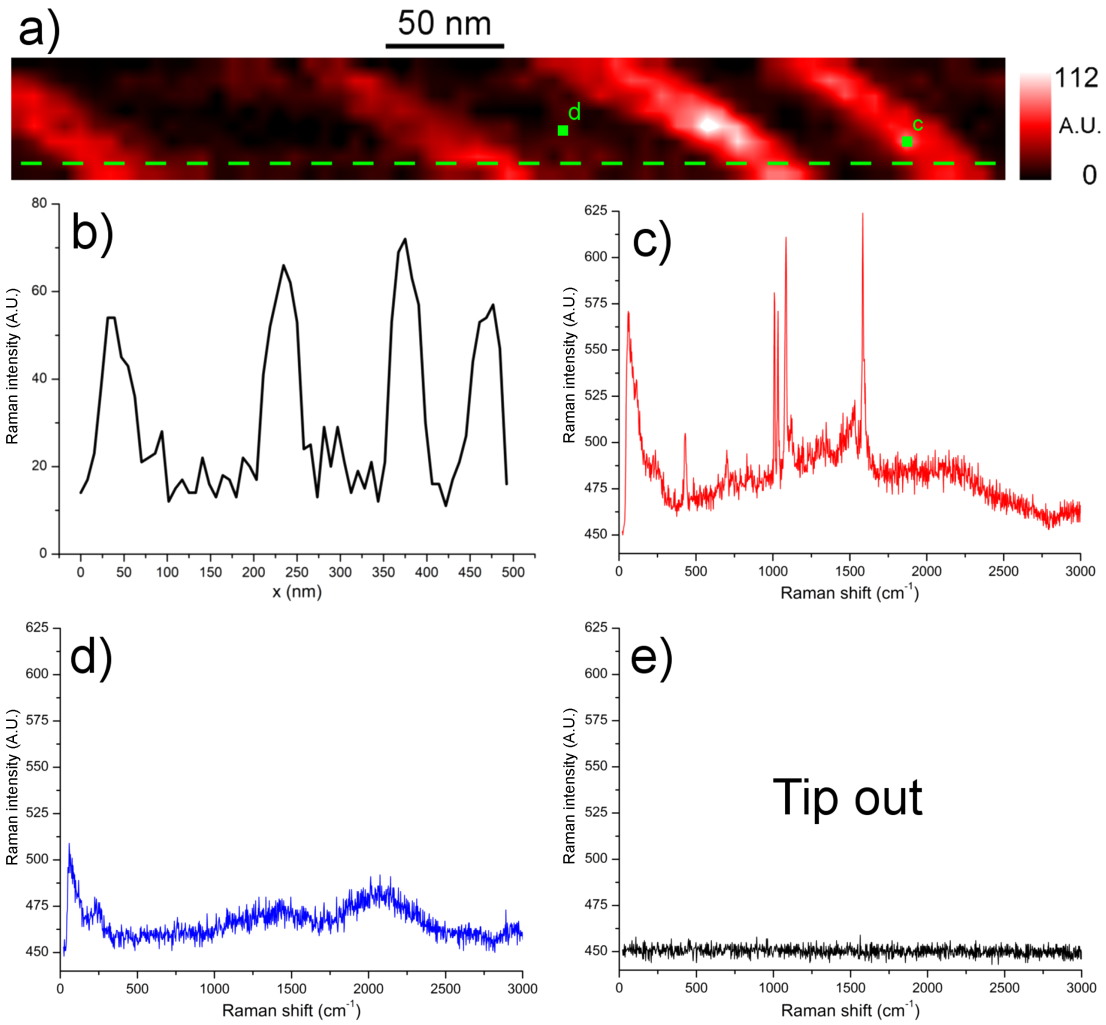

Figure 5.7: STM-TERS chemical image (a) of the thiophenol sample. The colouring is based on the intensity of the 1074 cm^{-1} Raman peak of thiophenol. The map is presented without corrections, except for a Gaussian blur antialiasing filter. The measurement was performed with a 0.25 mW laser power and 0.5 s integration time per pixel. The pixel size is approximately 7.5 nm × 7.5 nm. The geometry of the lines, also appreciable in the line profile (b) corresponding to the green dashed line in (a), retraces well that of the mask presented in figure 5.3c without distorsions. Analysis on single spectra show that no PMMA signal was present on the surface. In (c) and (d), spectra on the SAM lines and on bare gold are reported respectively, sampled on the pixels marked in (a). Confocal measurements on the area (e) displayed no Raman signal whatsoever. Reprinted with permission from [60]. Published by The Royal Society of Chemistry.

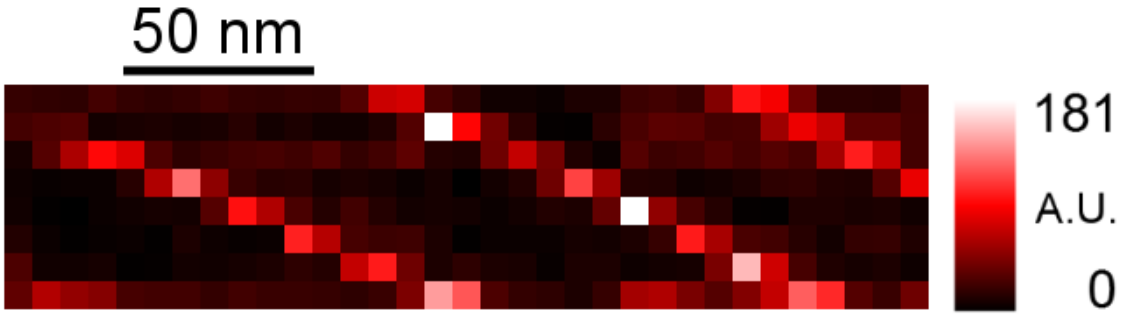

Figure 5.8: STM-TERS raw chemical image of a nanostructured thiophenol SAM with thinner lines with respect to the EBL beam diameter. No antialiasing filter was applied to clearly display each pixel, given the size of the features. The map is based on the 1074 cm^{-1} Raman peak intensity. Progressing the fabrication of the samples with these conditions resulted in SAM nanopatterns smaller than the EBL beam diameter. The measurement conditions were 0.25 mW laser power at the sample, with a 0.5 s integration time per pixel. The pixel side length is ∼7.5 nm. The average width of the lines in the figure is (9 ± 4) nm. Reprinted with permission from [60]. Published by The Royal Society of Chemistry.

resists at doses similar to albeit smaller than the optimal ones yielded trenches with wedge-like profiles in the masks, which uncovered a portion of the gold film underneath, but only partially with respect to the intended design. Proceeding with the manufacturing process with slightly underdeveloped masks with the thiol solution soaking and subsequent mask lift-off led to the formation of smaller, SAM lines. In this case, with an electron dose of 450 $\mu C/cm^2$, a final SAM grating with lines of widths much smaller than the EBL beam diameter was obtained.

After TERS imaging, a line width of (9 ± 4) nm was measured. The feature dimension was calculated as the average and standard deviation of the full width at half maximum (FWHM) of the Gaussian regressions of intensity profiles (defined as the area, after baseline subtraction, of the Lorentzian least square regression on each spectrum) of the 1074 cm^{-1} Raman signal along the scan direction. Since this dimension was so similar to the pixel size of ∼7.5 nm, by the Shannon-Nyquist theorem, faithful imaging of these features cannot be observed at a sampling (spatial) rate lower than the Nyquist rate, which, being defined as half the thickness magnitude of the lines, was in this case 15 nm: this means that the measured stripes were prone to strong aliasing, which distorted their appearance.

The stability of the thiophenol SAM was furtherly ascertained by collecting Raman spectra of the tips utilised to acquire the STM-TERS images immediately after use while approaching them to a clean gold surface prepared in the exact same way as the substrates for the SAMs, as described in section 5.2, to recreate the same enhancement conditions as the maps. In figure 5.9a and figure 5.9b, spectra

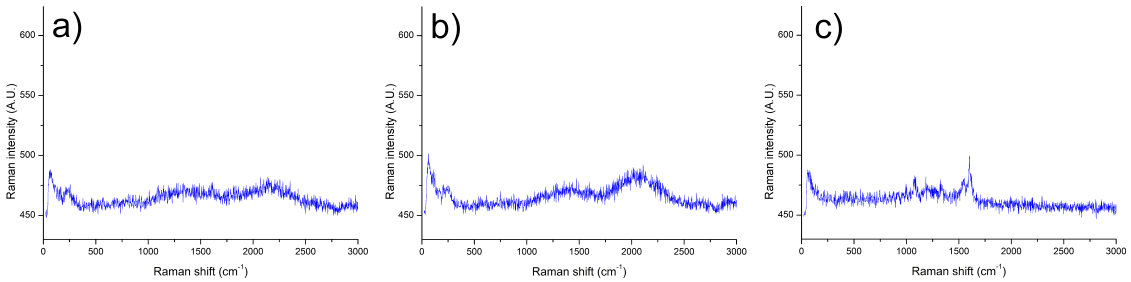

Figure 5.9: Spectra of the tips acquired after the maps presented in figures 5.7 (spectrum (a)), 5.8 (spectrum (b)), and 5.10 and 5.11 (spectrum (c)). Every measurement was performed with the same parameters of each pixel of the corresponding TERS map, on a clean gold surface analogous to the ones employed as foundations for the SAM specimens, in order to recreate the same enhancement conditions. Reprinted with permission from [60]. Published by The Royal Society of Chemistry.

of the tips acquired after approaching them to clean gold surfaces after the maps shown in figure 5.7 and figure 5.8, respectively, are presented. It can be noticed that no thiophenol traces could be detected in these conditions (the acquisition parameters were the same as the images reported in figure 5.7 and figure 5.8), a further indication of the stability of the SAM and the suitability of the surfaces for this kind of measurements.

The presented samples were prepared with 7-mercapto-4-methylcoumarin as well as using thiophenol. MMC is a relatively unexplored probe molecule for plasmon-enhanced Raman applications, which is much safer to handle in concentrations of the solutions utilised for the formation of the SAM. This is important in the European Union framework, as health effects on humans are an important aspect in the choice of chemicals, especially in the perspective of interlaboratory comparisons and approvals. TERS measurements of a MMC-based calibration substrate are shown in figure 5.10. The map is based on the intensity of the 1593 cm^{-1} Raman band, corresponding to C=C stretching of MMC.

Point spectra extracted from the TERS maps (with the same spectrometric conditions) on SAMs of the two thiols employed in this study showed that the most intense MMC TERS signal, at 1593 cm^{-1}, displayed a much higher signal than the strongest thiophenol signals, at 1073 cm^{-1} and 1581 cm^{-1}. The higher intensity of its spectrum and its non-hazardousness suggest that MMC could be a valid alternative to thiophenol as a target molecule for TERS and SERS applications.

However, differently from the thiophenol images, this map shows feeble signals of MMC even in unintended zones of the surface, implying lesser stability of the monolayer during the mask lift-off step of the fabrication process, or while TERS measurement, or both. In fact, single spectra of the employed tip were acquired

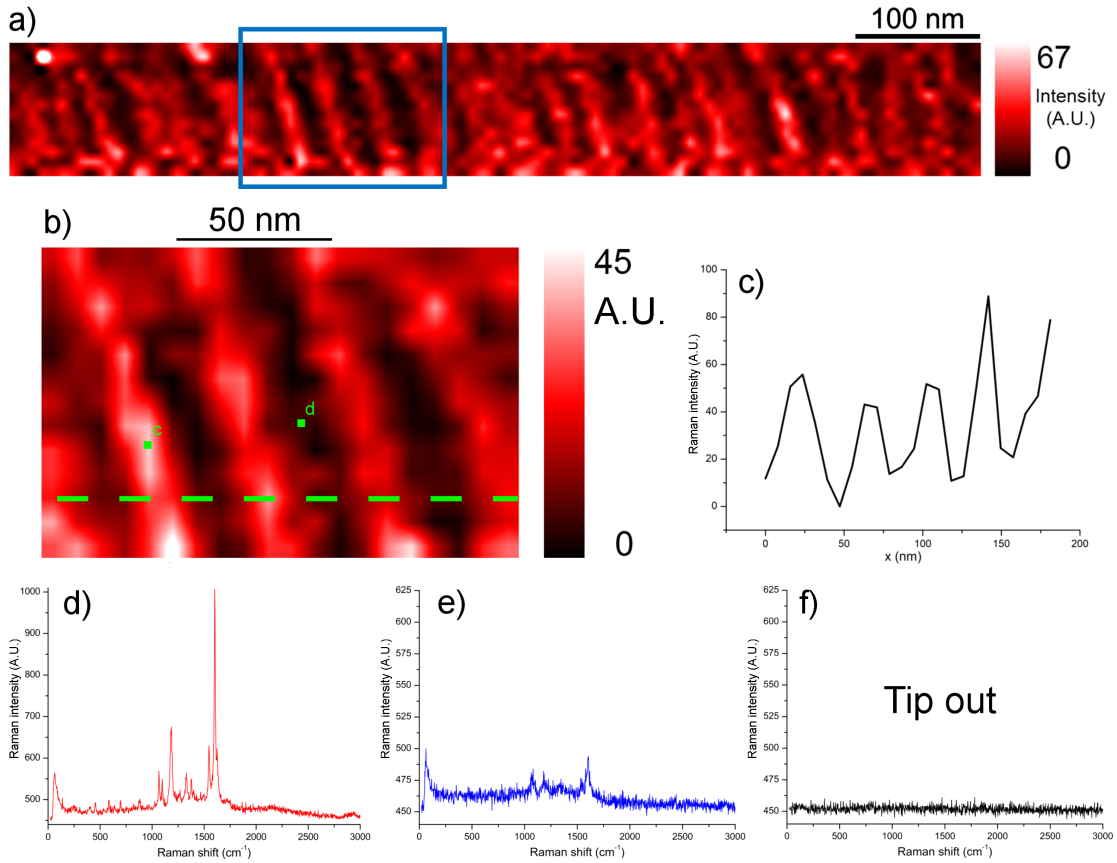

Figure 5.10: STM-TERS chemical image (a) of a nanopatterned 7-mercapto-4-methycoumarin monolayer sample, based on the 1593 cm^{-1} C=C stretching Raman signal of the molecule. No correction was applied to the image, except for Gaussian filtering. The rectangle indicates an area of interest, reported magnified in (b), which contains the lines with the best contrast. The measurement parameters were 0.25 mW excitation power, 0.5 s acquisition time per pixel, pixel side dimension ~7.5 nm. A line profile taken along the green dotted line in (b) is shown in (c). (d) and (e) show spectra corresponding to the pixels marked in (b), respectively in a molecule-rich zone and in an area previously covered by the mask. Note that because of the SAM instability, which led to tip contamination, and possibly because of diffusion of the MMC during mask lift-off, these zones are not completely devoid of MMC signals. A confocal measurement of the area is reported in (f). Adapted with permission from [60]. Published by The Royal Society of Chemistry.

immediately after the MMC map, on a clean Au surface to obtain the same Raman amplification as the TERS image. One such spectrum is presented in figure 5.9c, which shows noticeable traces of contamination of MMC on the tip, indicating that the mechanical stability of the MMC monolayer was less than that of the aforementioned thiophenol SAM, rendering the former not ideal as a basis for this sample, unlike thiophenol.

Of course, from these calibration samples dimensional information on the probe chemical capabilities can be extracted, and a comparison between the TERS chemical and topographic images can be accomplished. For this purpose, the parallel stripes pattern chosen for these substrates was convenient, since it was straightforward to carry out line width measurements, and even a small area mapped with TERS could generate a considerable sample size, since each line and raster scan could be considered an independent sample, on which statistic analysis can be applied. In figure 5.11, the results of such an evaluation on the MMC sample analysed in figure 5.10 are reported. Both the chemical TERS image based on the 1593 cm^{-1} MMC signal and the STM topographic map that was collected concurrently were taken into consideration. The thickness of the monolayer would be difficult to notice with respect to the roughness of the gold layer underneath with AFM, but since these measurements were performed with an STM control, more evident trenches (as opposed to steps) were visible in the topographic image. This was due to the conductivity of the organic SAM being lower than that of the bare gold: the scan was executed in constant feedback mode, hence the probe was bound to get closer to the surface when crossing the SAM lines in order to maintain the tunnelling current setpoint, which resulted in a lesser registered height with respect to the bare gold areas. Each SAM stripe was considered to be an independent repetition of the same width for the sake of these calculations. The line width was defined as the distance between the two edges, at 10% of the maximum depth of the dips in the topographic map, and 10% of the maximum TERS intensity in the chemical image.

The stripes appraised in the chemical map demonstrated an average lateral dimension of $\mu = 28.1$ nm with a standard deviation of $\sigma = 3.9$ nm, while the topograpic STM measurement resulted in an average width of $\mu = 25.9$ nm and a standard deviation of $\sigma = 3.5$ nm. These values indicate slightly broader measurements in the chemical map with respect to STM, which is explicable (and expected) by a larger dimension of the effective probe: the STM interaction generates from a few Å on the tip apex, while TERS hotspots generally have much greater dimensions of tens of nanometres, comparable to apices curvature dimensions. Since in SPM the registered spatial features are the result of convolution between the effective probe sizes and the target features themselves, these values are consistent with the different dimensions of the hotspot and the area from which most of the tunnelling current in STM arises.

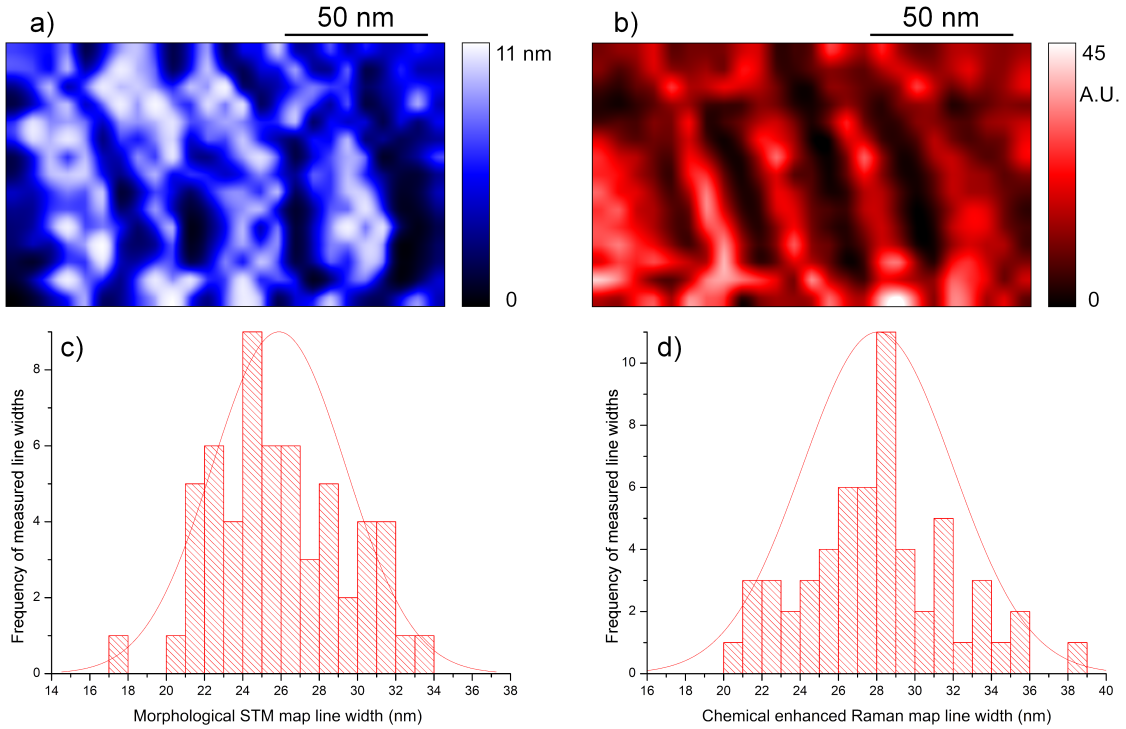

Figure 5.11: Comparison of topographic (a) and chemical (b) maps of a TERS image on a nanopatterned 7-mercapto-4-methycoumarin monolayer. (b) is coloured according to the 1593 cm^{-1} peak intensity. Note that the SAM stripes in (a) were measured by STM as depressions because of their lower conductivity with respect to the bare gold areas. (c) and (d) show statistical analysis of meausements of the lateral dimensions of the SAM stripes (defined as the distance between the two edges, at 10% of their height) with superimposed Gaussian curves of peaks and width equal to the mean and standard deviation of the respective samples, which for the chemical image were average width $\mu = 28.1$ nm and standard deviation of $\sigma = 3.9$ nm, whereas for the STM map were mean width $\mu = 25.9$ nm and standard deviation of $\sigma = 3.5$ nm. Reprinted with permission from [60]. Published by The Royal Society of Chemistry.

The enhancement factor (EF) of the scatterers is a fundamental parameter for TERS and SERS, which can be calculated from the single pixel spectra extracted from the maps. The EF is usually defined [70, 71] as the factor by which the Raman spectrum deriving from the molecules inside the hotspot is enhanced by the tip with respect to the intensity arising from the unaided Raman effect from the same amount of substance. The consequent formula is:

$$\mathrm{EF} = \frac{I_{tip\ in} - I_{tip\ out}}{I_{tip\ out}} \frac{N_{FF}}{N_{NF}} \tag{5.3}$$

where $I_{tip\ in}$ is the intensity of the selected amplified Raman signal in the spectrum measured with the tip approached to the sample, $I_{tip\ out}$ is the intensity of the same Raman band, not enhanced, on the measurand with the tip retracted in the same spectral conditions (laser power, integration time), while N_{NF} and N_{FF} are the amounts of substance in the hotspot (or *near-field*) and in the far-field respectively. In this equation, the contribution of the confocal Raman background is subtracted from the global spectrum acquired during TERS in the numerator, and the ratio between the intensities of the two effects is normalised by the ratio of the number of molecules probed by each effect.

In the case of homogeneous analytes, since $N_i = c_i V_i$, where N_i is the number of molecules, c_i is the concentration, and V_i is the considered volume, equation 5.3 becomes:

$$\mathrm{EF} = \frac{I_{tip\ in} - I_{tip\ out}}{I_{tip\ out}} \frac{V_{FF}}{V_{NF}} \tag{5.4}$$

in which V_{NF} and V_{FF} are the hotspot volume and the microscope focal (usually confocal) volume respectively. In the case of this study, i.e. planes of ordered SAMs, equation 5.4 is equal to:

$$\mathrm{EF} = \frac{I_{tip\ in} - I_{tip\ out}}{I_{tip\ out}} \frac{A_{FF}}{A_{NF}} \tag{5.5}$$

where A_{NF} and A_{FF} are the areas defined by the section of the hotspot by the SAM surface and the projection of the confocal volume on the surface respectively, in the assumption of having the substrate in optical focus and reasonably orthogonally orientated to the optical axis, as is the case of a top-visual apparatus such as the one employed in this thesis. In this study, A_{NF} was assumed to be equal to the area of a circle whose radius is equal to the average tip apex radius of the probes yielded by the manufacturing process of optimised STM-TERS tips described in section 4.2.

The EFs were calculated by employing the Lorentzian curves best fitting the peaks as the enhanced Raman intensities. Conventional Raman spectra were registered on the analysed areas by taking confocal Raman spectra after dismounting the tip from the TERS apparatus, with the same spectral conditions as each pixel of the TERS maps. However, in the framework of this study, $I_{tip\ out}$ resulted to be null, since both the thiophenol and the MMC SAMs have non-enhanced cross sections too low for detection with the excitation power and detection parameters employed for the TERS maps presented here.

Formulae 5.3, 5.4 and 5.5 are not valid in the case of $I_{tip\ out} = 0$ .The EF calculation result is heavily dependent on this value: an arbitrary or liberal choice would lead to highly inaccurate values of EF, with resulting errors that could be of several orders of magnitude. While an accurate enhancement factor value cannot be determined with these data, a lower limit for its value can be assessed:

by considering $I_{tip\ out}$ right below the lowest detectable Raman signal in the far-field spectra, a lower bound for EF can be calculated. A conventionally accepted threshold for the demarcation of a detection limit in spectra is three times the standard deviation of the noise: by employing this parameter $N_{tip\ out}$ in lieu of the null $I_{tip\ out}$ in equation 5.5 as the maximum possible intensity for the thiol signal in question, i.e. the highest undetectable signal in the spectra acquired with the tip retracted, information on EF can be extrapolated by using the following formula:

$$\mathrm{EF} > \frac{I_{tip\ in} - N_{tip\ out}}{N_{tip\ out}} \frac{A_{FF}}{A_{NF}} \tag{5.6}$$

$N_{tip\ out}$ was determined by employing the standard deviation value of the spectrum in the 1750 cm^{-1} to 2250 cm^{-1} region, which was devoid of Raman signals, after background subtraction. In order to employ this method and equation 5.6, the height of the peaks, interpolated by Lorentzian functions after background subtraction, were utilised as the enhanced Raman intensities $I_{tip\ in}$ instead of their areas, since the limit of detectability defined as three times the standard deviation of the noise concerns the height of the signal.

The lower bounds for the TERS enhancement factors were calculated to be $\mathrm{EF} > (2.2 \pm 0.5) \times 10^7$ for thiophenol, and $\mathrm{EF} > (1.0 \pm 0.2) \times 10^8$ for MMC.

Another formula for the estimation of the EF of enhanced Raman in the case of undetectable non-enhanced signals, adapted from [72], is the following:

$$\mathrm{EF} = \frac{I_{tip\ in} - I_{tip\ out}}{1 + I_{tip\ out}} \frac{A_{FF}}{A_{NF}} \tag{5.7}$$

from which an $\mathrm{EF} = (1.7 \pm 0.4) \times 10^8$ for thiophenol, and an enhancement factor of $(7.4 \pm 1.6) \times 10^8$ for MMC is evinced.

It is worth noting that the intensity of the enhanced signal in the SAM-covered areas changed greatly throughout the TERS images. This behaviour was caused by the variability of the tip-sample distance during the scans. It is known, in fact, that this is a crucial factor from which the intensity of the TERS signal heavily depends (see equation 1.33). Since the probe-surface distance in SPM revolves around the choice of the setpoint, which is arbitrary in some measure, and since said apex-sample separation differs from tip to tip even at the same setpoint because of the uncontrollability at the nanoscale of the apices radii and geometries, and the dispersion of the mechanical properties of the probe cantilevers in AFM as well, arranging a comparison or reproducibility study in TERS intensity between different tips simply by probing the same standard is not viable even by acquiring point spectra, let alone during actual scans. This issue was tackled in another study during this thesis, and presented in section 6.1. [25, 33, 46, 47, 60, 62, 66–89]

Chapter 6

Procedures for the accurate calculation of the enhancement factor, and for the improvement of its precision and magnitude

TERS is a vastly versatile measurement technique, and, given its great range of possible applications, it has a large margin of growth in its use in the next years. In order for its results to be comparable amongst laboratories and experimental apparatus types, the need for standardisation of procedures, definitions and reference samples is critical. While in recent years endeavours have been made to take on this necessity, from the development of reproducible tips to actual interlaboratory studies [18, 54, 60, 62, 63] and including the work presented in this thesis in section 5, there is a lack of common standards and procedures throughout the community. The very definition of one of the most important concepts in TERS, the enhancement factor (EF), is not universally accepted nor is it always applicable (more on that in section 6.4).

In this thesis, efforts have been made in order to develop procedures to reduce variability in TERS measurements, to extend the view of TERS as a practical application of SERS reduced to a single nanoparticle by recreating the most common SERS nanostructure arrangements with TERS, leading to isolated probe measurement and tip-to-tip dimers actualisation, the latter of which is promising to increase TERS effectiveness. An ab initio analysis of the procedures to accurately calculate the enhancement factors in TERS and SERS, even in case in which enhanced and non-amplified Raman spectra cannot be acquired in the same conditions, has been made as well.

The work on the standard approach for the precise, reproducible characterisation of TERS probes capabilities, along with the following study on a novel substrate for further magnification of the enhancement factor, and its accurate calculation, was published in 2019, and is accessible through the following reference: [61].

6.1 Novel procedure for TERS probes capabilities assessment: the isolated tip

Before tackling the issues in the measurement of TERS and SERS enhancement factors, it is worth noting that the amplitude of a TERS signal is dependent in any given moment on a number of factors which may not be immediately apparent. Even at fixed excitation wavelength and laser power and polarisation, the magnitude of the enhancement is extremely sensitive to the distance between the tip and the target molecules [90], their positions in the hotspot, and their orientations with respect to the polarisation of the enhanced electric field, which is highly directional (as discussed in section 1.4). These considerations are much more influential in TERS than in SERS or non-amplified Raman, since the amount of substance analysed by the former is much smaller, therefore these influential factors are not averaged out by the large amount of randomly organised scatterers which are usually present in the large focal volume investigated by an optical microscope in the latter two techniques.

Moreover, other aspects that affect the magnitude of TERS are connected to its SPM control. The separation between the tip and the sample, while intended to be constant, in fact varies erratically for a number of non-reproducible reasons, even while the system is not moving during a scan: mechanical noise, non-instantaneous response of the electronics driving the feedback, sounds and humidity (only if executed in ambient conditions), electrical noise, variations in temperature of the probe, the sample and the rest of the experimental apparatus itself, and chemical changes of the interacting surfaces do influence the tip-enhanced spectra routinely. The effect of the fluctuations of the probe-sample separation is much more conspicuous during scanning, when the local surface roughness, hence the amount of analysed substance, inevitably changes (except for very specific atomically flat samples). Furthermore, probe speed and PID controller settings, which are a somewhat discretionary choice of the operator and can vary greatly between experimental setups because of the differences in probe types and in excitation and collection efficiencies, affect the extent of the natural SPM artifacts and the motion, stability and repositioning speed of the probe on the sample. The decision of the setpoint is also arbitrary and not standardised, with a wide range of effective values which can result in radically different EFs, but nevertheless equally

valid TERS spectra and images. This concern can be appreciated in every TERS image discussed in section 5.3: the Raman intensity on the thiol monolayer stripes changes considerably throughout each map, even though the amount of molecules involved in the scattering process in each pixel is supposedly constant (with the obvious exception of the edges of the thiol lines).

These influential factors render comparisons between laboratories and experimental setups difficult, and they make attaining reproducibility and even repeatability of TERS measurements a challenge. In this thesis, a procedure for the standardisation of the estimation of the enhancing capabilities of TERS probes by which the aforementioned influencing aspects are bypassed is proposed and applied to the optimisation of the production of AFM-TERS gold-covered tips for resonance to a 633 nm excitation wavelength. The improvements on reproducibility brought by this approach were also analysed by comparing the dispersion of data acquired with this alternative disposition with that of the same tips and measurements carried out in gap mode, the typical method for EF assessment in TERS.

The standardisation method consists in the placement of the probe molecule directly on the tip, leaving it isolated from any surface. In this manner the tip-sample distance remains unchanged throughout the measurement, and so does the amount of analysed substance and its position and orientation with respect to the hotspot. A schematic depiction of the proposed procedure with respect to standard TERS measurement on the same molecule is shown in figure 6.1. Only thiophenol was utilised as a probe molecule for the AFM-TERS probe optimisation study, but measurements on the isolated tip setup with this molecule along with other two were made and compared. This will be discussed in sections 6.2, 6.3, and 6.4.

The specifics of the manufacturing process of the AFM-TERS employed in this study were discussed in section 4.1. Monocrystalline silicon top-visual AFM tips were coated with gold layers of different thicknesses by sputtering for plasmon resonance at 633 nm. After this step, the probes were immersed in a 5 mM thiophenol solution in ethanol and kept in it for 18 hours, then rinsed in pure ethanol and dried with a nitrogen flux. This allowed the formation of a thiophenol self-assembled monolayer (SAM) on the tip. The probes were employed in the ensuing measurements within 24 hours from this step.

Each tip was first employed as isolated. To do so, the probes were placed and fixed face-up on the TERS top-visual apparatus stage, so that each apex was pointed towards the objective while maintaining the same angle with respect to the optical axis. Focus on the apices was reached before starting the acquisitions. Each tip was measured several times, each time removing it from the sample holder and placing it again before focussing again on the apex, in order to test the effects of this source of variability (different operators carried out this action to take this source of variability into consideration). After this procedure, the very same tips were mounted to be employed as AFM-TERS probes, then approached to a clean gold surface manufactured as the ones described in section 5.2 as the foundations for

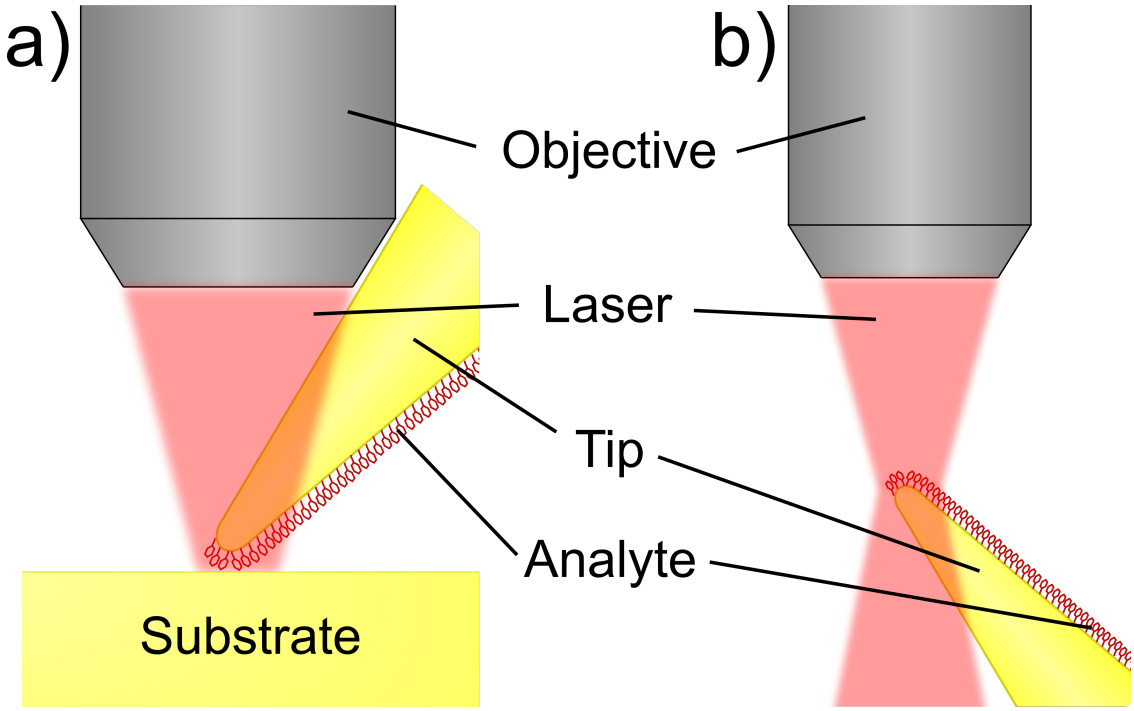

Figure 6.1: Schematic comparison between the standard approach for acquiring the TERS signal of a molecule (a), and the isolated tip method for spectral measurement proposed in this work, for the elimination of major sources of variability by depositing the analyte directly on the probe (b). Note that in gap mode (a) usually the molecules lie on flat surfaces instead of residing on the tip: nonetheless the depicted disposition was considered equivalent to it, and advantageous for the presented study as it allowed the employment of the same probes in both approaches. Reprinted with permission from [61]. Copyright 2019 American Chemical Society.

the nanopatterned SAM reference samples. The probes were maintained in static contact throughout the measurement, and optical focus was achieved as before, then spectra were acquired. This was repeated several times per tip as well, varying AFM settings within their valid ranges to take into account the discretion in their choice. The specifications employed for the spectra were 1.5 mW laser power with a wavelength of 633 nm, and a single acquisition with a duration of 60 s in both configurations.

The results of these measurements are shown in figure 6.2. Probes covered with nominal gold thicknesses of 30 nm, 60 nm, 90 nm and 120 nm were produced. While the tips with a 30 nm gold layer manifested little or no TERS capabilities, the other samples showed various degrees of enhancement. Observing the average intensity of the 998 cm^{-1} $\nu_{CC} + \delta_{CH}$ enhanced Raman band (best fitted by least square

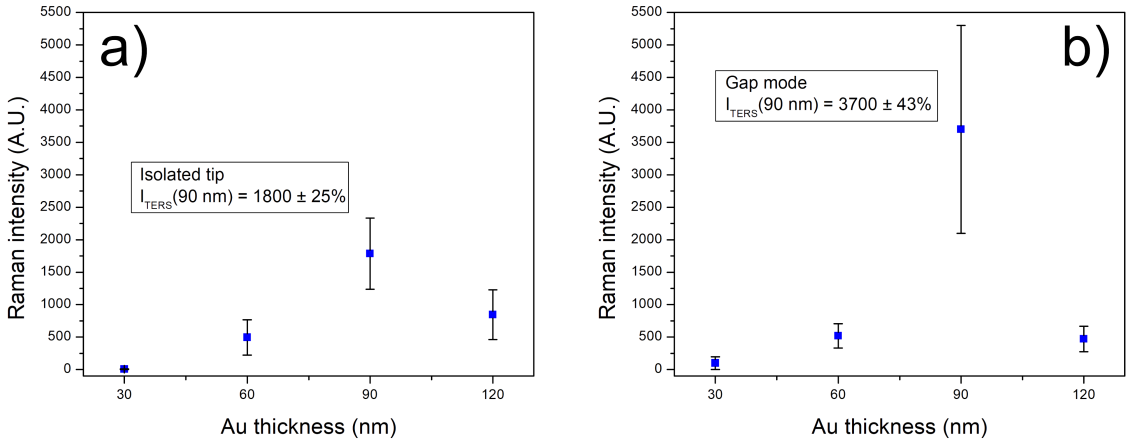

Figure 6.2: TERS average intensities of thiophenol SAMs chemisorbed on AFM-TERS tips as a function of the gold layer thickness deposited on them. (a): isolated tips intensities of the 998 cm^{-1} thiophenol band. (b): magnitude of the signal by the same tips employed in gap mode. Error bars represent standard deviations of the measurements. In both configurations, 90 nm was found to be the most enhancing gold thickness value, but gap mode measurements exhibit much higher data dispersion (43% relative standard deviation) with respect to spectra acquired in the isolated tip procedure (25%), demonstrating that this approach decreased TERS variability. Reprinted with permission from [61]. Copyright 2019 American Chemical Society.

regression with a Lorentzian curve after background subtraction) of each spectrum, from both the isolated tip and the gap mode configurations could be evinced that the 90 nm probes were the most efficient and, as expected, gap mode yielded more intense signals with respect to the uncoupled nanoparticles. The relative standard deviation was calculated to quantify variability of the intensities, and was found for the 90 nm probes to be 43% in gap mode, and only 25% when the tips were isolated, validating the hypothesis that the latter arrangement is able to increase precision in TERS measurements.

The probes were found to be usable for further measurements after they were covered in a thiol SAM. Figure 6.3 shows a TERS spectrum acquired with a 90 nm gold layer tip employed after coverage with a MMC SAM on a flat gold surface covered by a thiram monolayer, in contact mode. It was verified that the surface did not yield any thiram Raman signal without the tip at the conditions employed for the measurement. In the spectrum, Raman bands ascribable to both compounds are visible. The concept of employing a functionalised probe for TERS measurements using the molecule on the tip as an internal standard was already explored as a proof-of-concept by *Bortchagovsky, et al.* [91]: the combination of the

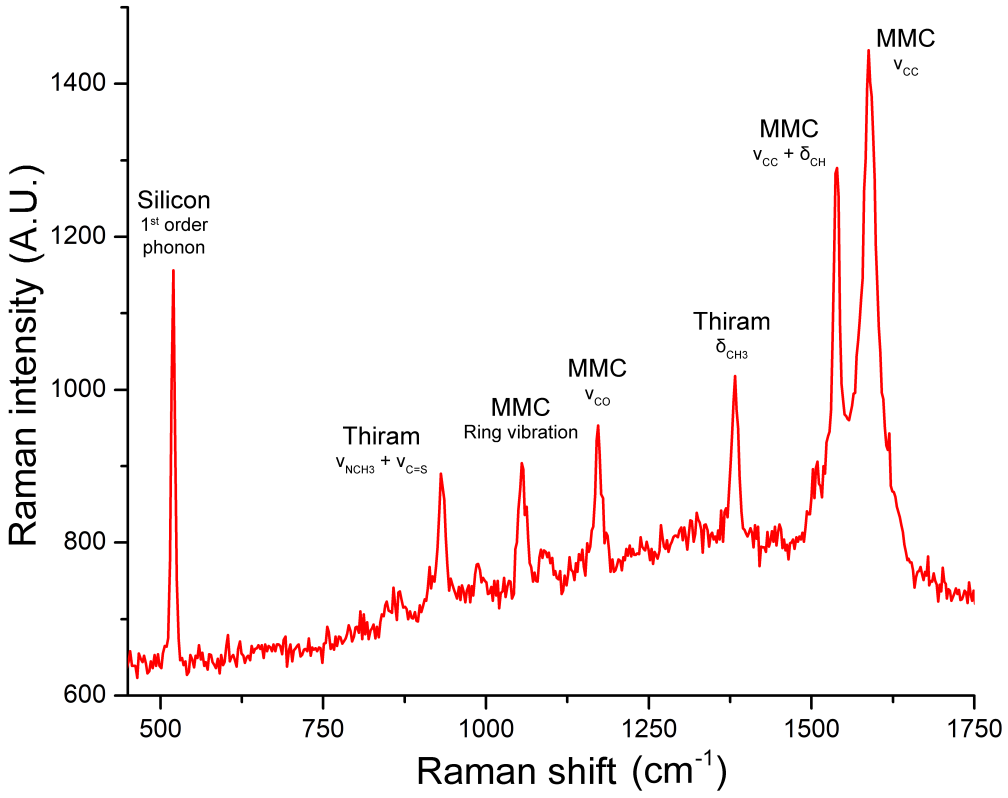

Figure 6.3: Spectrum of an optimised gold AFM-TERS tip functionalised with a monolayer of 7-mercapto-4-metylcoumarin (MMC) in contact with a thiram monolayer formed on a flat, SERS-inactive gold surface. Characteristic signals of both molecules are visible. Because of the silicon core of the tip and the SiO_2/Si surface foundation, a noticeable Raman band ascribable to monocrystalline silicon is present. Acquisition parameters were 1.5 mW laser power and 1 s integration time.

isolated tip procedure for characterisation of enhancing capabilities of probes with the possibility of actually employing them in measurements on samples opens up prospects for the improvement of TERS comparability and standardisation.

Since the 90 nm gold layer tips were deemed to be the most enhancing, these were employed as the AFM-TERS probes utilised in the studies discussed in the following sections.

6.2 Improving TERS enhancement: tip dimers

The previously discussed isolated tip configuration can be employed to experimentally study the plasmonic enhancement effect beyond the scope of this thesis. This arrangement and gap mode TERS, in fact, can also be seen as singular cases of two of the most common configurations in SERS involving a single hotspot: an isolated nanoparticle (for example a single scatterer suspended in a solution), and a nanoparticle lying on a surface (e.g. when it is deposited). Nevertheless, another disposition often occurs in SERS, which is the case of nanoparticles placed in close distance (<10 nm) from each other, commonly referred to as *dimers*. In the gaps between particles, in fact, more potent hotspots are created with respect to the isolated nanostructures, as discussed in chapter 1 [4, 79, 92].

This arrangement could be recreated as a singular instance by employing a pair of TERS tips, one of which mounted on the SPM as a probe and the other fixed on the stage to act as a sample, by seeking contact between the two apices using fine SPM control. Unfortunately, this would be extremely difficult to achieve because of the mechanical and morphological properties of SPM probes: the aspect ratios of the tips are in fact very unfavourable, since they are engineered specifically to avoid tip imaging; furthermore, the properties of AFM cantilevers are not encouraging for this achievement, because they are devised to flex and vibrate in response to the slightest forces, and mapping a highly mobile surface with SPM is notoriously difficult if not downright impossible if a precision in the order of the nanometres is sought.

In this study, instead, a specific substrate for an easy practical realisation of tip-tip dimers was devised and manufactured, consisting in a grid of mechanically stable, identical pyramidal tips with gold surfaces protruding from a flat sample. In this geometry, the sample is much more easily approachable, and the placement of the SPM tip on the apex of a substrate pyramid could be carried out in a straightforward way. This fully conductive, easily reproducible, large-area sample (5 mm × 5 mm in this study) was measured with AFM-TERS in this work, but given its characteristics, such a concept is suitable for STM-TERS measurements in the same fashion.

In figure 6.4, the manufacturing steps for the production by nanoimprinting template lithography of the tipped substrate for the achievement of tip dimers is shown. From a monocrystalline silicon surface, a mould is obtained by potassium hydroxide (KOH) anisotropic wet etching, which is known to be capable of generating very reproducible pits in the shape of inverted square-based pyramids. It is worth noting that this geometry, when covered by an appropriate gold film, is per se a viable SERS surface. In this thesis, commercial Klarite™ substrates by D3 Technologies Ltd. were employed as moulds after removal of their superficial gold layer. Polydimethylsiloxane (PDMS) was prepared so that, when cured, it would be as solid as possible. The PDMS was cast onto the mould, enclosed and pressed

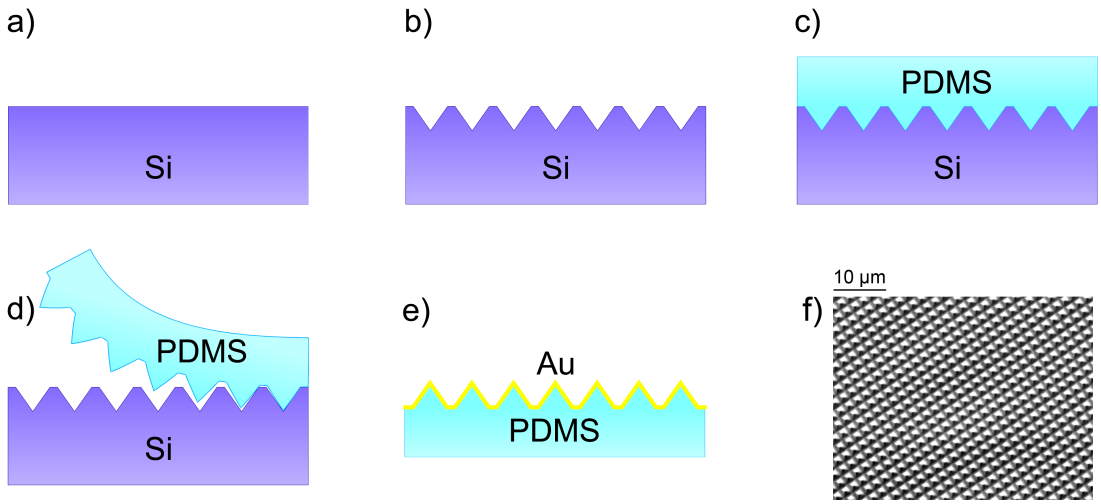

Figure 6.4: Schematic depiction of the manufacturing process of the tipped substrate for the practical realisation of tip dimers. Starting from monocrystalline silicon (a), KOH anisotropic etching is executed to obtain depressions shaped as inverted pyramids (b), on which polydimethylsiloxane (PDMS) is cast, and cured at 100 °C for 30 minutes until solid (c), then detached from the silicon mould (d) and sputtered with gold and a titanium adhesion layer (e). The resulting surface presents identical square pyramidal tips in a large area, observable in a SEM image in (f), ready for approach with TERS. Adapted with permission from [61]. Copyright 2019 American Chemical Society.

in glass slides, then put in a furnace at 100 °C for solidification for 30 minutes. After removing the cast, the resulting solid PDMS tipped substrate was fixed on a silicon support to reduce the risk of mechanical stress during manipulation on the metal layer soon to be deposited, then it underwent titanium and gold sputtering with the same parameters as the optimised AFM-TERS tips (90 nm gold deposition after sputtering of titanium for a 5 nm thick adhesion layer).

The produced samples were characterised by semi-contact AFM and scanning electron microscopy (shown in figure 6.5a). The resulting surfaces presented a square grid of identical pyramids of heights close to 1 µm, spaced 1.5 µm. The tips exhibited angles of 70.6°, as expected from casts deriving from the mould produced by the KOH anisotropic etching of monocrystalline silicon. Since the bulk of the pyramids was made of PDMS, attention had to be made during AFM measurements not to damage the substrate: while semi-contact AFM does not heavily stress analysed surfaces and therefore could be carried out on this samples

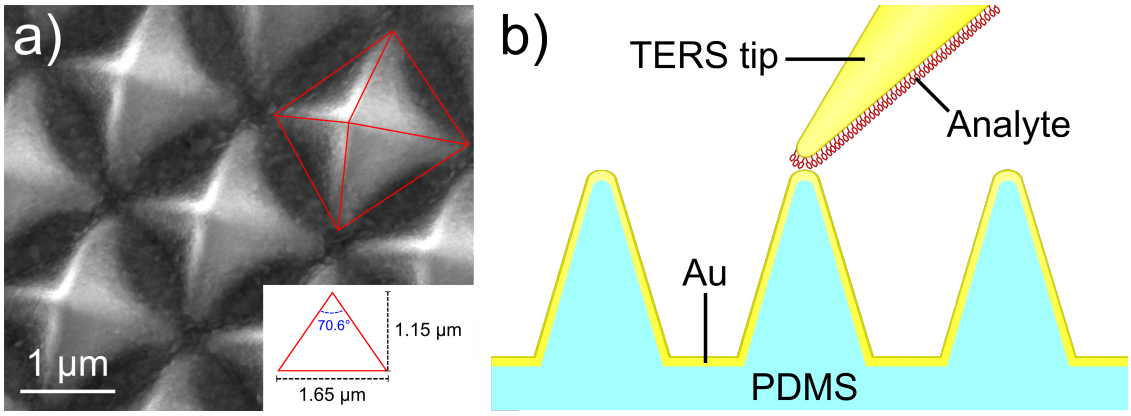

Figure 6.5: (a): scanning electron microscope image of the metallised substrate for tip dimers with red line overlay on the edges of a protrusion as a visual aid (inset: side view scheme of dimensional properties of a pyramid). (b): schematisation of a tip dimer realised with this surface, as performed in this study. Reprinted with permission from [61]. Copyright 2019 American Chemical Society.

without risk of damaging them, only light forces are tolerated by such a material, hence contact AFM approaches, needed for maximising enhancement, had to be executed gently, not to deform the bulk or puncture the gold layer.

After the manufacturing of the tipped substrates, AFM-TERS measurements were realised in tip dimer configuration. In order to do so, the analyte molecules were once again chemisorbed on top-visual AFM-TERS tips, which were used as "active" tips mounted on the SPM system, whose deflection was monitored and used for feedback, while the tipped sample was fixed on the piezoelectric stage. The AFM-TERS probes were fabricated with the optimised procedure described in section 4.1.

Three different molecules were employed as analytes in order to demonstrate the adaptability of this concept: the thiols employed for the study presented in section 5, namely thiophenol and 7-mercapto-4-methylcoumarin (MMC), and thiram (tetramethylthiuram disulfide), a law-regulated fungicide, pesticide and pest repellent with widespread use in agriculture for human consumption, whose trace detection is important for lawful regulations compliance. All three molecules chemisorb spontaneously on gold and silver to form stable self-assembled monolayers, which was quite a convenient disposition since it allowed high reproducibility and ease of calculation of the analysed amount of substance, in addition to the inherent known, fixed chemical bond distance.

To coat the probes with SAMs of these molecules, each freshly evaporated tip was soaked for 18 hours in an ethanol solution of either molecule with the following concentrations: 5 mM for thiophenol (≥99%, by Sigma-Aldrich), 1 mM for MMC (≥97%, Sigma-Aldrich), and 8 mM for thiram (97%, by Alfa Aesar). After this step,

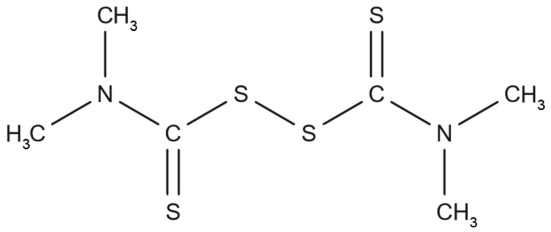

Figure 6.6: Structural formula of thiram [69].

Raman shift (cm^{-1})	Vibration
556	ν_{SS}
928	$\nu_{NCH_3} + \nu_{C=S}$
1139	$\rho_{CH_3} + \nu_{CN}$
1372	ν_{CC}
1444	Symmetrical δ_{CH_3}
1508	$\rho_{CH_3} + \nu_{CN}$

Table 6.1: Assignment of the most prominent plasmon-enhanced Raman bands of thiram (ν is stretching, δ is bending, ρ is rocking). [93]

they were thoroughly rinsed with pure ethanol, then dried with a nitrogen flux. The measurements were executed within 72 hours after this step and the production of the tipped substrates, to avoid possible degradation or contamination of either.

The results of the TERS measurements on tip dimers with each analyte are summarised in figure 6.7, in which they are compared with the other two common arrangements for nanoparticles explored in section 6.1, isolated tip and gap mode. The analysed Raman signals were the 998 cm^{-1} ($\nu_{CC} + \delta_{CH}$) peak of thiophenol, the 1593 cm^{-1} (ν_{CC}) band of MMC, and the 1372 cm^{-1} δ_{CH} signal of thiram. The probes were first measured in isolated configuration, repeating the procedure by moving them and changing then regaining focus (with different operators as before to take this source of variability into account), then spectra were acquired in gap mode with different setpoints (again removing them and regaining focus for each repetition), then the same procedure was applied in light contact mode on the apices of the pyramids of the tipped substrate to produce tip dimers and repeated changing sampled pyramid and reattaining optical focus.

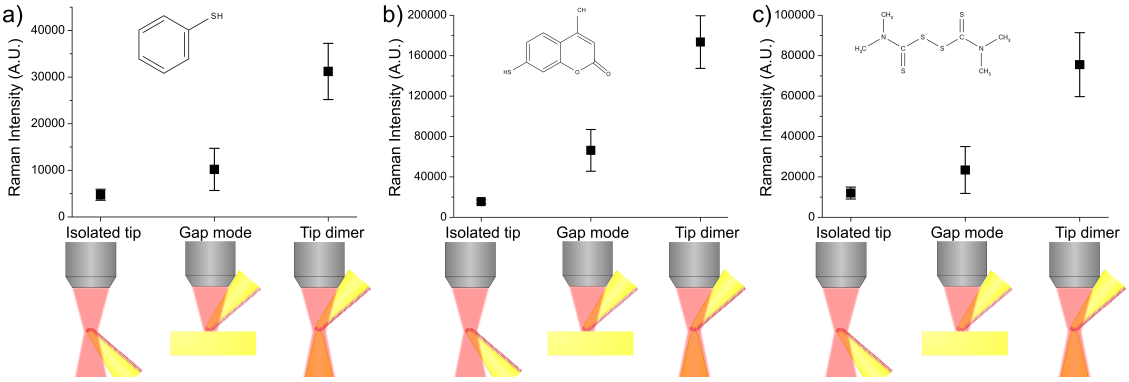

Figure 6.7: Comparison of TERS intensities in the three configurations analysed in this study. (a): thiophenol. (b): 7-mercapto-4-methylcoumarin. (c): thiram. Each data point is the average of the intensities of a Raman band (998 cm^{-1} for thiophenol, 1593 cm^{-1} for MMC, 1372 cm^{-1} for thiram) from measurements on different tips, while error bars represent the standard deviations of the distributions. Note that the reported intensities are comparable among the graphs.

It was found that, when the tips were approached to the top of the pyramids achieving the tip dimer configuration, the TERS spectra of each molecule were systematically much more intense than those arising from both the isolated apices and the same tips approached on flat gold surfaces; approaches on the 20 nm gold layers produced with electron-beam physical vapour deposition described in section 5.2 and the flat areas in the tipped substrate resulted in comparable amplitudes between each other. Specifically, tip dimers generated TERS intensities 2–3 times higher than gap mode, which in turn amplified the signal with respect to the isolated nanoparticles by roughly the same factor.

6.3 Accurate measurement of Raman confocal volume

In order to accurately calculate the enhancement factor of SERS or TERS, formula 5.3 and derived expressions require the acquisition of a non-amplified Raman spectrum and knowledge of the amount of substance from which the Raman intensity arises. This is often dependent on the volume of excitation and collection, which in turn derives from the parameters of the Raman microscope, such as the possible confocality aperture, the objective employed, and the properties of the laser beam passing through it. Although both the laser spot while focussed (beam waist) and the focal depth could be theoretically predicted, non-ideality or simply

lack of knowledge of some of the factors, dielectric function of the medium, as well as imperfect alignment or focus, contribute to inaccuracy and/or low precision in the calculation of the focal volume.

In this thesis, methods for the direct measurement of the acquisition volume of a Raman microscope, i.e. the volume investigated by the laser, from which the non-enhanced Raman radiation is acquired, were devised and employed, since it is an important factor in the calculation of the enhancement factor of TERS. The concept behind both procedures is the use of a strongly active, ideally point-like Raman scatterer to probe the focal volume: its small dimension is needed to avoid broadening of the measured volume due to convolution of the dimensions of the probe and the measurand, and consequently its Raman cross section should be high because of the low amount of substance to be employed, in order to carry out the operations in reasonable time and with acceptable signal to noise ratios.

A single, Raman-enhancing nanoparticle functionalised with an analyte molecule, such as a SERS nanosphere or a TERS isolated tip (like the ones analysed in section 6.1) covered in an organic monolayer was considered for these measurements. While this arrangement would yield quite detectable Raman signals, plasmon-enhanced Raman is not suitable for this task, because of the dependence of its intensity on excitation polarisation direction, which is not uniform around the beam waist, and for its non-linear response to radiation intensity (as discussed in chapter 1).

Because of the difficulty in identifying a point-like candidate material for this purpose, in this thesis the probing process was divided into two separate procedures: one for the measurement of the focal depth, and the other for mapping the planar section of the volume (orthogonal to the depth direction), which was conducted at the beam waist. This course of action was suggested by the cylindrical symmetry of an ideal confocal microscopy apparatus, which exhibits a Gaussian power density profile in the usual case of the output of most lasers (single TEM_{00} mode). Acquiring these profiles allowed the characterisation of the confocal volume, as it could be approximated by an ellipsoid, given the definition of intensity thresholds [94], whose volume is elementarily calculable given its axes. It is noteworthy that while the two probing operations are separate and based on somewhat different concepts, they could be combined into a single three-dimensional scan, which would have the advantage of allowing a complete mapping of the volume, foregoing the geometrical assumption and calculation employed in the present work.

Carbon-based, highly reproducible nanostructures such as graphene and single-walled carbon nanotubes (SWCNTs) are excellent candidates for such procedures, as they are extremely small in at least one dimension. However, SWCNTs have the definite disadvantage of requiring specific protocols for their deposition and immobilisation on a surface. Even then, isolated SWCNTs are invisible with standard optical microscopy, and should be lying straight, not curved, to act as ideal probes. Furthermore, a single SWCNT results in quite low signal to noise

ratios with the 633 nm excitation wavelength often employed in SERS and TERS (including in this thesis). The choice fell on monolayer graphene in two different geometries for the two probing procedures, described in the following paragraphs.

As every TERS measurement presented in this work was conducted with a 633 nm He-Ne laser, a 100× long working distance microscope objective with 0.7 NA, and a 50 µm diameter circular pinhole confocal aperture of the optical microscopy system, this setup was maintained throughout the following operations. The pertaining sample was placed on the SPM stage of the TERS system and moved with the piezoelectric stage controlled with its capacitive sensors for the scans, and of course no SPM probe was mounted during these acquisitions.

Depth profile. The vertical direction of the microscope, depth, which is parallel to the optical axis, was analysed by employing a solid, flat monolayer graphene sheet. Graphene is among the most suitable materials conceivable for this purpose. As an allotropic form of carbon consisting in a two-dimensional hexagonal lattice of ordered sp^2-bonded carbon atoms with high thermal conductivity, chemical stability, and mechanical resistance, a flat monolayer graphene sheet has the smallest possible dimension of a single atom in the vertical direction, hence has the potential of being most performing in terms of spatial resolution. This property, combined with its very high Raman cross section and the possibility of easily obtaining, manipulating and locating samples with areas considerably larger than the focussed laser spot size, makes it an ideal candidate for this analysis.

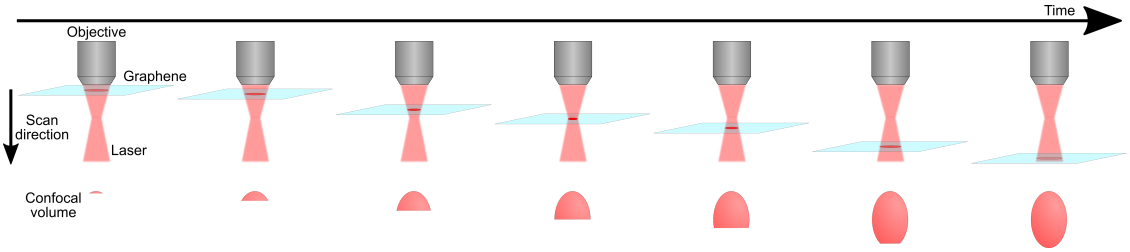

Figure 6.8: Scheme of the measurement of the depth profile of the Raman microscope with a graphene sheet. Several steps are shown as a temporal sequence (left to right). Top row: scheme of the apparatus. Bottom row: geometrical depiction of measured intensities assuming a circular laser spot.

The procedure for profiling the depth of the Raman microscope is straightforward, and is carried out as follows. After placing the sheet under the microscope, oriented orthogonally to the depth direction, and choosing a suitable zone of graphene (continuous, without visible imperfections or contaminations), a Raman

spectrum of the material is acquired to achieve optical focus by maximising the signal. It is important to limit the power density at the sample at all times, choosing an appropriate laser power according to the objective, in order not to cause heat damage to the graphene. For these measurements, laser power at the sample never exceeded 1.0 mW. The acquisition parameters are then optimised: a signal to noise ratio of at least 10–20 for the chosen Raman band should be obtained, depending on the selected intensity threshold for the definition of the focal volume. In this study the 2D band (2690 cm^{-1} corresponding to double-phonon scattering) was considered, since for single-layer graphene its intensity is higher and in general it is less dependent on the number of layers than the other prominent peak in a non-defective lattice, which is the G band. The stage is then moved out of focus in the depth direction until the Raman intensity falls below the threshold, then arbitrarily further to create margin. At this point the probing starts, consisting in the acquisition of spectra at regular intervals while the stage is scanned along the vertical direction towards the focus point and beyond. The scan finishes some steps after the point in which the intensity reaches the threshold again.

In this work, this procedure was repeated several times removing and placing again the graphene sample each time, over several sessions, to achieve independent measurements. Five scans with step sizes of 100 nm and 200 nm are reported. The employed sample was commercial monolayer graphene, bought from Graphene Laboratories Inc. [95], created by chemical vapour deposition and transferred on quartz [96–98]. A transparent support for the graphene was chosen since a reflective surface was deemed less suitable for an accurate measurement, as considerable reflection was thought to affect the results. Indeed, the best condition would be the adoption of a flat, suspended graphene monolayer. This was also sought in this work with graphene transfer from copper foil on a holed monocrystalline silicon substrate, but preliminary tests on the manufactured samples had shown low reproducibility of the measurements, probably because of reflections of the laser by the walls of the holes, and possibly because of a degree of curvature of the areas of the graphene sheet suspended on the wells.

The intensity of the 2D Raman band was calculated by considering for each spectrum, after linear baseline subtraction, the area under the Lorentzian regression curve. In order to compare scans, each run was normalised to 1 by the intensity of the best focussed spectrum. The results of five independent scans are presented in figure 6.9. Assuming a Gaussian profile of the depth of the confocal volume [94], the information relevant to the dimension of the focal volume is the Gaussian curve width parameter σ, corresponding to half of the curve width at $\frac{1}{e}$ times its maximum, from which the total width of the curve can be calculated as 2σ. The values of 2σ for the aforementioned five scans singularly best fitted are reported in table 6.2, along with the average and standard deviation of the sample distribution.

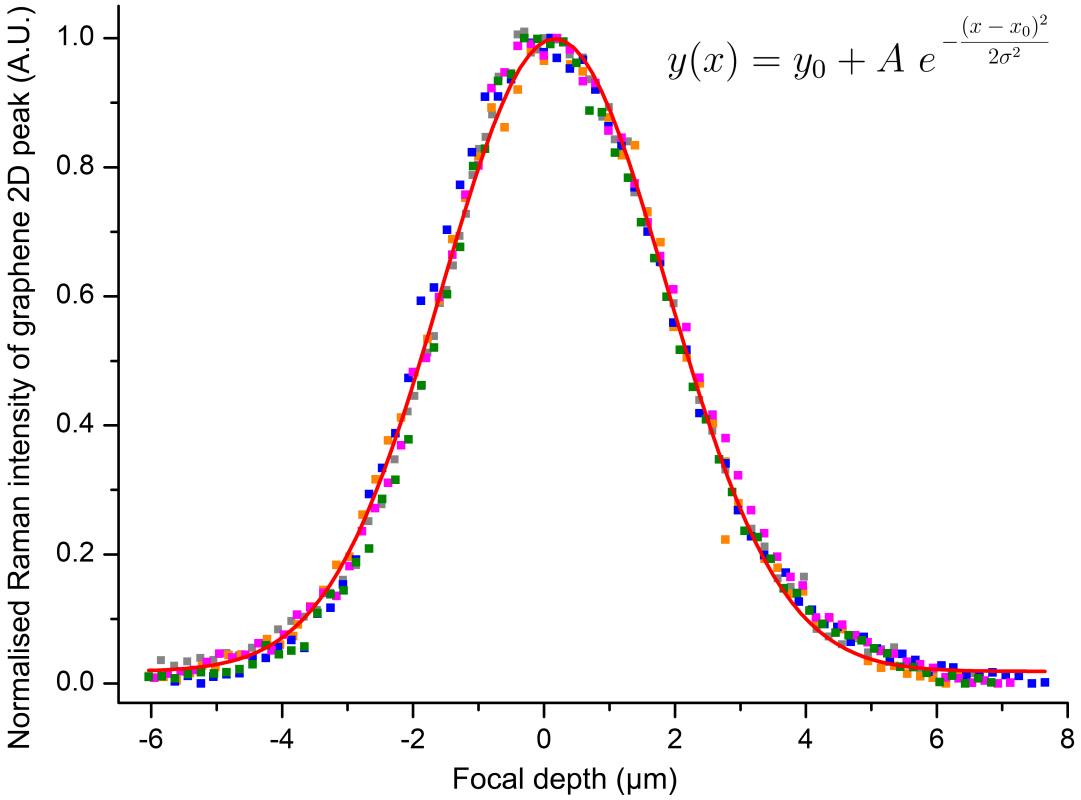

Figure 6.9: Scatter plots of five independent scans of the vertical profile (depth, along the optical axis) of the confocal volume of the Raman microscope of the DXR™-Ntegra TERS system), probed with a graphene monolayer. Each scan is represented with a different colour and it is independently normalised to 1. A Gaussian regression of the whole dataset is superimposed (line in red): the equation in reported in black (y is the intensity, x the scan direction, y_0, x_0 are offsets). The fit on all five scans yielded a curve of width $2\sigma = 3.56$.

Planar profile. A traditional practice for the measurement of the radius of a laser spot and for the characterisation of Gaussian beams is the knife-edge method [99, 100]. To conduct this procedure, a power meter is placed in the laser path while a completely opaque object with a straight edge, the knife, is scanned in a direction orthogonal to the optical path to gradually block the beam, while the intensity of the transmitted light is monitored as a function of its maximum, when the knife-edge is absent. The positions of the knife which cause the intensity of the laser to reach set thresholds define the lateral limits of the beam in the scan direction. In the hypothesis of cylindrical symmetry around the optical axis, a

Scan number	Gaussian regression 2σ (µm)
#1	3.46
#2	3.68
#3	3.46
#4	3.76
#5	3.52
Average	3.58
Standard deviation	0.14

Table 6.2: Width of the Gaussian curve fit (2σ) of five depth profiles of the confocal volume of the TERS system Raman microscope probed with a graphene monolayer.

single measurement is sufficient to define the beam waist; alternatively, the same process can be carried out again in the planar direction orthogonal to the first to identify asymmetries.

A similar concept can be applied to a Raman microscope near its focus point, by utilising the measured Raman intensity of a sample uniformly distributed in the focus plane and gradually covering it with a knife edge. A less complicated but effectively equivalent arrangement conceived for this thesis consists in the employment of an appropriately manufactured surface, presenting two half-planes with different uniform compounds with a straight, sharp interface. An example of this configuration is the edge of graphene flakes (if not jagged or curved). By scanning a straight graphene edge through the microscope focus point in the same way as the opaque object used in the knife-edge method, the laser spot profile can be mapped by monitoring its Raman intensity.

Figure 6.10 shows a schematic representation of the probing procedure. This practice is comparable to the depth scan introduced earlier, with the notable difference that the intensity at any given position of the analyte does not arise from a small portion of the volume with respect to the scan direction, investigating a segment of the profile at each acquisition, but the laser spot is increasingly occupied by the graphene surface instead, generating an intensity profile I which is monotonously growing, being the integral of the profile. This behaviour as a function of the lateral position is, for a Gaussian beam, equal to the integral of the Gaussian profile with respect to the focal plane surface xy, limited by the graphene area filling the laser spot Σ:

$$I(\Sigma) = \iint_{\Sigma} \frac{1}{\sqrt{2\pi\sigma_x^2}} \frac{1}{\sqrt{2\pi\sigma_y^2}} \exp\left[-\left(\frac{(x-\mu_x)^2}{2\sigma_x^2} + \frac{(y-\mu_y)^2}{2\sigma_y^2}\right)\right] dx\ dy \tag{6.1}$$

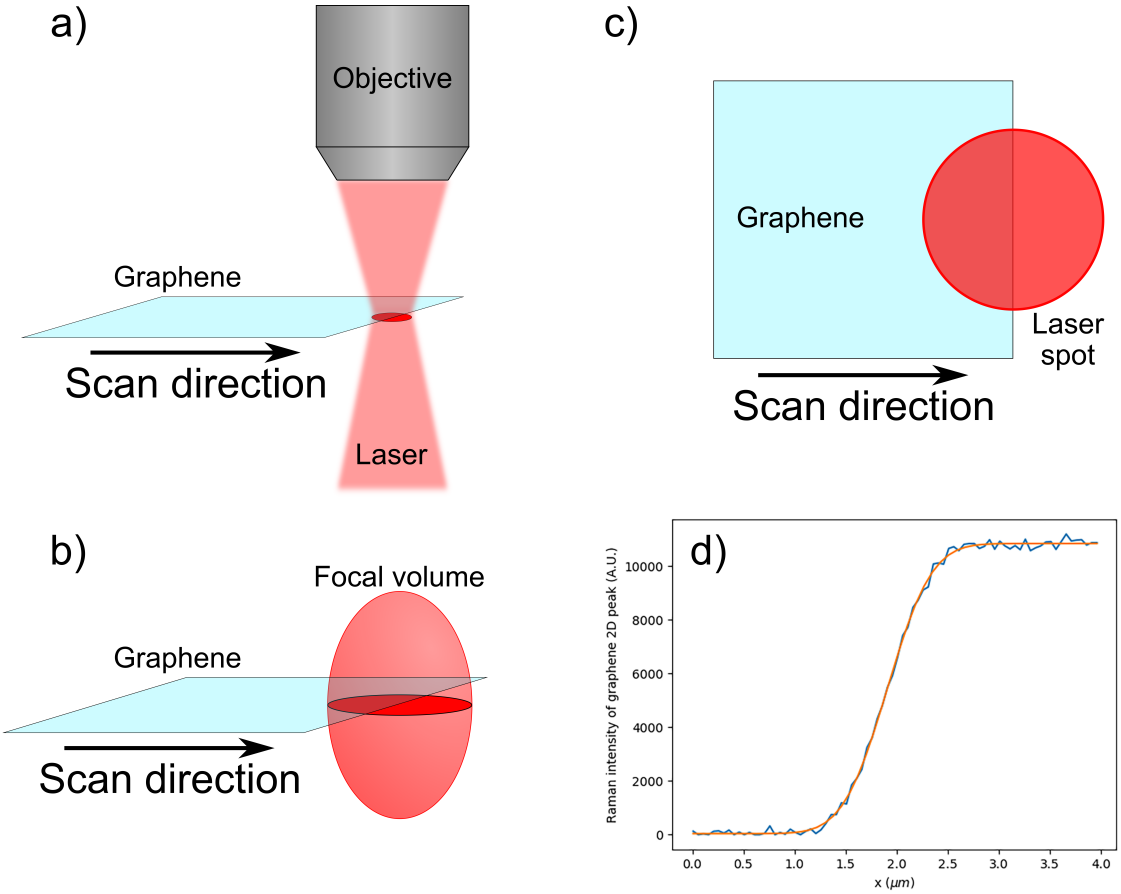

Figure 6.10: Schemes of the measurement of the lateral profile of the Raman microscope by graphene edge probing. A graphene sheet with a straight edge was laterally scanned in the focal volume of the microscope, at the focus plane. Starting this from a position out of the beam, the Raman intensity of the graphene follows a Gaussian error function trend, from which the Gaussian profile can be inferred. (a): perspectival view of the apparatus during the probing procedure. (b): perspectival view of the ellipsoidal confocal volume during scanning. (c): planar view of the laser spot probed by graphene. (d): experimental data (blue line) and Gaussian error function best fit (orange line) of the 2D Raman peak of graphene as a result of a scan along the x axis.

where (μ_x, μ_y) is the coordinate of the centre of the beam spot, and σ_x and σ_y are the width parameters of the Gaussian profiles in the x and y directions respectively. In this equation, the integral is normalised to 1. This expression is equal, for a half-plane of graphene with a geometrically straight edge, to a one-dimensional Gaussian integral in the scan direction x ranging from $-\infty$ to the lateral position x_0 of the graphene edge, in the hypothesis that the setup consists in a half-plane $x < x_0$ fully

occupied by uniform graphene and $x > x_0$ containing no graphene material:

$$\begin{aligned} I(x_0) &= \frac{1}{2\pi\sqrt{\sigma_x^2\sigma_y^2}} \int_{-\infty}^{+\infty} \exp\left[-\frac{(y-\mu_y)^2}{2\sigma_y^2}\right] dy \int_{-\infty}^{x_0} \exp\left[-\frac{(x-\mu_x)^2}{2\sigma_x^2}\right] dx = \\ &= \frac{1}{\sqrt{2\pi\sigma_x^2}} \int_{-\infty}^{x_0} \exp\left[-\frac{(x-\mu_x)^2}{2\sigma_x^2}\right] dx = \Phi\left(\frac{x_0-\mu_x}{\sigma_x}\right) \end{aligned} \tag{6.2}$$

which is the cumulative Gaussian distribution function $\Phi(t)$, a sigmoid curve closely related to the Gaussian error function $\mathrm{erf}(t)$. This function represents the integral of a Gaussian function as a function of the integration interval:

$$\begin{aligned} \Phi\left(\frac{x-\mu}{\sigma}\right) &= \frac{1}{\sqrt{2\pi\sigma^2}} \int_{-\infty}^{x} \exp\left[-\frac{(t-\mu)^2}{2\sigma^2}\right] dt = \frac{1}{2}\left[1 + \mathrm{erf}\left(\frac{x-\mu}{\sqrt{2}\sigma}\right)\right] \\ \mathrm{erf}(t) &= \frac{2}{\sqrt{\pi}} \int_0^t e^{-x^2}\, dx \end{aligned} \tag{6.3}$$

where $\mathrm{erf}(t)$ is defined for a Gaussian distribution centred at $\mu = 0$ and with width parameter $\sigma = \frac{1}{2}$.

In this instance, the final expression should have, for an analysis of non-normalised Raman peaks with background subtraction, a co-domain limited to the interval $(0; I_{max})$, where I_{max} is the maximal Raman intensity of the graphene during the scan, achieved when the laser spot is fully occupied by the analyte. From the Raman peak intensity of graphene as a function of the scan position and error function regression of these data, it is possible to achieve a value for the width σ of the Gaussian profile from which $\Phi(t)$ and $\mathrm{erf}(t)$ derive, therefore the size of the laser spot. This procedure can be executed in one, two or more directions. There is a criticality in the operation: the graphene edge should be placed as perpendicularly as possible with respect to the scan direction. Failure to achieve this would result in a measurement bias of the width parameter equal to a factor $\left(\frac{1}{\cos\theta} - 1\right)$, where θ is the offset angle from the orthogonality condition of the edge with respect to the scan axis. While this factor is negligible for $\theta \sim 0$, it becomes influential for larger angles.

In this thesis, two orthogonal directions along the focus plane were investigated with the graphene edge method, labelled x (horizontal) and y (vertical). The operating procedure was conducted as follows. Commercial monolayer graphene produced by chemical vapour deposition (equivalent to the one utilised in the focal depth measurement) transferred to a wafer of 280 nm SiO_2 on monocrystalline silicon was employed. The optical contrast of mono- and few-layer graphene on this support allows clear localisation of suitable flakes, and identification of large areas of monolayer graphene without the need of time-consuming Raman maps [101]. After choosing an appropriate area, a semi-contact AFM map was conducted on the flake to verify the straightness of the edge, visible in figure 6.11. Note that for best

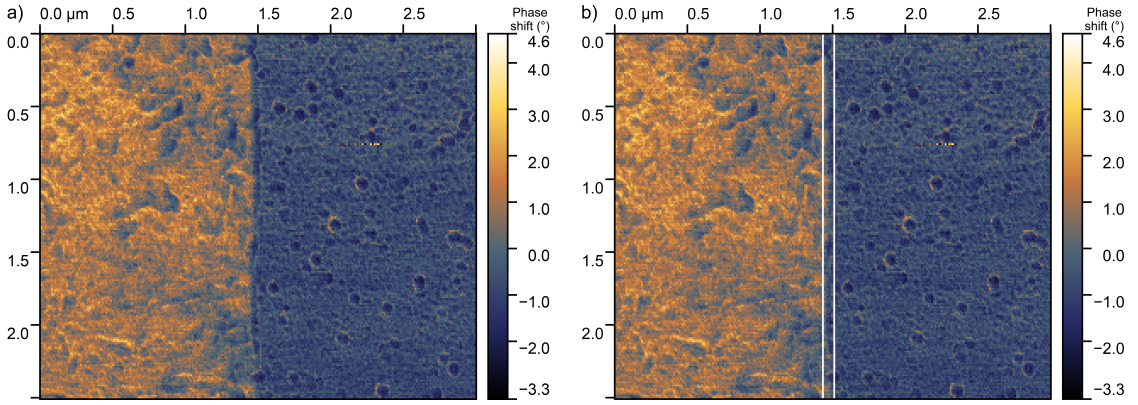

Figure 6.11: (a): semi-contact AFM image (phase) of the graphene edge employed for the planar probing of the focal depth. (b): the same image with white marker lines indicating the limits of the jagged graphene edge in the scan direction. The distance between the lines is 10 nm.

precision of this method, an edge as straight as possible is needed, as its jaggedness influences the measurement. For example, the profile of the edge of the flake employed in this study deviated from its median vertical line by ±5 nm, affecting the profile. To reduce uncertainty even more, another production method for the graphene flake edge, such as nanopatterning by AFM lithography, focussed ion milling, masking and selective covering of the sheet via electron beam lithography and evaporation, or electron-beam-initiated mechanical rupture/tearing in high vacuum [102], might be a more performing solution, although less practical.

The substrate was rotated in order to achieve orthogonality of the edge with the desired scan direction. Several line measurements along the axis were then performed, in the form of a Raman map whose fast raster scan direction was the axis to be characterised. The choice of the scanning zone is arbitrary: for a reliable regression, lines centred on the graphene edge were chosen which were at least three times larger than the estimated spot size. As there were four fit parameters to be extracted for each line (graphene edge position and centre of the error function μ, width parameter σ, maximum intensity I_{max} and baseline offset I_{min}), an ample number of line points including areas further from the edge resulted in a better estimation[1] of σ. Areas of $3{\times}2$ µm^2 were chosen, for repeated scan lines 3 µm long. Each data point was calculated by integration of the Lorentzian regression of the 2D Raman peak after baseline subtraction, as the focal depth profiling presented earlier.

[1]In terms of reduced χ^2 obviously, but also judging by the reduced dispersion of data on σ, and by comparing the fit results to estimations on the same data achieved by selection of the positions of the intensities corresponding to σ as well.

x axis Gaussian curve width $2\sigma_x$		y axis Gaussian curve width $2\sigma_y$	
Parameter	Value (µm)	Parameter	Value (µm)
Average	0.65	Average	0.67
Standard deviation	0.04	Standard deviation	0.03

Table 6.3: Gaussian curve widths (2σ) of the planar profiles of the confocal volume of the Raman microscope probed with a graphene monolayer straight edge, measured along two orthogonal axes. 40 lines of Raman spectra were acquired in each direction and best fitted with Gaussian error functions. These data are based on the 2D peak of graphene.

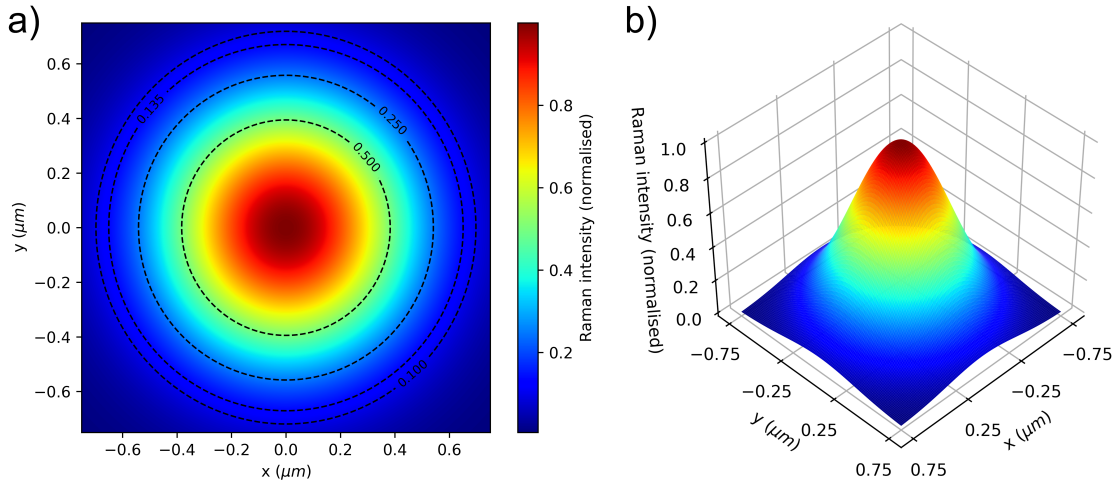

Figure 6.12: Reconstruction of the laser spot intensity from planar probing data of 2D Raman peak with the graphene edge method assuming an ideal Gaussian profile. (a): 2D intensity plot with lines indicating common intensity thresholds for the definition of the spot size. (b): 3D view of (a).

40 lines were measured in each direction for this study. For each line, a Gaussian error function regression taking into account the four aforementioned parameters was made, and a width parameter σ was extracted. The average curve width 2σ and the standard deviation on the distribution was calculated for each line: they are reported for the two directions in table 6.3. Assuming Gaussian profiles, the mapped laser spot profile of the Raman microscope could be reconstructed, whose intensity image as a function of position is shown in figure 6.12.

From these data, a laser spot area value can be easily obtained which, combined with the depth width, allows the calculation of the confocal volume of the microscope.

Confocal volume definition and calculation. After the measurement of the width parameters for the Gaussian profiles for depth and two planar directions, the confocal volume of the microscope employed for TERS measurements can be defined, in order to quantify the amount of substance measured by non-amplified Raman (N_{Raman} in equation 6.5) to accurately determine the EF. The definition of the focal volume, as well as that of the laser spot size, is somewhat arbitrary, as the Gaussian profile does not have clear boundaries. For this reason, a threshold must be defined in order to limit the volume to a certain size according to a parameter (e.g. the volume containing a certain percentage of total radiation intensity). The threshold can be sought either on its intensity or its integral. In table 6.4, a few parameters which can be chosen to set a limit to its dimensions are reported, along with the resulting dimensions of the focal volume measured in this thesis for these values. Uncertainties on the width parameters were calculated from the standard deviations of the repeated measurements (coverage factor $k = 1.96$).

The most common threshold for beam width is $\frac{1}{e^2}$ of the maximum intensity [100, 103, 104], corresponding to a width limited by 2σ for each axis and in each sense. Choosing this limit, the total confocal volume of the Raman microscope of the TERS apparatus could be calculated, and was found to be (6.5 ± 0.5) µm^3.

It is worth noting that the depth scanning and the graphene edge planar profiling can be combined. By performing the graphene edge scanning at different depths of the volume, the same information on the three dimensions as the separate

Height	Width	Area	Δx (µm)	Δy (µm)	Δz (µm)
10%	2.14 σ	96.8%	1.39 ± 0.09	1.43 ± 0.06	7.7 ± 0.3
13.5% $\left(\frac{1}{e^2}\right)$	2 σ	95.45%	1.30 ± 0.08	1.34 ± 0.06	7.2 ± 0.3
26%	1.65 σ	90.0%	1.07 ± 0.07	1.11 ± 0.05	5.9 ± 0.2
32.7%	1.495 σ	86.5% $\left(1 - \frac{1}{e^2}\right)$	0.97 ± 0.06	1.00 ± 0.04	5.4 ± 0.2

Table 6.4: Parameters of a Gaussian profile, possible thresholds for confocal volume determination (fraction of maximum height, width from the centre, area under the curve), and consequent dimensions of the volume (Δx, Δy, Δz) by choosing them as intensity limits.

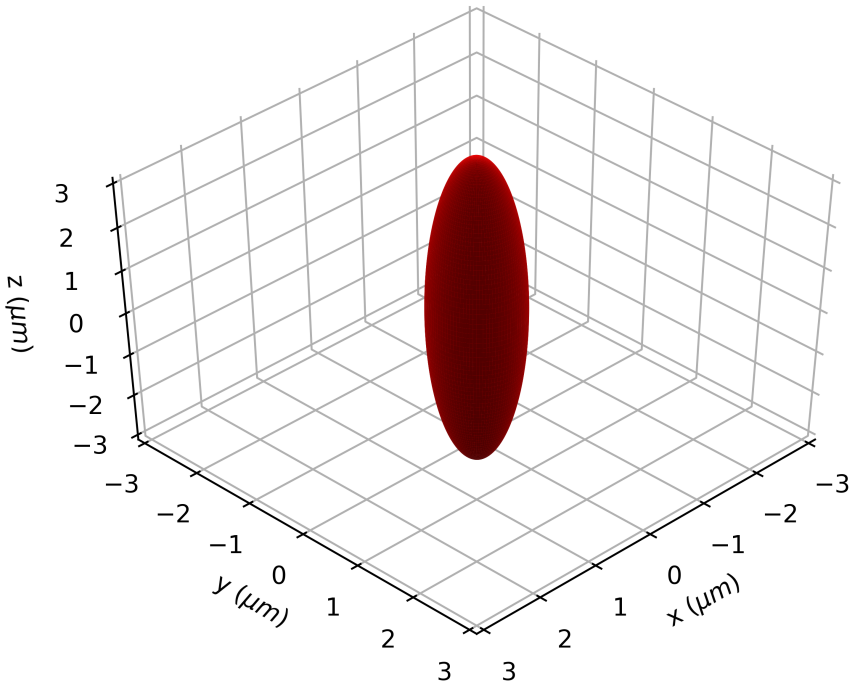

Figure 6.13: Reconstruction of the confocal volume of the Raman microscope. The limit was set by employing a threshold on intensity of $\frac{1}{e^2}$, corresponding to two times the width parameters of the Gaussian profiles along each of the Cartesian axes in both senses.

procedures can be attained, with the great advantage of acquiring an actual three-dimensional image of the volume without the need of assuming Gaussian profiles and an ellipsoidal shape. [94, 100–107]

6.4 Accurate calculation of the enhancement factor in TERS

Enhanced Raman intensity values can be meaningful by themselves for comparing closely related systems in the same environment, such as those shown in figure 6.7, in which nanoparticle configurations can be correlated since the acquisitions were performed by analysing the same amount of substance with the same experimental parameters. In the study, in fact, measurements were accomplished by means of employing the same probes consequently in each configuration and with the same spectral parameters (i.e. factors that influence spectra, such as objective, excitation power, and collection time). However, the simple intensity analysis

approach is impracticable when studying and comparing probes with different geometries or different molecules, as well as when changing experimental apparatus or conditions, and in general in the majority of cases involving variations in setup aspects. The concept of enhancement factor (EF) solves this comparability issue by rationalising the TERS (or SERS) intensity by its non-amplified counterpart in the same conditions, and normalising this value by the number of involved molecules in each case.

The accurate calculation of EFs is often difficult or downright impossible with a simple application of its formula, already reported as equation 5.3:

$$EF = \frac{I_{tip\ in} - I_{tip\ out}}{I_{tip\ out}} \frac{N_{FF}}{N_{NF}} \tag{6.4}$$

where $I_{tip\ in}$ is the intensity of the considered spectral features registered with the probe approached to the surface, and $I_{tip\ out}$ is the intensity of the same signals with the tip retracted in the same experimental conditions, while N_{NF} and N_{FF} are the amount of substance generating the TERS signal and excited during non-amplified Raman respectively. Note that this is an average enhancement factor, as the LFIEF is not constant throughout the hotspot. To broaden the scope of application of this discussion to include SERS as well, equation 6.4 can be rewritten as:

$$EF = \frac{I_{ERS}}{I_{Raman}} \frac{N_{Raman}}{N_{ERS}} \tag{6.5}$$

in which I_{ERS} is the portion of Raman intensity of the signal corresponding to the vibration taken into consideration generated by the enhanced Raman (ERS, be it TERS or SERS) effect (after deducting the non-enhanced Raman contribution to the spectrum, although this last element is usually very small and could be ignored as an approximation when subtracted from I_{ERS}), I_{Raman} is the Raman intensity arising from the unaided Raman effect with the same spectral parameters, while N_{Raman} and N_{ERS} are the numbers of molecules involved in the non-enhanced and plasmon-enhanced Raman effects respectively.

The impracticability of applying this equation to formally calculate the EF arises from the estimation of several of its parameters. While obtaining I_{ERS} is a matter of uncomplicated spectral analysis, the evaluation of the amount of substance in standard Raman and ERS is not straightforward in most cases. In fact, both are dependent on the probed volume and the investigated substance and its spatial distribution. Even in the case of homogeneous bulk substances, such as solutions, crystals or other highly ordered structures, in which case equation 6.5 becomes:

$$EF = \frac{I_{ERS}}{I_{Raman}} \frac{c_{Raman}\ V_{Raman}}{c_{ERS}\ V_{ERS}} \tag{6.6}$$

where c_{ERS} and c_{Raman} are the concentrations or densities of the analyte in the acqusition of the ERS and Raman spectra respectively, and V_{ERS} and V_{Raman} are the volumes of space investigated by enhanced Raman (i.e. the hotspot volume)

and by Raman (for example the focal volume in the case of transparent samples) respectively, the employment of the formula requires characterisation of these latter two parameters. A method for the direct measurement of V_{Raman} was introduced in section 6.3, which requires nanomaterials to probe the focal volume, resulting in its three-dimensional imaging. The same concept could be applied to obtain information on the dimensions of the hotspot, although usually finite element methods of numerical simulation or approximations based on the morphology of the tip are employed.

The most impeding limitation on the formal calculation of the EF is due to the magnitude of the enhancement factors involved in most TERS and SERS processes, hence the great difference between the optimal conditions for plasmon-enhanced Raman spectroscopy and those for non-enhanced Raman scattering: the former often preclude detection of non-amplified Raman signals, while the latter are usually too intense for ERS. Since I_{ERS} and I_{Raman} must be acquired at the same conditions for the formula to stand, it is often the case that I_{Raman} is zero, such as in the study reported in section 5.3 of this work. In order to assess the EF in such instances, a method for the estimation of an accurate I_{Raman} was developed in this thesis.

The procedure involves two steps, and the preparation of a solution of the analyte molecule in a transparent solvent with a high non-enhanced Raman cross-section. The concentration of the solution is arbitrary, but it should abide by two conditions: it must be high enough for the analyte to be detected in liquid with the Raman spectrometer, and the resulting liquid should have low absorption in the spectral region of the excitation laser and the considered Raman band. After the preparation of the solution, a non-amplified Raman measurement is made inside the solution (i.e. the whole focal volume should be inside the liquid) with the same spectral conditions as the amplified TERS or SERS spectrum from which I_{ERS} is acquired (henceforth referred to as enhanced Raman conditions, or ERC). Note that a spectrum registered in ERC would not usually yield any signal by the analyte molecule dissolved in the solution[2], since ERC are characterised by quite low excitation power and exposure time, but, for this method to be applicable, the resulting spectrum should show at least one peak ascribable to the solvent. Another spectrum of the solution must be acquired with a suitable setup for the detection of the analyte signal involved in the calculation of the EF (non-amplified Raman conditions, RC).

[2]If a notable intensity of the target Raman peak of the molecule is detected instead, the procedure can end at this step simply by employing this value as I_{Raman}, the solution concentration as c_{Raman}, and the focal volume as V_{Raman}.

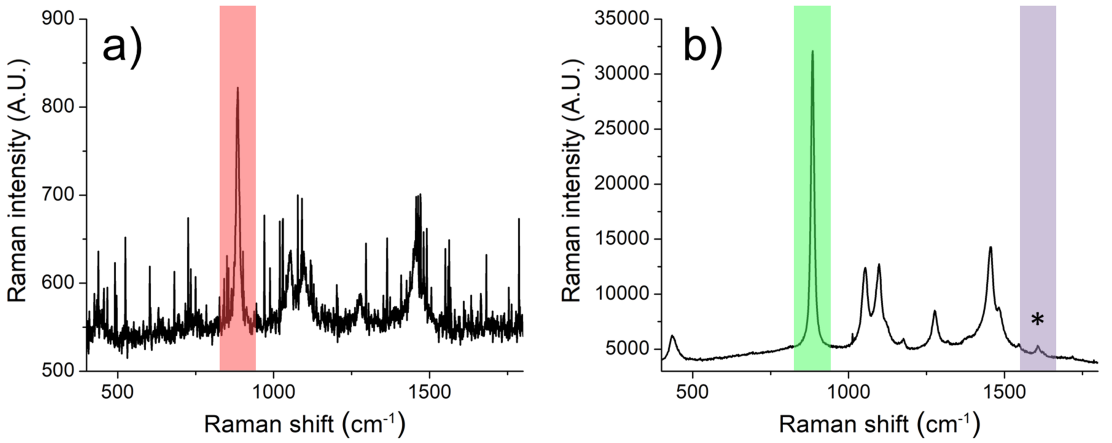

c)

$$I_{Raman} = I_{ERC}(analyte) = \frac{I_{RC}(analyte)}{I_{RC}(solvent)} I_{ERC}(solvent)$$

Figure 6.14: Method for the estimation of undetectable non-amplified Raman signals for the calculation of the enhancement factor, involving the collection of two spectra of a solution of the analyte investigated with enhanced Raman spectroscopy, here applied for MMC in ethanol as an example. (a): the solution is measured with the conditions employed for enhanced Raman spectroscopy (ERC, in this case 1.5 mW laser power, 60 s integration time). No MMC is detectable, but some ethanol peaks are visible. The intensity of the band highlighted in red is calculated. (b): another spectrum of the solution is acquired, with a setup and conditions suitable for non-amplified Raman (RC, in this case a special cell with 8 mW excitation power and a 300 s exposure), optimised to detect the target band of the analyte (highlighted in blue and marked with an asterisk). Intensities of the band of the analyte measured in (a) and the solvent signal taken into consideration (in green) are calculated. (c): the proportion (equation 6.7, whose factors are highlighted in figure with colours corresponding to the peaks in the spectra) is computed to evaluate the equivalent signal intensity of the analyte in ERC. Reprinted with permission from [61]. Copyright 2019 American Chemical Society.

Utilising the Raman-active solvent as an internal standard, an estimation of the equivalent Raman intensity of the analyte in ERC can be assessed with the following proportion:

$$I_{Raman} = I_{ERC}(analyte) = \frac{I_{RC}(analyte)}{I_{RC}(solvent)} I_{ERC}(solvent) \tag{6.7}$$

in which I_{ERC} and I_{RC} are the intensities, in ERC and RC respectively, of the chosen signal of either the solvent or the analyte, in parentheses. The result of this proportion, $I_{ERC}(analyte)$, is then a reasonable value for I_{Raman} in equation 6.6 and related formulae when the focal volume is employed as V_{Raman}. Figure 6.14 shows examples of the two steps of the procedure as well as equation 6.7 with visualisation aids.

The approaches presented in this section and section 6.3 to estimate the parameters involved in equation 6.6 were employed in this thesis to calculate the enhancement factor generated by the AFM-TERS probes in the study introduced in section 6.2 on the analysed molecules in the three configurations. Self-assembled monolayers, in fact, simplify the estimation of the amount of substance needed for the EF: employing SAMs and the aforementioned two-step method with solutions to acquire I_{Raman}, formula 6.6 becomes:

$$EF = \frac{I_{ERS}}{I_{Raman}} \frac{c_{Raman}\, V_{Raman}}{C_{ERS}\, A_{ERS}} \tag{6.8}$$

where C_{ERS} is the surface concentration of the SAM, and A_{ERS} is the area of the SAM investigated by the hotspot. Since in this particular study the SAMs were not chemisorbed on a flat surface but on the gold tips, the common TERS approximation of the hotspot area as a circle with radius equal to the curvature radius of the tip was adapted to consider the area of the surface of a spherical dome with radius equal to the average curvature radius of the tips (estimated by scanning electron microscopy), with the diameter of the base of the dome equal to the output of finite element simulations found in literature on nanoparticles of sizes ascribable to those of the tips employed in this study [4]. Surface concentrations of the thiophenol and thiram SAMs were sourced in literature [73, 76–78], while C_{ERS} for MMC was estimated relying on the molecule volume, an approach that was verified to be quite effective with thiophenol, producing a very similar result to the measured value found in literature.

The analysed Raman signals of the three molecules were the 998 cm^{-1} ($\nu_{CC} + \delta_{CH}$) peak of thiophenol, the 1593 cm^{-1} (ν_{CC}) band of MMC, and the 1372 cm^{-1} δ_{CH} signal of thiram. The solutions employed for the estimation of I_{Raman} with the method introduced above were the following: thiophenol 33 mM in ethanol, 1 mM MMC in ethanol, and thiram 0.62 M in chloroform. Enhanced Raman conditions were 1.5 mW laser power with a single acquisition with a duration of 60 s, as already stated in section 6.2. The setup for the detection of the RC signals was a concave mirror cuvette holder, in which a quartz cuvette filled with the solution was placed for each acquisition, with 8 mW laser power and 300 s acquisition time. The Raman bands of the solvents employed as internal standards were the 882 cm^{-1} signal of ethanol, and the 262 cm^{-1} peak of chloroform.

Figure 6.15 shows a graph summarising the values of the EFs calculated for the three molecules in the three configurations explored in section 6.2, calculated with their uncertainties, along with a sample TERS spectrum for each combination of the two. The results of the EF study are also reported numerically in table 6.5.

It is worth mentioning that these EF values are descriptive only of the specific Raman peaks analysed: different molecular vibrational modes may have distinct TERS/SERS enhancements, as the cross section of the Raman signal correspondent to each vibration is dependent on the direction of the change in polarisability of the molecule with respect to the excitation polarisation, which is highly directional in plasmon-enhanced Raman: this may affect the EF values for each vibrational mode, especially when the sample is heavily organised such as in the case of a self-assembled monolayer, with respect to molecules in a powder or solution as in non-amplified Raman, whose spatial orientation direction is null on average because of their disorder and great quantity. For the analytes considered in this study, this is quite evident in the case of thiophenol by examining the peak ratios in TERS and non-enhanced Raman spectra. EFs of different peaks and/or peak ratios may differ when changing apparatus type, probes or excitation wavelength [62].

It is evident by the EF data (as it was comparing the intensities by themselves) that a distinct trend is followed for the three molecules by changing nanoparticle configurations. It was found that gap mode exhibited EFs (2.2 ± 0.4) times higher than the isolated probe on average, while the average ratio between enhancement factors of tip dimers and the isolated probe arrangement was (6.7 ± 0.6).

Configuration	Thiophenol EF	MMC EF	Thiram EF
Isolated tip	$(3.7 \pm 1.2) \times 10^6$	$(1.9 \pm 0.4) \times 10^5$	$(1.8 \pm 0.5) \times 10^8$
Gap mode	$(8 \pm 4) \times 10^6$	$(5 \pm 2) \times 10^5$	$(3.6 \pm 1.9) \times 10^8$
Tip dimer	$(2.5 \pm 0.7) \times 10^7$	$(1.4 \pm 0.3) \times 10^6$	$(1.2 \pm 0.3) \times 10^9$

Table 6.5: Enhancement factor results for the three analytes in the three configurations.

Comparing the EFs of the molecules in each configuration yields radically different results than doing the same with raw intensity data. The principal factor in this is the conventional Raman cross section of the analytes: the 633 nm laser radiation falls into the range of an absorbption band of MMC, leading to resonant Raman and high I_{Raman} values which brought down the EF even though the molecule exhibited the most intense TERS spectra of the three. The study showed that thiram, instead, manifested the highest EFs between the analytes and was found to be an excellent

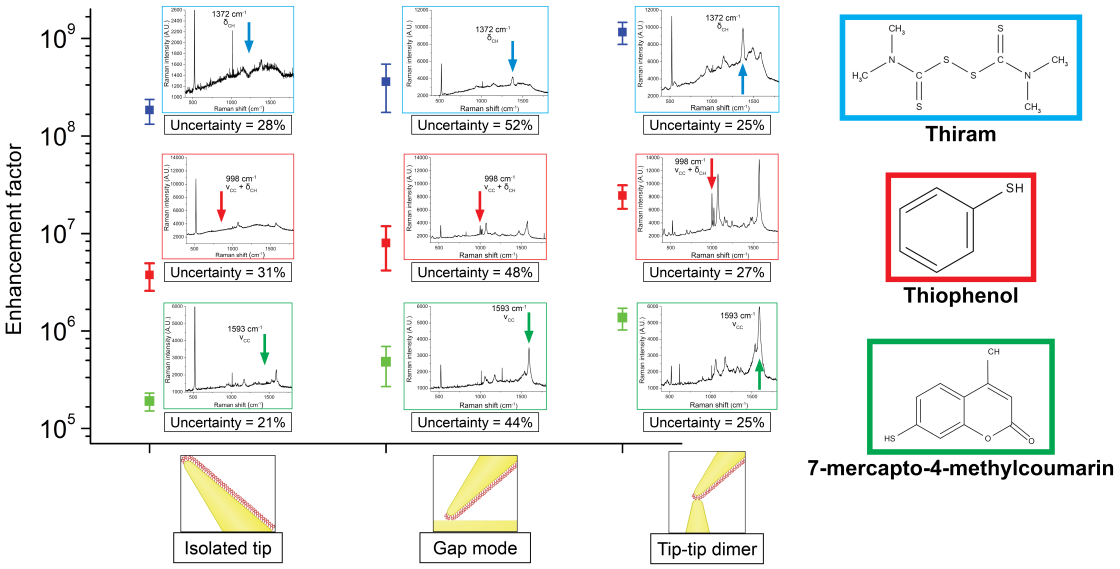

Figure 6.15: Graph of the enhancement factors exhibited by the three analytes employed in this work (thiophenol in red, MMC in green, thiram in blue) in the three nanoparticle configurations studied. Error bars represent uncertainties on the mean values. Insets show examples of spectra for each molecule-arrangement combination; arrows indicate the Raman band taken into consideration for the calculation of the EF for that compound. Reprinted with permission from [61]. Copyright 2019 American Chemical Society.

TERS/SERS probe, performing even better than the de facto standard thiophenol in this scope, paving the way for the employment of this molecule in TERS, and of TERS itself in new real-life applications such as food and agricultural analyses, since thiram is a commonplace pesticide employed in coltures which is regulated by law not to be present in any concentration on most fruits and vegetables destined to human consumption [108], hence whose trace detection is an actual need in industry and distribution. [7, 12, 18, 23, 53, 54, 60–63, 66–79, 90–94, 100–118]

Chapter 7

Conclusions

In this thesis the topic of standardisation in tip-enhanced Raman spectroscopy was discussed. This work was focussed on the ab initio development of procedures for obtaining reproducible TERS tips and data, both spatial images and point spectra, and it aimed to define and explore key concepts widespread in the TERS community, with a particular attention to comparability of measurements.

After a brief discussion on the theoretical bases of plasmon-enhanced Raman spectroscopy and on the fundamental notions of metrology, the subject of in-house production of TERS tips was considered, for employment both in AFM- and STM-based feedbacks. Full silver STM-TERS tips were manufactured by electrochemical etching starting from silver wires and commonplace chemicals. A reaction cell was constructed to achieve this, then improvements to the reproducibility of the tips and their plasmon tuning to the sought optical excitation wavelength were made by devising and assembling an electronic control circuit for the reaction. As a result, TERS-active probes for 633 nm wavelength resonance with average apices curvature radii of (40 $\pm$ 10) nm were obtained, to be utilised in a following study on TERS spatial capabilities.

After this, a surface complementary to SPM calibration samples for TERS chemical imaging was devised, manufactured and measured with the silver STM-tips. The TERS calibration candidate standard was engineered for compatibility with any TERS system, and consisted in a flat, non-enhancing gold surface with patterns of thiol self-assembled monolayers with nanometric features chemisorbed on it. Every step of the manufacturing process was optimised for the task. Starting from flat electron-beam evaporated gold surfaces, whose roughness was characterised and refined to avoid any unwanted SERS enhancement, the samples were produced by electron-beam lithography of PMMA masks deposited on the aforementioned gold foundations. The optimal electron dose interval was sought to obtain suitable masks which were then developed, exposing the gold surfaces on which the thiols could chemisorb. Two thiols were employed: thiophenol, a de facto standard in TERS, and 7-mercapto-4-methylcoumarin (MMC), an unexplored molecule for

TERS which generates TERS intensities higher than thiophenol in these conditions. After the mask lift-off, STM-TERS images on both types of monolayers were carried out on these standards, demonstrating the validity of the sample with thiophenol, and the relative instability of the MMC monolayer. Lower limits of the nanopatterning technique were also explored by employing underdeveloped masks to obtain small features of dimensions <10 nm. A comparison between the spatial capabilities of the topographic and chemical imaging of TERS was also conducted, which, as expected, resulted in a lower resolution of the chemical map, since this is tied to the hotspot volume, which is generally broader than the STM effective probe size.

Gold-covered AFM-TERS probes were developed as well, starting from commercial AFM probes, which were metallised with different quantities of gold by means of a sputtering system. Then, the production was optimised for manufacture probes with plasmon resonance at a wavelength of 633 nm by analysing them with a novel procedure which maximises precision of the measurement of TERS spectra, carried out by adsorbing molecules directly on the tips, which were then measured isolated from any surface. The optimised process for tip production was to sputter a 5 nm titanium adhesion layer on the silicon commercial probes, followed by 90 nm of gold. Self-assembled monolayers of thiophenol were employed in this study. The isolated tip method for precise spectral measurements was compared to the standard process of putting the probe in contact with a surface supporting the analyte, and it was found that the former yielded much more precise acquisitions with respect to the latter (25% standard deviation of intensity measurements in isolated tip configuration, a significant reduction from the 43% in standard gap mode).

A novel disposition in TERS was also realised in this thesis, in order to recreate a parallel to one of the most common occurrences in SERS: tip dimers, which were expected to yield a much higher enhancement of Raman signals originating from their centres with respect to other configurations. This was achieved by developing and employing a specific substrate, consisting in an array of identical tips obtained from nanoimprinting lithography of silicon anisotropically etched with KOH. The final surface, made of PDMS sputtered with gold, proved convenient to achieve the tip-tip dimer configuration, which, as expected, resulted in stronger TERS intensities with respect to flat surfaces and isolated tips. Tip dimers were utilised in the TERS measurement of three analytes: the two thiols employed before for the spatial standard, thiophenol and MMC, as well as thiram, a law-regulated pesticide routinely used in agriculture for human consumption.

The concept of enhancement factor in TERS and SERS was also fully explored. This required the development of a method for probing the focal volume of Raman microscopes by means of nanomaterials. Monolayer graphene was employed in two different ways to measure the dimensions of the focussed beam waist and the confocal depth of the Raman microscope: a full sheet was utilised for depth, while a graphene edge was employed in a procedure similar to the knife-edge method

commonly used in optics for the measurement of laser spot sizes at the beam waist. After verifying that the profiles in the three dimensions were actually Gaussian, least squares regressions on multiple scans were used to quantify the volume dimensions with their uncertainties, resulting in a precise estimation by actual measurements instead of theoretical predictions.

A procedure for the evaluation of enhanced and non-amplified Raman intensities with the same experimental parameters which could be applied to a great quantity of samples, including thiols and thiram, was also conceived for the accurate calculation of the enhancement factor. The technique involved the employment of an appropriate solution of which Raman spectra were measured with enhanced Raman conditions and with a setup optimised for standard Raman acquisitions. When the equivalent Raman intensity was found with this process, the values of the enhancement factors for thiophenol, MMC and thiram were calculated with their uncertainties for the three nanoparticle configurations explored with the AFM-TERS tips. It was found that thiram manifested a much higher enhancement factor with respect to the other two analytes, while MMC the lowest. Furthermore, it was calculated that gap mode yielded on average (2.2 ± 0.4) times higher enhancement with respect to the isolated tip, whereas tip dimers exhibited a mean enhancement factor amplification of (6.7 ± 0.6) when compared to the single tip.

Future developments on these topics include the accurate quantification of the enhancement factor of the silver STM-TERS tips manufactured by electrochemical etching; the gold-sputtered AFM-TERS tips could also be employed with the nanopatterned thiol reference sample for spatial capabilities of TERS chemical mapping, and these results may be compared to the measurements on the same samples without the mask lift-off, testing a novel, all-in-one standard for the topographic and chemical imaging of TERS. By employing the nanopatterned surface and the isolated tip procedure for the measurement of the enhancement factor, a comparison of every aspect of their performances can be conducted with respect to the STM-TERS. Another natural step forward from the studies presented in this thesis would be interlaboratory comparisons, which are critical in order for the innovation of a measurement technique, for the development of standard practices and samples, and for it to eventually become widespread. Calibration of the thiol nanopatterned samples by metrological AFM would also allow the TERS community to have a secondary standard for SI traceability to the metre. The study conducted so far on the measurement of the focal volume of the Raman microscope impacts a much wider field than just TERS, since quantification by (non-enhanced) Raman is an open issue and a goal much sought after. The work can be expanded by merging the two practices of graphene probing presented in this thesis in a single procedure, as stated earlier, allowing a three-dimensional scan of the volume by the graphene edge method, which would be applicable to any laser mode and intensity behaviour in space, surpassing the need of assuming ideal profiles for the calculations. Another possibility with significance beyond TERS, affecting

SERS as well, is the accurate quantification of traces of molecules by enhanced Raman: the knowledge of an accurate enhanced factor for a target molecule with its respective uncertainty allows the estimation of the number of molecules involved in the enhanced Raman scattering by acquiring TERS/SERS spectra, then simply using an inverse formula to determine the amount of substance. The method of calculation of the enhancement factor presented in this thesis, in fact, could be applied to a vast variety of molecules of interest in the surfaces chemistry field, as demonstrated in this work by the use of pesticide traces, opening up new, important applications of the two techniques.

Bibliography

[1] Martin Fleischmann, Patrick J Hendra, and A James McQuillan. "Raman spectra of pyridine adsorbed at a silver electrode". In: *Chemical Physics Letters* 26.2 (1974), pp. 163–166.

[2] Pablo G Etchegoin and Eric C Le Ru. *Basic electromagnetic theory of SERS*. Wiley Online Library, 2010, pp. 1–37. DOI: 10.1002/9783527632756.

[3] Peter N Njoki et al. "Size correlation of optical and spectroscopic properties for gold nanoparticles". In: *The Journal of Physical Chemistry C* 111.40 (2007), pp. 14664–14669. DOI: 10.1021/jp074902z.

[4] K Lance Kelly et al. "The optical properties of metal nanoparticles: the influence of size, shape, and dielectric environment". In: *The Journal of Physical Chemistry B* 107.3 (2003), pp. 668–677. DOI: 10.1021/jp026731y.

[5] Otto Muskens et al. "Optical response of a single noble metal nanoparticle". In: *Journal of Optics A: Pure and Applied Optics* 8.4 (2006), S264. DOI: 10.1088/1464-4258/8/4/S28.

[6] Nastaran Kazemi-Zanjani, Sylvain Vedraine, and François Lagugné-Labarthet. "Localized enhancement of electric field in tip-enhanced Raman spectroscopy using radially and linearly polarized light". In: *Optics Express* 21.21 (2013), pp. 25271–25276. DOI: 10.1364/OE.21.025271.

[7] Raoul M. Stöckle et al. "Nanoscale chemical analysis by tip-enhanced Raman spectroscopy". In: *Chemical Physics Letters* 318.1-3 (2000), pp. 131–136.

[8] W. E. Smith and G. Dent. *Modern Raman Spectroscopy – A Practical Approach*. Wiley Online Library, 2005.

[9] Elena Bailo and Volker Deckert. "Tip-enhanced Raman scattering". In: *Chemical Society Reviews* 37.5 (2008), pp. 921–930.

[10] Gregory D. Smith and Robin J.H. Clark. "Raman microscopy in archaeological science". In: *Journal of Archaeological Science* 31 (2004), pp. 1137–1160.

[11] Katrin Kneipp and Harald Kneipp. "Single molecule Raman scattering". In: *Applied Spectroscopy* 60.12 (2006), 322A.

[12] Eric C Le Ru et al. “Surface enhanced Raman scattering enhancement factors: a comprehensive study”. In: *The Journal of Physical Chemistry C* 111.37 (2007), pp. 13794–13803.

[13] Evan J Blackie, Eric C Le Ru, and Pablo G Etchegoin. “Single-molecule surface-enhanced Raman spectroscopy of nonresonant molecules”. In: *Journal of the American Chemical Society* 131.40 (2009), pp. 14466–14472.

[14] Christoph Langhammer et al. “Plasmonic properties of supported Pt and Pd nanostructures”. In: *Nano Letters* 6.4 (2006), pp. 833–838.

[15] Bhavya Sharma et al. “SERS: materials, applications, and the future”. In: *Materials Today* 15.1 (2012), pp. 16–25.

[16] Paul L. Stiles et al. “Surface-enhanced Raman spectroscopy”. In: *Annual Review of Analytical Chemistry* 26.1 (2008), p. 601.

[17] Katrin Kneipp, Martin Moskovits, and Harald Kneipp. *Surface-enhanced Raman scattering: physics and applications*. Springer Science & Business Media, 2006.

[18] Norihiko Hayazawa, Taka-aki Yano, and Satoshi Kawata. “Highly reproducible tip-enhanced Raman scattering using an oxidized and metallized silicon cantilever tip as a tool for everyone”. In: *Journal of Raman Spectroscopy* 43.9 (2012), pp. 1177–1182.

[19] Atsushi Taguchi et al. “Controlling the plasmon resonance wavelength in metal-coated probe using refractive index modification”. In: *Optics Express* 17.8 (2009), pp. 6509–6518.

[20] Xudong Cui et al. “Highly efficient nano-tips with metal–dielectric coatings for tip-enhanced spectroscopy applications”. In: *Chemical Physics Letters* 453.4 (2008), pp. 262–265.

[21] Xudong Cui et al. “Tuning the resonance frequency of Ag-coated dielectric tips”. In: *Optics Express* 15.13 (2007), pp. 8309–8316.

[22] Regina Treffer et al. “Advances in TERS (tip-enhanced Raman scattering) for biochemical applications”. In: *Biochemical Society Transactions* 40.4 (2012), pp. 609–614.

[23] Zhenglong Zhang et al. “Tip-enhanced Raman spectroscopy”. In: *Analytical Chemistry* 88.19 (2016), pp. 9328–9346.

[24] Ute Neugebauer et al. “On the way to nanometer-sized information of the bacterial surface by tip-enhanced Raman spectroscopy”. In: *Chemical Physics and Physical Chemistry* 7.7 (2006), pp. 1428–1430.

[25] Federico Latorre et al. “Spatial resolution of tip-enhanced Raman spectroscopy–DFT assessment of the chemical effect”. In: *Nanoscale* 8.19 (2016), pp. 10229–10239.

[26] Evelien M van Schrojenstein Lantman et al. "Catalytic processes monitored at the nanoscale with tip-enhanced Raman spectroscopy". In: *Nature Nanotechnology* 7.9 (2012), p. 583.

[27] Nan Jiang et al. "Observation of multiple vibrational modes in ultrahigh vacuum tip-enhanced Raman spectroscopy combined with molecular-resolution scanning tunneling microscopy". In: *Nano Letters* 12.10 (2012), pp. 5061–5067.

[28] Chi Chen, Norihiko Hayazawa, and Satoshi Kawata. "A 1.7 nm resolution chemical analysis of carbon nanotubes by tip-enhanced Raman imaging in the ambient". In: *Nature Communications* 5 (2014), p. 3312.

[29] Boon-Siang Yeo et al. "Tip-enhanced Raman Spectroscopy–Its status, challenges and future directions". In: *Chemical Physics Letters* 472.1 (2009), pp. 1–13.

[30] Matthew D Sonntag et al. "Recent advances in tip-enhanced Raman spectroscopy". In: *The Journal of Physical Chemistry Letters* 5.18 (2014), pp. 3125–3130.

[31] Matthew D Sonntag et al. "Single-molecule tip-enhanced Raman spectroscopy". In: *The Journal of Physical Chemistry C* 116.1 (2011), pp. 478–483.

[32] Dana Cialla et al. "Raman to the limit: tip-enhanced Raman spectroscopic investigations of a single tobacco mosaic virus". In: *Journal of Raman Spectroscopy* 40.3 (2009), pp. 240–243.

[33] R Zhang et al. "Chemical mapping of a single molecule by plasmon-enhanced Raman scattering". In: *Nature* 498.7452 (2013), pp. 82–86.

[34] Liang Zhu et al. "Experimental challenges for approaching local strain determination in silicon by nano-Raman spectroscopy". In: *Materials Science-Poland* 25.1 (2007), pp. 19–31.

[35] Bayden R Wood et al. "Tip-enhanced Raman scattering (TERS) from hemozoin crystals within a sectioned erythrocyte". In: *Nano Letters* 11.5 (2011), pp. 1868–1873.

[36] Weihua Zhang et al. "Single molecule tip-enhanced Raman spectroscopy with silver tips". In: *The Journal of Physical Chemistry C* 111.4 (2007), pp. 1733–1738.

[37] J Stadler, T Schmid, and R Zenobi. "Nanoscale chemical imaging using top-illumination tip-enhanced Raman spectroscopy". In: *Nano Letters* 10.11 (2010), pp. 4514–4520.

[38] Victor L Mironov. *Fundamentals of scanning probe microscopy*. Moscow: Technosfera, 2004.

[39] International Bureau of Weights and Measures (BIPM). "VIM–International Vocabulary of Metrology – Basic and General Concepts and Associated Terms". In: *JCGM 200:2012* (2012).

[40] International Bureau of Weights and Measures (BIPM). "GUM–Guide to the Expression of Uncertainty in Measurement". In: *JCGM 100:2008* (2008).

[41] International Bureau of Weights and Measures (BIPM). *History of the SI*. http://www.bipm.org. Accessed: 2019-07-01.

[42] Steven J Choquette et al. "Relative intensity correction of Raman spectrometers: NIST SRMs 2241 through 2243 for 785 nm, 532 nm, and 488 nm/514.5 nm excitation". In: *Applied Spectroscopy* 61.2 (2007), pp. 117–129. DOI: 10.1366/000370207779947585.

[43] ASTM Committee E13 on Molecular Spectroscopy and Separation Science. *Standard Guide for Raman Shift Standards for Spectrometer Calibration*. 2007.

[44] BIPM Consultative Committee for Length. *Mise en pratique for the definition of the metre in the SI*. 2019.

[45] TJ Quinn. "Practical realization of the definition of the metre, including recommended radiations of other optical frequency standards (2001)". In: *Metrologia* 40.2 (2003), p. 103.

[46] Virpi Korpelainen. "Traceability for nanometre scale measurements: Atomic force microscopes in dimensional nanometrology". PhD thesis. University of Helsinki, 2014.

[47] V Korpelainen and A Lassila. "Calibration of a commercial AFM: traceability for a coordinate system". In: *Measurement Science and Technology* 18.2 (2007), p. 395.

[48] Oliver Krause. *Why Probes Look the Way They Do – Concepts and Technologies of AFM Probes Manufacturing*. Webinar. 2008.

[49] Phil Russell. *AFM Probe Manufacturing*. Webinar. 2008.

[50] *NT-MDT website*. http://www.ntmdt-tips.com. Accessed: 2019-07-01.

[51] Lothar Opilik et al. "Degradation of silver near-field optical probes and its electrochemical reversal". In: *Applied Physics Letters* 107.9 (2015), p. 091109.

[52] Naresh Kumar et al. "Extending the plasmonic lifetime of tip-enhanced Raman spectroscopy probes". In: *Physical Chemistry Chemical Physics* 18.19 (2016), pp. 13710–13716.

[53] Thomas Schmid et al. "Nanoscale chemical imaging using tip-enhanced Raman spectroscopy: a critical review". In: *Angewandte Chemie International Edition* 52.23 (2013), pp. 5940–5954.

[54] Teng-Xiang Huang et al. "Tip-enhanced Raman spectroscopy: tip-related issues". In: *Analytical and Bioanalytical Chemistry* 407.27 (2015), pp. 8177–8195.

[55] Thomas Siegfried et al. "Engineering metal adhesion layers that do not deteriorate plasmon resonances". In: *ACS Nano* 7.3 (2013), pp. 2751–2757.

[56] Florent Colas et al. "Comparison of adhesion layers of gold on silicate glasses for SERS detection". In: *Journal of Optics* 17.11 (2015), p. 114010.

[57] Loan Le Thi Ngoc et al. "Suppression of surface-enhanced raman scattering on gold nanostructures by metal adhesion layers". In: *The Journal of Physical Chemistry C* 120.33 (2016), pp. 18756–18762.

[58] Desalegn T Debu et al. "Surface plasmon damping effects due to Ti adhesion layer in individual gold nanodisks". In: *Optical Materials Express* 7.1 (2017), pp. 73–84.

[59] Yasser Khan et al. "Two-step controllable electrochemical etching of tungsten scanning probe microscopy tips". In: *Review of Scientific Instruments* 83.6 (2012), p. 063708.

[60] Alessio Sacco et al. "Development of a candidate reference sample for the characterization of tip-enhanced Raman spectroscopy spatial resolution". In: *RSC Advances* 8.49 (2018), pp. 27863–27869. DOI: 10.1039/C8RA03762K.

[61] Alessio Sacco et al. "Novel Approaches in Tip-Enhanced Raman Spectroscopy: Accurate Measurement of Enhancement Factors and Pesticide Detection in Tip Dimer Configuration". In: *The Journal of Physical Chemistry C* 123.40 (2019), pp. 24723–24730. DOI: 10.1021/acs.jpcc.9b07016.

[62] Carolin Blum et al. "Tip-enhanced Raman spectroscopy–an interlaboratory reproducibility and comparison study". In: *Journal of Raman Spectroscopy* 45.1 (2014), pp. 22–31.

[63] Peter Walke et al. "Silver nanowires for highly reproducible cantilever based AFM-TERS microscopy: towards a universal TERS probe". In: *Nanoscale* 10.16 (2018), pp. 7556–7565.

[64] Sergey S Kharintsev et al. "Near-field optical taper antennas fabricated with a highly replicable ac electrochemical etching method". In: *Nanotechnology* 22.2 (2010), p. 025202.

[65] JS Lloyd et al. "Reproducible electrochemical etching of silver probes with a radius of curvature of 20 nm for tip-enhanced Raman applications". In: *Applied Physics Letters* 99.14 (2011), p. 143108.

[66] Ernest Paul DeGarmo et al. *Materials and process in manufacturing*. Prentice Hall Upper Saddle River, 1997.

[67] Sigma-Aldrich. *Thiophenol Safety Data Sheet*. http://www.sigma-aldrich.com. Accessed: 2019-07-01. 2014.

[68] Sigma-Aldrich. *7-mercapto-4-methylcoumarin Safety Data Sheet*. http://www.sigma-aldrich.com. Accessed: 2019-07-01. 2019.

[69] Thomas James Smith. "MolView: a program for analyzing and displaying atomic structures on the Macintosh personal computer". In: *Journal of Molecular Graphics* 13.2 (1995). Schemes created with MolView. http://molview.org, pp. 122–125.

[70] Debdulal Roy, Jian Wang, and Craig Williams. "Novel methodology for estimating the enhancement factor for tip-enhanced Raman spectroscopy". In: *Journal of Applied Physics* 105.1 (2009), p. 013530.

[71] Naresh Kumar, Alasdair Rae, and Debdulal Roy. "Accurate measurement of enhancement factor in tip-enhanced Raman spectroscopy through elimination of far-field artefacts". In: *Applied Physics Letters* 104.12 (2014), p. 123106.

[72] SA Kara et al. "Fabrication of flexible silicon nanowires by self-assembled metal assisted chemical etching for surface enhanced Raman spectroscopy". In: *RSC Advances* 6.96 (2016), pp. 93649–93659.

[73] Peter Morf. "Self-assembled monolayers beyond thiols: dithiocarbamates-from pure layers to ternary assembly systems". PhD thesis. University of Basel, 2007.

[74] Colin D Bain, Joe Evall, and George M Whitesides. "Formation of monolayers by the coadsorption of thiols on gold: variation in the head group, tail group, and solvent". In: *Journal of the American Chemical Society* 111.18 (1989), pp. 7155–7164.

[75] J Christopher Love et al. "Self-assembled monolayers of thiolates on metals as a form of nanotechnology". In: *Chemical Reviews* 105.4 (2005), pp. 1103–1170.

[76] Li-Jun Wan et al. "Molecular orientation and ordered structure of benzenethiol adsorbed on gold (111)". In: *The Journal of Physical Chemistry B* 104.15 (2000), pp. 3563–3569.

[77] Yu-Tai Tao et al. "Structure evolution of aromatic-derivatized thiol monolayers on evaporated gold". In: *Langmuir* 13.15 (1997), pp. 4018–4023.

[78] Eyal Sabatani et al. "Thioaromatic monolayers on gold: a new family of self-assembling monolayers". In: *Langmuir* 9.11 (1993), pp. 2974–2981.

[79] Eleonora Cara et al. "Influence of the long-range ordering of gold-coated Si nanowires on SERS". In: *Scientific Reports* 8.1 (2018), p. 11305.

[80] Norihiko Hayazawa et al. “Metallized tip amplification of near-field Raman scattering”. In: *Optics Communications* 183.1-4 (2000), pp. 333–336.

[81] N Lee et al. “High contrast scanning nano-Raman spectroscopy of silicon”. In: *Journal of Raman Spectroscopy* 38.6 (2007), pp. 789–796.

[82] Mark S Anderson. “Locally enhanced Raman spectroscopy with an atomic force microscope”. In: *Applied Physics Letters* 76.21 (2000), pp. 3130–3132.

[83] Catalin C Neacsu et al. “Scanning-probe Raman spectroscopy with single-molecule sensitivity”. In: *Physical Review B* 73.19 (2006), p. 193406.

[84] Chao Zhang, Bao-Qin Chen, and Zhi-Yuan Li. “Optical origin of subnanometer resolution in tip-enhanced Raman mapping”. In: *The Journal of Physical Chemistry C* 119.21 (2015), pp. 11858–11871.

[85] Xiang Wang et al. “Tip-enhanced Raman spectroscopy for surfaces and interfaces”. In: *Chemical Society Reviews* 46.13 (2017), pp. 4020–4041.

[86] Yurui Fang, Zhenglong Zhang, and Mengtao Sun. “High vacuum tip-enhanced Raman spectroscope based on a scanning tunneling microscope”. In: *Review of Scientific Instruments* 87.3 (2016), p. 033104.

[87] Richard Koops, Marijn van Veghel, and Arthur van de Nes. “A dedicated calibration standard for nanoscale areal surface texture measurements”. In: *Microelectronic Engineering* 141 (2015), pp. 250–255.

[88] Frederik Stöhr et al. “Three-dimensional nanometrology of microstructures by replica molding and large-range atomic force microscopy”. In: *Microelectronic Engineering* 141 (2015), pp. 6–11.

[89] Angelo Taglietti et al. “Mixing thiols on the surface of silver nanoparticles: preserving antibacterial properties while introducing SERS activity”. In: *Journal of Nanoparticle Research* 15.11 (2013), p. 2047.

[90] Bruno Pettinger et al. “Direct monitoring of plasmon resonances in a tip-surface gap of varying width”. In: *Physical Review B* 76.11 (2007), p. 113409.

[91] Eugene Bortchagovsky, T Schmid, and Renato Zenobi. “Internal standard for tip-enhanced Raman spectroscopy”. In: *Applied Physics Letters* 103.4 (2013), p. 043111.

[92] Jianing Chen et al. “Tip-enhanced Raman scattering of p-thiocresol molecules on individual gold nanoparticles”. In: *Applied Physics Letters* 92.9 (2008), p. 093110.

[93] Benjamin Saute and Radha Narayanan. “Solution-based direct readout surface enhanced Raman spectroscopic (SERS) detection of ultra-low levels of thiram with dogbone shaped gold nanoparticles”. In: *Analyst* 136.3 (2011), pp. 527–532.

[94] Orazio Svelto and David C Hanna. *Principles of lasers*. Vol. 4. Springer, 1998.

[95] URL: http://www.graphene-supermarket.com.

[96] Xuesong Li et al. "Large-area synthesis of high-quality and uniform graphene films on copper foils". In: *Science* 324.5932 (2009), pp. 1312–1314.

[97] Xuesong Li et al. "Transfer of large-area graphene films for high-performance transparent conductive electrodes". In: *Nano Letters* 9.12 (2009), pp. 4359–4363.

[98] Xuelei Liang et al. "Toward clean and crackless transfer of graphene". In: *ACS Nano* 5.11 (2011), pp. 9144–9153.

[99] Marija S Scholl. "Measured spatial properties of the cw Nd: YAG laser beam". In: *Applied Optics* 19.21 (1980), pp. 3655–3659.

[100] Mario Gonzalez-Cardel, Pedro Arguijo, and Rufino Diaz-Uribe. "Gaussian beam radius measurement with a knife-edge: a polynomial approximation to the inverse error function". In: *Applied Optics* 52.16 (2013), pp. 3849–3855.

[101] Matteo Bruna and SJAPL Borini. "Optical constants of graphene layers in the visible range". In: *Applied Physics Letters* 94.3 (2009), p. 031901.

[102] Kwanpyo Kim et al. "Atomically perfect torn graphene edges and their reversible reconstruction". In: *Nature Communications* 4 (2013), p. 2723.

[103] Gerald F Marshall. *Laser Beam Scanning: Opto-Mechanical Devices, Systems and Data Storage Optics*. Marcel Dekker, Inc., 1985.

[104] Mikis Mylonakis et al. "Simple precision measurements of optical beam sizes". In: *Applied Optics* 57.33 (2018), pp. 9863–9867.

[105] LM Malard et al. "Raman spectroscopy in graphene". In: *Physics Reports* 473.5-6 (2009), pp. 51–87.

[106] Joe Hodkiewicz. "The Importance of Tight Laser Power Control When Working with Carbon Nanomaterials". In: *Spectroscopy* 26.7 (2011), p. 22.

[107] Isaac Childres et al. "Raman spectroscopy of graphene and related materials". In: *New Developments in Photon and Materials Research* 1 (2013).

[108] EPA. *Reregistration Eligibility Decision (RED) for Thiram*. 2004.

[109] Tanja Deckert-Gaudig et al. "Tip-enhanced Raman spectroscopy–from early developments to recent advances". In: *Chemical Society Reviews* 46.13 (2017), pp. 4077–4110.

[110] Natalia Martin Sabanes et al. "The effect of STM parameters on tip-enhanced Raman spectra". In: *Faraday Discussions* 205 (2017), pp. 233–243.

[111] Yutaka Maruyama and Wataru Kanematsu. "Confocal volume in laser Raman microscopy depth profiling". In: *Journal of Applied Physics* 110.10 (2011), p. 103107.

[112] Neil J Everall. "Modeling and measuring the effect of refraction on the depth resolution of confocal Raman microscopy". In: *Applied Spectroscopy* 54.6 (2000), pp. 773–782.

[113] Jinlong Gong et al. "Micro-and nanopatterning of inorganic and polymeric substrates by indentation lithography". In: *Nano Letters* 10.7 (2010), pp. 2702–2708.

[114] Jingran Zhang et al. "Fabrication of gold-coated PDMS surfaces with arrayed triangular micro/nanopyramids for use as SERS substrates". In: *Beilstein Journal of Nanotechnology* 8.1 (2017), pp. 2271–2282.

[115] Troy A Alexander. "Applications of surface-enhanced Raman spectroscopy (SERS) for biosensing: an analysis of reproducible commercially available substrates". In: *Smart Medical and Biomedical Sensor Technology III*. Vol. 6007. International Society for Optics and Photonics. 2005, p. 600703.

[116] Troy A Alexander and Dianna M Le. "Characterization of a commercialized SERS-active substrate and its application to the identification of intact Bacillus endospores". In: *Applied Optics* 46.18 (2007), pp. 3878–3890.

[117] Mikella E Farrell, Srikanth Singamaneni, and Paul M Pellegrino. "Targeting Biological Sensing with commercial SERS substrates". In: *Advanced Environmental, Chemical, and Biological Sensing Technologies Ix*. Vol. 8366. International Society for Optics and Photonics. 2012, p. 836602.

[118] John D Hunter. "Matplotlib: A 2D graphics environment". In: *Computing in science & engineering* 9.3 (2007), p. 90.

This Ph.D. thesis has been typeset by means of the TEX-system facilities. The typesetting engine was pdfLATEX. The document class was `toptesi`, by Claudio Beccari, with option `tipotesi=scudo`. This class is available in every up-to-date and complete TEX-system installation.